12-15-2020

Response of Deep Aquifers to Climate Variability

Karem Fathy Abdelgaber Abdelmohsen

RESPONSE OF DEEP AQUIFERS TO CLIMATE VARIABILITY

by

Karem Fathy Abdelgaber Abdelmohsen

A dissertation submitted to the Graduate College
in partial fulfillment of the requirements
for the degree of Doctor of Philosophy
Geological and Environmental Sciences
Western Michigan University
December 2020

Doctoral Committee:

Mohamed Sutlan, Ph.D., Chair
William Sauck, Ph.D.
Richard Becker, Ph.D.
Matt Reeves, Ph.D.

RESPONSE OF DEEP AQUIFERS TO CLIMATE VARIABILITY

Karem Fathy Abdelgaber Abdelmohsen, Ph.D.

Western Michigan University, 2020

Our recent analysis of Temporal Gravity Recovery and Climate Experiment (GRACE) solutions over the largest aquifer system in Africa (the Nubian Sandstone Aquifer System: NSAS) revealed that while the response of deep aquifers to climatic variations remains a relatively slow process that takes thousands to tens of thousands of years, there is a much faster response in aquifers that are characterized by dense networks of faults, fractures and karst as is the case with the NSAS. This rapid groundwater flow, when it occurs, is detected as an increase in $GRACE_{TWS}$ over areas downgradient and distant (hundreds of km) from the source areas over which increased precipitation occurred in wet periods. The increase in $GRACE_{TWS}$ over these distant areas cannot be accounted for by an increase in precipitation, soil moisture, or surface water flow given the hyperarid conditions even during periods of increased precipitation over the source areas. In this research we will accomplish the following using the NSAS in North Africa as test sites: (1) investigate whether the rapid response observed over the NSAS could be common to many of the aquifers worldwide, (2) identify the conditions under which such rapid flow occurs, and (3) apply groundwater flow models in fractured rocks and use the models to develop sustainable and/or optimum scenarios for groundwater management in areas showing evidence of rapid groundwater flow. These three tasks will be accomplished by conducting the following for each of the investigated aquifer systems: (1) use satellite-based precipitation mission data to identify temporal (short-term climate variability: wet and dry periods) and spatial variations of precipitation over areas of interest (source versus discharge areas), (2) identify the spatial and temporal response of $GRACE_{TWS}$ to short climate variability over the areas of interest, (3) generate $GRACE_{TWS}$ phase, difference, and amplitude images to investigate the direction and extent of $GRACE_{TWS}$ variations that are indicative of mass movement in dry and wet periods and seasons; (4) delineate potential preferred pathways for groundwater flow by mapping fault traces from shaded relief maps, radar backscatter images, and geologic maps and their postulated

extension in the subsurface from tilt derivative (TDR) product of a selected Gravity Field and Steady-State Ocean Circulation Explorer (GOCE)-based global geopotential model (GGM). Finally GRACE-based inferences will be validated using: (1) field data (temporal head data, isotopic and geochemical composition for groundwater samples) along the identified structures and satellite-based (SMOS) soil moisture content to test whether the identified structures represent preferred pathways for groundwater flow, and (2) conceptual flow models that simulate the rapid groundwater flow from the source areas towards discharge areas along preferred pathways and a much slower flow in the surrounding media. Findings will provide new insights into the response of large, deep aquifers to climate variability and address the sustainability of the NSAS and similar fossil aquifers worldwide.

ACKNOWLEDGMENTS

I am very grateful to ALLAH almighty for his graces and blessings throughout my PhD journey.

First, I would like to express my sincere gratitude to my PhD advisor and mentor, Prof. Dr. Mohamed Sultan, for his continuous support, his patience, motivation, and immense knowledge. His guidance helped me conduct my research, publish my papers, and write my thesis. Nothing would have been possible without Dr. Mohamed's support and guidelines. I could not have imagined having a better advisor and mentor for my Ph.D study.

Besides my advisor, I would like to thank the rest of my thesis committee: Prof. Matt Reeves, Prof. William A Sauck, and Dr. Richard Becker, for their insightful comments and encouragement, and for their follow up on the progress of my research work.

I really appreciate the support of Dr. Abotalib Farag for his fruitful discussions and valuable suggestions, especially in geological-related areas.

I also appreciate the support of my older advisor (Prof. Khaled Zahran) and colleagues in NRIAG (Dr. Nadia and Dr. Sobh) for their fruitful discussions and valuable advice.

I also want to extend my thanks to my colleagues in the Earth Science Remote Sensing Facility (ESRS) for their valuable support, encouragement, and advice. I am so lucky and privileged to be part of ESRS lab. I'll never forget you guys (Hossein, Moein, Fahad, Mohamed, Dr. Abotalib, Guzalay, Soha, Sita, Kyle, Mustafa, Hannah, Esayas, and Abdulaziz).

This research is funded by the National Aeronautics and Space Administration (NASA) Earth Science Division and the Egyptian Ministry of Higher Education and Scientific Research.

Last but not the least, I would like to thank my father and mother "Fathy and Amal", my Wife "Fatma", my brothers and sister for supporting me throughout my PhD journey and my life in general.

Karem F. Abdelmohsen

TABLE OF CONTENTS

Table of Contents—Continued

CHAPTER

LIST OF TABLES

LIST OF FIGURES

CHAPTER 1

INTRODUCTION

1.1 Dissertation Framework

Chapter 2 provides a brief overview of the GRACE satellite missions and an overview of the different GRACE solutions that have been utilized for this research work.

Chapters 3 and 4 of this thesis are written as independent research studies based on manuscripts, one of which has been published in Science of The Total Environment (Chapter 3; Abdelmohsen et al., 2019), and the other has been submitted for consideration for publication in and Earth Science Reviews and is currently under review (Abdelmohsen et al., 2020).

Chapter 3 provides an integrated research investigation that incorporates the analysis of Temporal Gravity Recovery and Climate Experiment (GRACE), Soil Moisture and Ocean Salinity mission (SMOS), satellite altimetry, stable isotopic composition of groundwater, and precipitation and static global geopotential models over the Nubian Sandstone Aquifer System (NSAS) to examine the structural control on groundwater flow and the aquifer response to climate variability.

Chapter 4 provides a study on Lake-aquifer interactions. I first review the methods that are used by the scientific community to address this issue, then discuss ways by which GRACE measurements can contribute to the understanding of these complex systems that are quite difficult to investigate using traditional modelling techniques. To demonstrate how GRACE

seasonal cycle can be used to better understand lake-aquifer interactions we chose the Dakhla subbasin within the NSAS as a test site.

Chapter 5 provides a summary of the thesis and suggestions for future work.

CHAPTER 2

BACKGROUND

2.1 GRACE Satellite Mission

The GRACE satellite was launched in 2002 to map the temporal variations in Earth's global gravity field and mean gravity field (Tapley et al., 2004a, 2004b). The variability in the gravity field solutions at the time scales examined by GRACE (i.e., days to years) are largely related to redistribution of mass at, or near, Earth's surface (Wahr et al., 2004). GRACE measures the variability in terrestrial water storage (TWS), which refers to the total water content for all the reservoirs (e.g., groundwater, surface water, snow and ice, soil moisture and permafrost, or wet biomass) in an area. Spherical harmonic (SH) solutions of GRACE gravity data have been used successfully to measure TWS variations over large hydrologic systems (Ahmed et al., 2016, 2014; Ahmed and Abdelmohsen, 2018; Mohamed et al., 2016; Sultan et al., 2014, 2013; Wouters et al., 2014), yet their applications on subbasin scales were hindered by their coarse spatial resolution (>125,000 km^2), leakage signal problems, and the required complex post-processing steps (Scanlon et al., 2016).

There are three publicly available GRACE solutions that were utilized in this study: (1) CSR-M monthly mass concentration (mascon) solutions (Save et al., 2016) from the Center for Space Research at the University of Texas (UT-CSR; http://www.csr.utexas.edu/grace), (2) the mascon solutions from the Jet Propulsion Laboratory (JPL-M), and (3) the spherical harmonics of the UT-CSR GRACE solution (CSR- SH). The mascon solutions are advantageous compared to the spherical harmonics given their higher signal-to-noise ratio, higher spatial resolution, and reduced leakage errors. Moreover, they do not require post processing including de-striping or smoothing filtering or any scaling to compensate for the attenuation of the geophysical signals caused by de-striping (Luthcke et al., 2013; Save et al., 2016; Bridget R. Scanlon et al., 2016; Watkins et al., 2015; D. N. Wiese et al., 2016).

The CSR developed a new GRACE Release solution (RL06) by improving models and parameterization in the previous release (RL05) to provide a starting point for GRACE Follow On (GRACE-FO) processing (Save, 2019). The entire GRACE mission (2002–2017) were reprocessed with the same standards as GRACE-FO. The GRACE CSR-M solutions were derived using Tikhonov regularization with an L-ribbon approach to compute the regularization parameter and were resolved on an equal area geodesic grid of roughly 1° at the equator. However, that is not likely to be the effective resolution of this product that is estimated at ~ 250 km (Save, 2019). The data provided are over sampled on an equiangular grid of size 0.5°×0.5° in RL05 and 0.25° × 0.25° in RL06 for ease of use. (Save, 2019; Save et al., 2016). The CSR RL06M has a newly defined grid in which the hexagonal tiles that extend across the coastline in the earlier release (RL05M) are now divided into two tiles along the coastline to minimize the leakage signal between land and ocean signals (Save, 2019; Save et al., 2016). The newly launched GRACE-FO data is being processed with the same standards as GRACE RL06.

CHAPTER 3

RESPONSE OF DEEP AQUIFERS TO CLIMATE VARIABILITY

3.1 Introduction

Short-lived climatic variabilities on timescales of years to decades is believed to affect the recharge of shallow (depth to water table [DWT] < 30 m), but not deep, aquifers (Chen et al., 2004; Healy and Cook, 2002). By contrast, the impact of climate change and climatic variabilities on deep aquifer systems reportedly spans longer timescales (thousands to tens of thousands of years; Abotalib et al., 2019; Fendorf et al., 2010; Hanson et al., 2006; Sturchio et al., 2004) due to the length of time for precipitation to infiltrate unsaturated soil profiles and underlying shallow aquifers (Dickinson et al., 2014), and for the infiltrated waters to flow from recharge to distant discharge areas (Abotalib et al., 2019). The response of deep aquifers to a recharge signal caused by climatic variations is mainly constrained by the aquifer's properties (e.g., aquifer transmissivity and storativity, thickness of clay interbeds, and the presence of fractures, faults, and karst topography) and depths to groundwater (Geyer et al., 2008; Goode, 1996; Seaton and Burbey, 2005; Walton, 2011). The well-established time-lag response of deep aquifer systems has been recently challenged with reported sub-annual deep aquifer response to short-lived climatic variabilities in the United States (Russo and Lall, 2017) and by the presence of young decadal-aged waters with measurable tritium within deep (>250 m) fossil aquifers (Jasechko et al., 2017). However, the mechanism by which modern precipitation infiltrates and mixes with fossil groundwater in deep aquifers is still poorly understood. In this manuscript, we use data from the Gravity Recovery and Climate Experiment (GRACE) satellite to document a rapid response to short-lived climatic variabilities over a deep, extensive (area: 2×10^6 km^2), fossil aquifer in northeast Africa, the Nubian Sandstone Aquifer System (NSAS) and provide possible mechanisms for the observed rapid response.

The NSAS with its simple hydrologic setting allows straightforward interpretations of the observed temporal variations in GRACE TWS solutions, a situation that does not readily apply to the more complex hydrologic systems worldwide. For example, recharge occurs in the southern sections of the NSAS (Sudan and Chad), where the aquifer crops out and where the average annual precipitation (AAP) could reach up to 1000 mm/yr locally and is minimal to absent in the northern parts (Egypt and Libya) where precipitation is negligible (AAP: <20 mm/yr). Using the NSAS in northeast Africa (Fig. 1), we demonstrate that throughout the investigated period (April 2002 to June 2016), the observed temporal GRACE mass variations were largely controlled by recharge in the south and from Lake Nasser and by the rapid and preferential groundwater flow along complex fracture/fault systems and karst topography. Findings were corroborated by field, geophysical, topographic, and isotopic investigations. We would have not been able to demonstrate these findings if we dealt with more complex systems where precipitation and recharge are occurring across the entire aquifer.

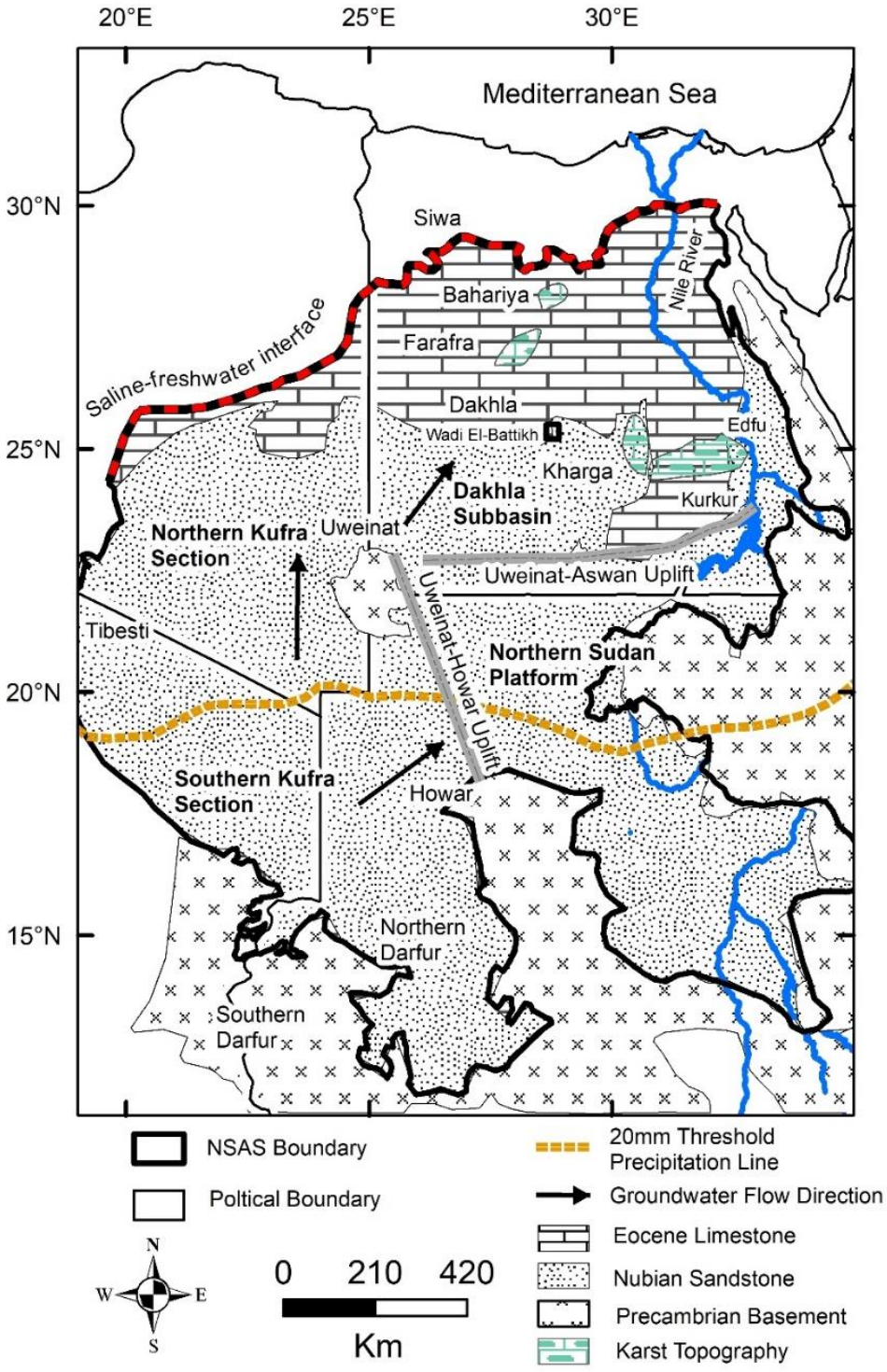

Figure 1. (a) Location map showing the distribution of the NSAS and its subbasins (Dakhla, Kufra, and Northern Sudan Platform), the basement uplifts (Uweinat-Aswan, Uweinat-Howar), the 20 mm AAP threshold line, and the groundwater flow direction (Ball, 1927; Sanford, 1935).

3.2 Geologic and Hydrogeologic Settings

The NSAS consists mainly of thick (>3 km) Paleozoic and Mesozoic continental sandstone intercalated with marine Tertiary carbonates, shale, and clay deposited in shallow marine and deltaic settings (Hesse et al., 1987). The aquifer is bound by basement from the east and south, the Devonian bedrock from the west, and by the saltwater-freshwater interface in the north (Sultan et al., 2013). The NSAS is formed of three major subbasins that are separated by basement uplifts. The Uweinat-Aswan uplift separates the Dakhla subbasin (Egypt) from the Northern Sudan Platform subbasin (northern Sudan) to the south, and the Uweinat-Howar uplift separates the latter (Northern Sudan Platform subbasin) from the Kufra subbasin (Libya, northeastern Chad, and northwestern Sudan) to the west (Hesse et al., 1987; Fig. 1). Along segments of these uplifts, the basement crops out or reaches near surface elevations, yet in other segments along the length of the uplifts, the depth to basement increases allowing groundwater flow through these windows (Ahmed et al., 2016). The Kufra subbasin is here subdivided into the Northern Kufra and the Southern Kufra sections that are separated by a threshold AAP line of 20 mm (Fig. 1). Groundwater flow is generally from the southwest to the northeast, and the aquifer is confined north of latitude 25°N but unconfined to the south of it in the Dakhla subbasin (Ball, 1927; Sanford, 1935).

The NSAS is composed of two major hydrological units: the sandstone-dominated Nubian aquifer system (NAS) and the overlying carbonate-dominated post-Nubian aquifer system (PNAS; (M Bakhbakhi, 2006). The NSAS was largely recharged during previous pluvial periods in the Quaternary by intensification of paleomonsoons (Prell and Kutzbach, 1987; Sarnthein et al., 1981; Yan and Petit-Maire, 1994) or paleowesterlies (Abouelmagd et al., 2014; Sturchio et al., 2004; Sultan et al., 1997). At present, the aquifer is receiving modest local recharge in the

southern highlands (e.g., Gebel Darfur in Sudan and Gebel Tibesti in Chad; Fig. 1) where the Nubian Sandstone crops out and where precipitation reaches up to 96 mm/yr.

3.3 Methodology

The following data sets were generated over investigated areas (e.g., subbasins) and periods to compare to other relevant geologic, topographic, and hydrologic data in a geographic information system (GIS) platform to identify sources of recharge and preferred pathways for groundwater flow and to investigate the aquifers' response to climate variability: (1) $GRACE_{TWS}$ trend images and time series were extracted from $GRACE_{TWS}$ (Figs. 2, 3) to identify the spatial and temporal variations in $GRACE_{TWS}$; (2) Lake Nasser surface water levels (2002–2016) from the US Department of Agriculture's Foreign Agricultural Service (USDA-FAS) global reservoir and lake monitoring database (GRLM; available at https://www.pecad.fas.usda.gov/cropexplorer/global reservoir/), soil moisture data (2010 to 2016) from Soil Moisture and Ocean Salinity (SMOS) mission data (Kerr et al., 2001), and temporal head data (2005 to 2008) to investigate the response of groundwater levels and soil moisture content to fluctuations in Lake Nasser surface water; (3) AAP rates and trends were extracted from Tropical Rainfall Measuring Mission (TRMM) data (Huffman et al., 2007) and correlated with GRACE-derived products to investigate the factor(s) controlling the $GRACE_{TWS}$ variations; (4) deriving $GRACE_{TWS}$ phase and difference in TWS to investigate the direction and extent of TWS variations that are indicative of mass movement in dry and wet periods; (5) geologic maps to extract fault traces; (6) Gravity Field and Steady-State Ocean Circulation Explorer (GOCE)-based global geopotential models (GGMs) to select the model having the least deviation from the terrestrial gravity data; (7) tilt derivative (TDR) product of the selected GGM to extract the subsurface extensions of the fault traces and to map faults in sand-covered areas, and (8) isotopic composition for groundwater samples along faults to test whether structures represent preferred pathways for groundwater flow from Lake Nasser and from the Northern Sudan Platform to the Dakhla subbasin.

3.3.1 GRACE data

The three GRACE solutions which were applied (from April 2002 through June 2016) in this study are reported relative to a 2004–2009 mean baseline. The GRACE CSR-M solutions were derived using Tikhonov regularization (Save et al., 2016) and were resolved on a geodesic grid (grid size: 1 equatorial degree) (Save et al., 2012, 2016). No post-processing and/or filtering or application of empirical scaling factors were applied to the CSR-M or the JPL-M mascon solutions (Watkins et al., 2015; Save et al., 2016). Given the higher signal to noise ratio of the mascon solutions relative to the spherical harmonics (Watkins et al., 2015; Save et al., 2016, Scanlon et al., 2016), the CSR-M solutions were selected as the primary dataset for extracting trends over the investigated subbasins (Rodell et al., 2018). The secular trend in GRACE-derived TWS ($GRACE_{TWS}$) data was extracted by simultaneously fitting a trend and a seasonal term to each TWS time series. The variations (standard deviation) in trend values extracted from all three solutions (CSR-M, JPL-M, and CSR-SH) were considered to represent the uncertainty in the reported trend values (Scanlon et al., 2018; Rodell et al., 2018).

The spherical harmonics data was processed by replacing GRACE-derived C20 coefficients with the solutions from Satellite Laser Ranging (SLR), because the native GRACE-C20 values have a larger uncertainty than the SLR-values. (Cheng et al., 2011; Swenson et al., 2008). The degree-1 coefficients are estimated using the methods from Swenson et al., 2008. and applying the glacial isostatic adjustment (GIA) correction using the GIA model (A et al., 2013). The noise was reduced at the basin scale by applying a destriping filter (Swenson and Wahr, 2006) and a Gaussian (250 km radius) smoothing filter (Wahr et al., 1998; Swenson and Wahr, 2006). The scaling factor was applied to minimize the attenuation in TWS signal due to the post-processing of GRACE data (Landerer and Swenson 2012; Long et al. 2015).

The contribution of the surface water to the Dakhla subbasin $GRACE_{TWS}$ was omitted by subtracting the $GRACE_{TWS}$ of a 120 km buffer zone surrounding Lake Nasser and the Tushka lakes (Fig. 2). This approach not only removes the contribution of the surface water, but also the contribution of the infiltration from the surface water in the immediate surroundings of Lake

Nasser and the Tushka lakes. A calibrated two-dimensional groundwater flow model which was constructed to investigate the long-term hydrologic impacts of Lake Nasser in southwest Egypt revealed substantial infiltration in the immediate vicinity (<30 km) of the Lake amounting to 60 x km^3 between years 1970 and 1984 and 40 x km^3 between 1987 and 2000 (Sultan et al ., 2013).

The periods used for the extraction of $GRACE_{TWS}$ trends were as follows: entire period (April 2002 through June 2016), dry (2002 through 2012), and wet (2013 through 2016) periods. The break points between the wet and dry periods were identified for each of the investigated subbasins using the Regime Shift Detection (RSD) method (Andersen et al., 2009; Reeves et al., 2007; Rodionov, 2004; Villarini et al., 2009).The phase image was generated by simultaneously fitting an annual cycle (sine and cosine) and trend terms for each $GRACE_{TWS}$ time series. The phase for each pixel is then calculated as the time (January to December) during which the maximum value was reached in the extracted annual cycle.

3.3.2 Geophysical data

The tilt derivative (TDR) filter was applied to the gravity data derived from the Eigen-6C4 GGM; the latter was found to have the least deviation (9.122 mGal) from the terrestrial gravity data for the study area (Appendix A). A GGM is a model of the gravity field obtained by converting the observed gravity data (often sparse in this region) to a set of spherical harmonic coefficients which then can be evaluated at any position, even where there were no observation points. Thus, it is a smoothed, interpolated approximation to the actual gravity field. The applied approach (selection of model showing minimum deviation from terrestrial gravity data) was adopted after Elsaka et al., (2016).

The TDR is a normalized phase derivative with first-order derivatives (Miller and Singh, 1994; Verduzco et al., 2004; Fairhead et al., 2011) and is defined as:

$$\text{Tilt derivative} = \tan^{-1}[\text{VDR}/\text{THDR}] \quad (1)$$

Where, the VDR is the vertical derivative, and THDR is the total horizontal derivative. Due to the nature of the arctan trigonometric function, all amplitudes are restricted to values between $+\pi/2$ and $-\pi/2$ regardless of the amplitudes of the VDR and THDR (Verduzco et al., 2004; Fairhead et al., 2011). The TDR is independent of absolute density since the VDR and THDR are functions of the density of the subsurface. The derivative is a powerful tool to identify subsurface structural edges (not absolute density or magnetization), where the zero tilt indicates the location of rapid lateral changes in the density of basement materials (Oruc, 2010).

3.3.3 Geochemistry and isotopic composition of water samples

We collected 21 groundwater samples from wells tapping the NSAS in southern Dakhla subbasin for isotopic analyses (H and O; Table 1; Figs. 8b, 9). The depth to water table (DWT) in the sampled wells ranged from 50 to 110 m. The wells were pumped for a minimum of 20 to 30 minutes before sampling of groundwater that were collected in 100 ml, tightly capped, polyethylene bottles. Stable isotope ratios of H and O in water were measured at the Stable Isotope Geochemistry Lab, Western Michigan University, USA, using Los Gatos Research (LGR) Off–Axis Integrated Cavity Output spectroscopy (off–Axis ICOS) technology. The isotopic data for samples are reported (Table 1) using the conventional delta (δ) notation, in units of permil (‰) deviation relative to Vienna standard mean ocean water (V-SMOW; Coplen, 1996), whereby

$$\delta_{\text{sample}}\ (‰) = [R_{\text{sample}}/R_{\text{standard}} - 1]*10^3 \qquad (2)$$

and

$$R = {}^{2}\text{H}/{}^{1}\text{H} \text{ or } {}^{18}\text{O}/{}^{16}\text{O} \qquad (3)$$

For comparison purposes, we included additional reported analyses for groundwater samples from the Western Desert (Patterson et al., 2005; Thorweihe, 1986), and the Northern Sudan

Table 1: Locations and O and H isotopic compositions for groundwater samples from wells tapping the NSAS in the southern parts of the Western Desert and in areas proximal to Lake Nasser

Sample ID	Name	Area	Longitude E	Latitude N	δ D (‰)	δ ^{18}O (‰)
WD7F-3	Seal PNK	Lake Nasser	32.44000	23.5600	−50.2	−5.69
WD7F-4	Kurkr	Lake Nasser	32.74091	23.98783	−70.1	−8.72
WD7F-5	Khor Galal	Lake Nasser	32.71683	23.77234	−76.6	−9.09
WD7F-6	GW1	Lake Nasser	32.57000	23.39000	−79.4	−10.14
WD7F-7	PSK	Lake Nasser	32.45000	23.50000	−77.4	−10.04
WD7F-9	Garef Hussien	Lake Nasser	31.99975	22.81808	−72.6	−9.17
WD7F-23	Research Desert 2	Lake Nasser	31.51756	22.53808	−81.0	−10.17
WD7F-24	Magnetic Station	Lake Nasser	31.54392	22.49089	−84.2	−10.58
WD7F-8	DW3	Lake Nasser	32.84366	23.34897	7.1	0.77
WD7F-11	East Oweinat 3	East Uweinat	28.68989	22.20419	−79.5	−10.21
WD7F-12	East Oweinat 5	East Uweinat	28.64700	22.19136	−79.7	−10.15
WD7F-13	East Oweinat 7	East Uweinat	28.65386	22.19406	−82.2	−10.53
WD7F-14	East Oweinat 9	East Uweinat	28.64017	22.18939	−81.5	−10.54
WD7F-15	East Oweinat 11	East Uweinat	28.62564	22.18514	−81.1	−10.33
WD7F-16	East Oweinat 12	East Uweinat	28.59178	22.17639	−81.5	−10.38
WD7F-17	East Oweinat 13	East Uweinat	28.58586	22.17297	−80.6	−10.09
WD7F-18	East Oweinat 16	East Uweinat	28.67961	22.21419	−80.4	−10.24
WD7F-19	East Oweinat 14	East Uweinat	28.68903	22.21703	−81.0	−10.34
WD7F-20	Army	East Uweinat	28.70262	22.45915	−82.4	−10.64
WD7F-21	Darb Al Arbaein 1	Darb Al Arbaein	29.73906	22.31775	−75.1	−9.28
WD7F-22	Darb Al Arbaein 2	Darb Al Arbaein	29.74925	22.32800	−80.7	−10.16

Platform (Thorweihe, 1986), surface water samples from Lake Nasser (Aly et al., 1993), and precipitation over the Northern Sudan Platform (Joseph et al., 1992).

3.4 Results and Discussion

Fig. 2 shows the spatial distribution of the secular trends in $GRACE_{TWS}$ data over the NSAS and its subbasins throughout two climatic periods: a dry period extending from 2002 to 2012, followed by a wet period from 2013 to 2016. Fig. 3 shows the $GRACE_{TWS}$ time series over the Dakhla, the Northern Sudan Platform subbasins, and the Kufra sections. Positive trends indicate an increase in $GRACE_{TWS}$ with time, and negative trends indicate the opposite (Fig. 3 and Table 2). The Dakhla subbasin shows a depletion in $GRACE_{TWS}$ (-3.8 ± 1.3 mm/yr) during the period 2002 to 2012, followed by an increase in $GRACE_{TWS}$ of 7.8 ± 1 mm/yr during the period 2013 to 2016. The Northern Sudan Platform shows a near steady state (-1.0 ± 1.2 mm/yr) during the earlier followed by an increase during the later period (7.4 ± 0.3 mm/yr). The Southern Kufra section shows patterns similar to those of the Northern Sudan Platform, a near steady state (-0.5 ± 1 mm/yr) during the earlier period followed by an increase in the later period (9.1 ± 2.2mm/yr). The Northern Kufra section shows a pattern similar to the Dakhla basin, a depletion (-2.5 ± 2.2 mm/yr) followed by an increase in $GRACE_{TWS}$ (10.4 ± 1 mm/yr).

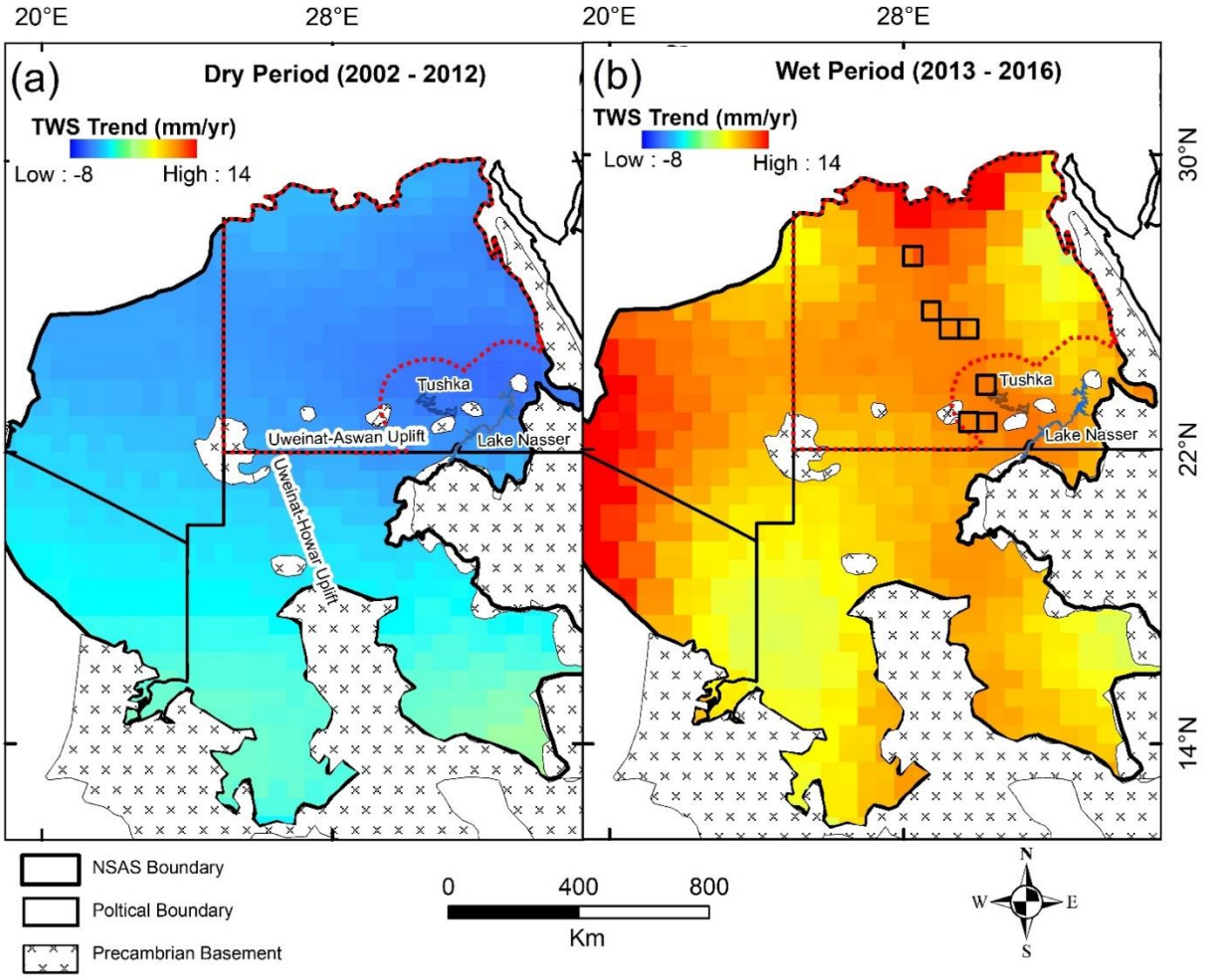

Figure 2. Secular $GRACE_{TWS}$ trend image (mm/yr) over the NSAS. (a) Dry period (2002–2012). (b) Wet period (2013–2016). The red dashed line shows the distribution of the Dakhla subbasin less a polygon defined by a 120 km wide buffer zone surrounding Lake Nasser and the Tushka lakes. Also shown are the locations of 7 areas (outlined by black boxes) displaying temporal variations in soil moisture content similar to those observed over Wadi El-Batikh (Fig. 1 and Fig. 5a).

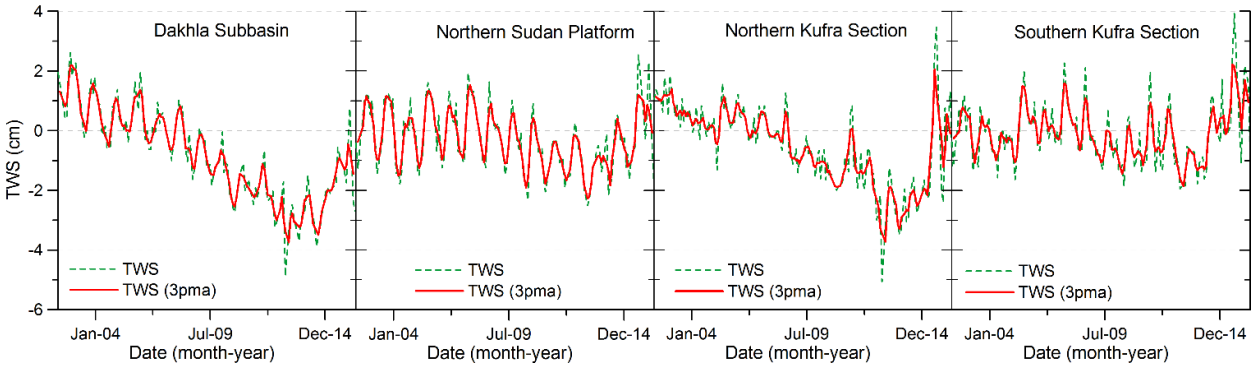

Figure 3. $GRACE_{TWS}$ time series over Dakhla subbasin, Northern Sudan Platform, and Northern and Southern Kufra sections with three point moving average (3pma).

Table 2: Precipitation and Terrestrial Water Storage over the NSAS throughout the dry (2002–2012) and wet (2013–2016) periods

Area	**Area**	**Dry Period (2002–2012)**				**Wet Period (2013–2016)**			
		†ΔTWS		#AAP		†ΔTWS		#AAP	
	km²	**mm/yr**	**km³/yr**	**mm/yr**	**km³/yr**	**mm/yr**	**km³/yr**	**mm/yr**	**km³/yr**
Dakhla sub-basin	67x10⁴	−3.8 ±1.3	−2.5 ±0.9	7.5	5	7.8±1	5.2 ±0.7	9.5	6.4
Southern Kufra section	64 x10⁴	−0.5 ±1	−0.3 ±.06	92	59.5	9.1±2.2	5.9 ±1.4	115	74.3
Northern Kufra section	25 x10⁴	−2.5 ±2.2	−0.6 ±0.6	6.5	1.7	10.4 ±1	2.7 ±0.3	6.7	1.7
Northern Sudan platform	43 x10⁴	−1 ±1.2	−0.5 ±0.6	78	34.2	7.4±0.3	3.3 ±0.1	99	43.5

†ΔTWS: Change in terrestrial water storage.

#AAP: Average Annual Precipitation.

The observed increase in $GRACE_{TWS}$ in the Northern Sudan Platform and in the Southern Kufra during the wet period could be explained by an increase in precipitation during this period. The AAP over the Northern Sudan Platform during the wet period was high (99 mm/yr) compared to that during the earlier dry period (78 mm/yr), an increase of 27% (Table 2; Fig. 4(a)). A similar

increase in precipitation was observed over the Southern Kufra during the wet period (Table 2; AAP for wet period: 115 mm/yr; dry period: 92 mm/yr). By contrast, the AAP over the Dakhla subbasin was negligible during the dry (7.5 mm/yr) and wet periods (9.5 mm/yr), as was the precipitation over Northern Kufra section (Table 2; AAP for wet period: 6.7 mm/yr; dry period: 6.5 mm/yr). The increase in $GRACE_{TWS}$ over the Dakhla subbasin in the wet period amounted to 7.8 ±1 mm/yr (total of 31.2 mm throughout the wet period) and over the Northern Kufra section it was 10.4 ±1 mm/yr (total of 41.6 mm throughout the wet period). Going from the dry to the wet period, the AAP increased by 2mm/yr (total of 8mm throughout wet period) over the Dakhla subbasin and by 0.2 mm/yr (total of 0.8 mm throughout wet period) over the Northern Kufra. Previous work has shown that recharge in the Egyptian deserts ranges from 11 to 31% of the total precipitation (Milewski et al., 2009). Even if we were to assume that all the added precipitation during the wet period ended up as recharge, we still cannot account for the observed increase in $GRACE_{TWS}$ over the Dakhla subbasin and the Northern Kufra section. Thus, the observed increase in $GRACE_{TWS}$ over these two areas during the wet period cannot be attributed to an increase in precipitation, nor could it be due to an increase in soil moisture, given that precipitation remained negligible throughout the investigated period (Appendix A). The observed increase in $GRACE_{TWS}$ will have to be related to an increase in surface and/or groundwater storage.

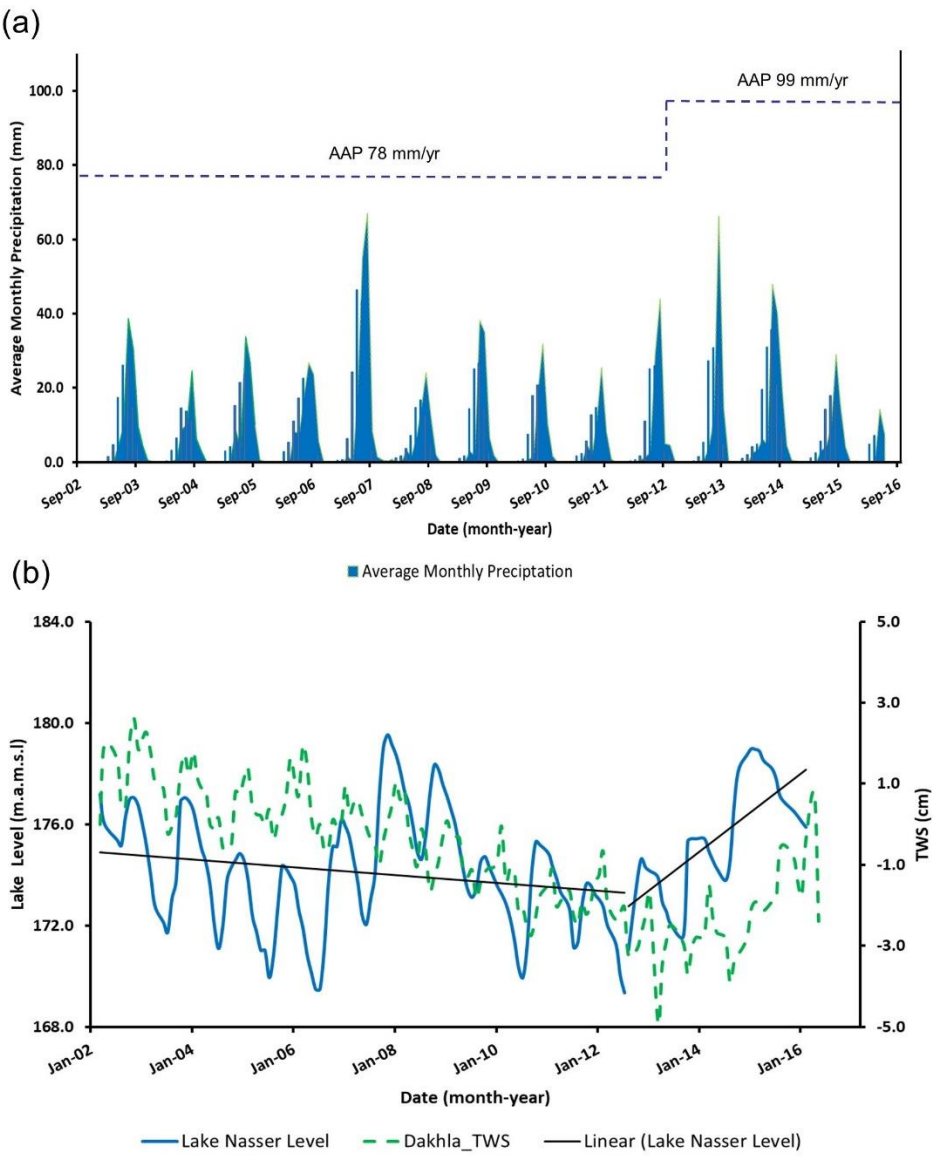

Figure 4. (a) Average monthly and annual precipitation over the Northern Sudan Platform extracted from TRMM data for the dry and wet periods. (b) Time series for Lake Nasser surface water level (2002–2016) extracted from the GRLM database. For comparison, the $GRACE_{TWS}$ time series over the Dakhla subbasin is provided.

There are no major rivers in the Northern Kufra section, and thus the observed increase in $GRACE_{TWS}$ in the Northern Kufra section during the wet period would have to be due to

groundwater flow from the Southern Kufra section. There is one major river that flows in the Dakhla basin, the Nile (Fig. 1). During the wet periods one would expect increased runoff from the source areas in the Ethiopian highlands, impoundment of excess Nile River water in Lake Nasser, elevated lake levels, and an increase in the surface water storage. Investigating the time series of Lake Nasser level fluctuations for the period between 2002 and 2016 (Fig. 4(b)) indicated that indeed this is the case. We observe a progressive rise in average annual lake levels from 172 m.a.m.s.l. in 2012 to 178 m.a.m.s.l in 2015 (Fig. 4(b)) as well as an increase in its area. Examination of the temporal Landsat thematic mapper (TM) data over Lake Nasser revealed that its area increased from 3622 km^2 in 2012 to 4530 km^2 in 2016. Likewise, $GRACE_{TWS}$ trends for a 120 km wide polygon centered over Lake Nasser increased from -4.1 ± 0.3 mm/yr (-0.2 ± 0.01 km^3/yr) during the dry period to 8.6 ± 1.5 mm/yr (0.5 ± 0.08 km^3/yr) in the wet period. One would also expect increased infiltration and recharge, a rise in groundwater levels, and enhanced down-gradient groundwater flow during wet periods. Using a calibrated two-dimensional groundwater flow model, Sultan et al., (2013) investigated the long-term hydrologic impacts of Lake Nasser in southwest Egypt. Their model outputs showed that during a similar rise in Lake Nasser surface water levels (water levels: 170 meters above mean sea level [m.a.m.s.l] in 1992; 179 m.a.m.s.l in 1995) recharge increased from 0.7 km^3/yr to 6 km^3/yr. We attribute the increase in $GRACE_{TWS}$ in the Dakhla subbasin during the wet period to increased infiltration and groundwater flow from Lake Nasser and from Northern Sudan as well.

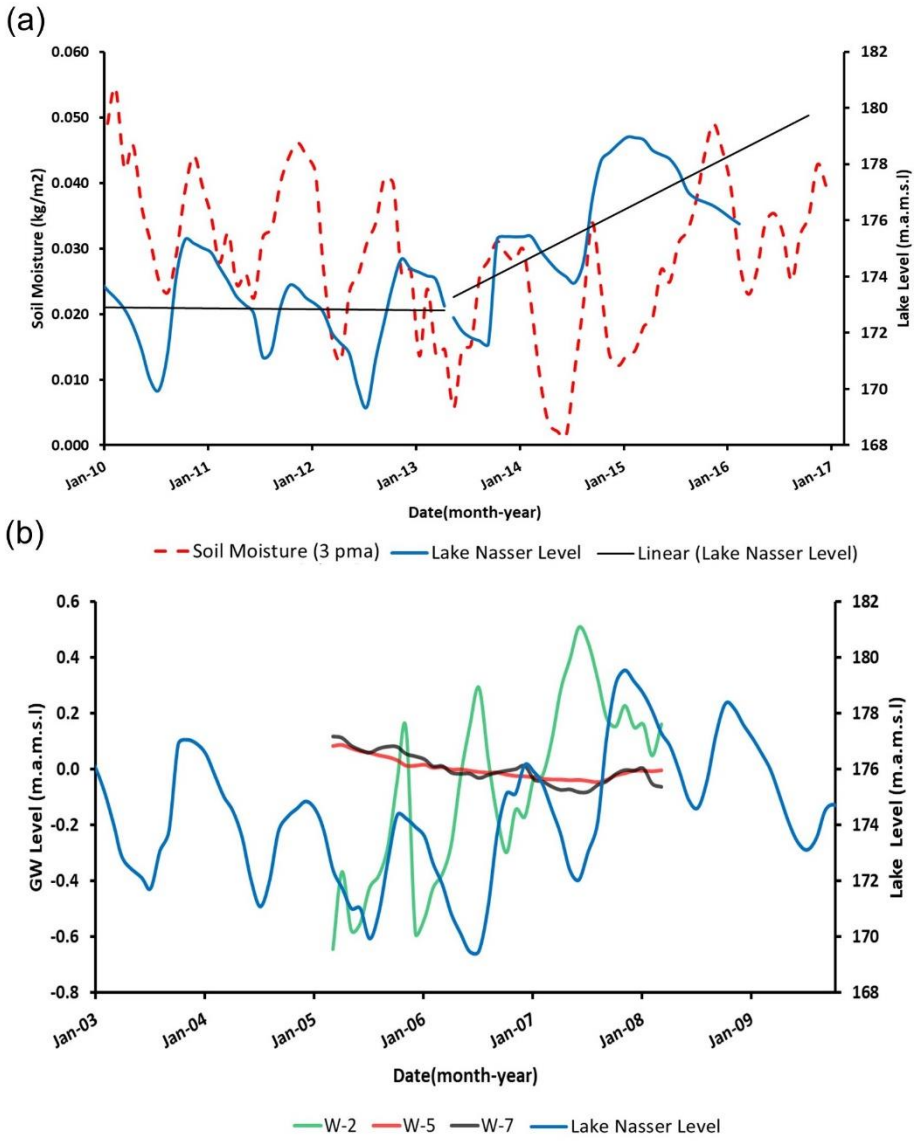

Figure 5. Rapid response in groundwater level and soil moisture to fluctuations in Lake Nasser surface water levels. (a) Comparison of monthly (April 2005 to April 2008) soil moisture content from SMOS data acquired over Wadi El-Batikh with Lake Nasser surface water levels. (b) Comparison of monitoring well data (Wells # W-2, W-5 and W-7; 2005 to 2008) in East Uweinat area and surroundings to Lake Nasser surface water levels.

We test the above-mentioned hypothesis (the nature of the source areas) and the direction and extent of mass movement during dry and wet periods using phase and difference images extracted from temporal $GRACE_{TWS}$ data. The phase diagrams display the month in which the maximum $GRACE_{TWS}$ value was attained for each pixel, in the dry period (Fig. 6(a)), and in the wet period (Fig. 6(b)). Fig. 6(a) shows that Lake Nasser and its surroundings, extending some 600 km to the west and 300 km to the north, attained their maximum $GRACE_{TWS}$ values in the month of January. To the north and northwest of these areas, phase values transition from the month of January to February, then March followed by April, and ending by the month of July in the extreme northwest of the Dakhla subbasin. The observed phase over Lake Nasser and its immediate surroundings are to be expected given that the lake surface water levels peak in the months of December and January (Figs. 4 and 5). One interpretation that is consistent with the observed phase patterns during the dry period is that Lake Nasser is the main source of recharge, with modest to minimal recharge from the south, and that mass movement is extensive and rapid (hundreds of km/yr along preferred directions). During the wet period, a maximum phase is observed over Lake Nasser in the same approximate period (December instead of January), yet the progressive transition in phase from Lake Nasser outwards throughout major sections of the Dakhla subbasin that was observed during the dry period is absent. Instead, we observe a maximum phase over source areas in northern Sudan (south of the 20 mm threshold precipitation line) during the reported peak precipitation periods (August and September; Fig. 4(a)). To the north and northeast of this area the phase transitions progressively from the months of September/August to October, followed by November, and ends up in December to the east and northeast of the Dakhla subbasin, where apparently recharge from Lake Nasser is underway at the same approximate time period (December) in the year. One plausible interpretation of these patterns is that during wet periods, the Dakhla subbasin receives rapid and extensive groundwater flow from the Northern Sudan Platform and from Lake Nasser. The inferred rapid overall groundwater flow directions in both the wet and dry periods are represented by black arrows on Fig. 6. The lines satisfy a number of conditions: they originate from the proposed sources areas, a progressive increase in phase and decrease in amplitude is observed along their length, and they terminate where the advocated phase transitions are disrupted.

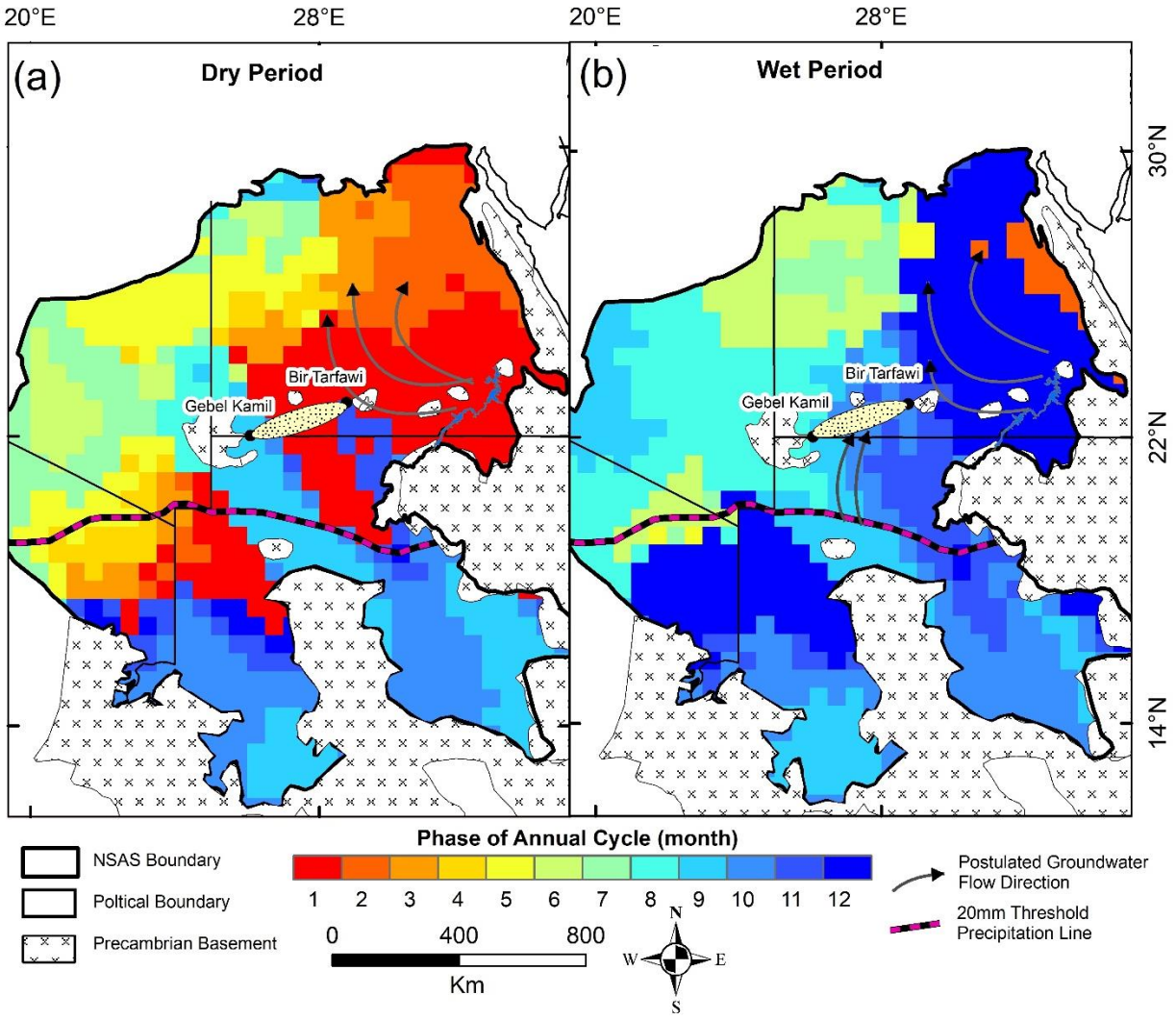

Figure 6. The phase of the annual cycle derived from $GRACE_{TWS}$. (a) Phase during the dry period (2003–2012). (b) Phase during the wet period (2013–2015). The months of the year are represented by numbers (January: 1; December: 12).

If the advanced conceptual model is true, one would expect to observe a progressive increase in the $GRACE_{TWS}$ downgradient from the source areas, namely from the Southern Kufra section

towards the Northern Kufra section and from the Northern Sudan Platform and from Lake Nasser towards the Dakhla subbasin throughout the wet period. One way to examine these postulated spatial variations in $GRACE_{TWS}$ throughout the wet period is through the construction of difference images between the average annual $GRACE_{TWS}$ (AA $GRACE_{TWS}$) for: (1) 2013 and 2012 (Fig. 7(a)), (2) 2014 and 2012 (Fig. 7(b)), and (3) 2015 and 2012 (Fig. 7(c)). Inspection of Fig. 7 shows a progressive increase in $GRACE_{TWS}$ and mass movement from the source areas, namely Lake Nasser, and from northern Sudan towards the Dakhla subbasin. Comparison of Figs. 7 (a–c) shows that by 2015, almost all the Dakhla subbasin shows an overall increase in $GRACE_{TWS}$, with the largest increase (>20 mm) observed over areas extending up to 400 km from the source areas (Lake Nasser and areas south of the 20 mm AAP threshold line; Fig. 7(c)). These distances are represented by the length of the dashed arrows in Fig. 7(c). It is here assumed that recharge of the NSAS will occur in areas to the south of the line but not to the north of it, where the limited precipitation is less likely to recharge the NSAS and more likely to be lost to evaporation. It is worth mentioning that the groundwater flow from the Northern Sudan Platform subbasin to the Dakhla subbasin is limited during the dry periods, given the presence of an east-west–trending basement uplift, the Uweinat-Aswa (Mohamed et al., 2017). Apparently, though, the flow becomes less restricted during the wet periods along windows found in areas within the uplift, where the basement is deep, the aquifer is thick. One of these windows is found to the east of the Uweinat outcrop at the borders of Egypt, Sudan, and Libya (Fig. 1); the window is 225 km wide (Fig. 6), the basement at this location is up to 370 m deep, and the average depth to water table is 10–50 m (Mohamed et al., 2017).

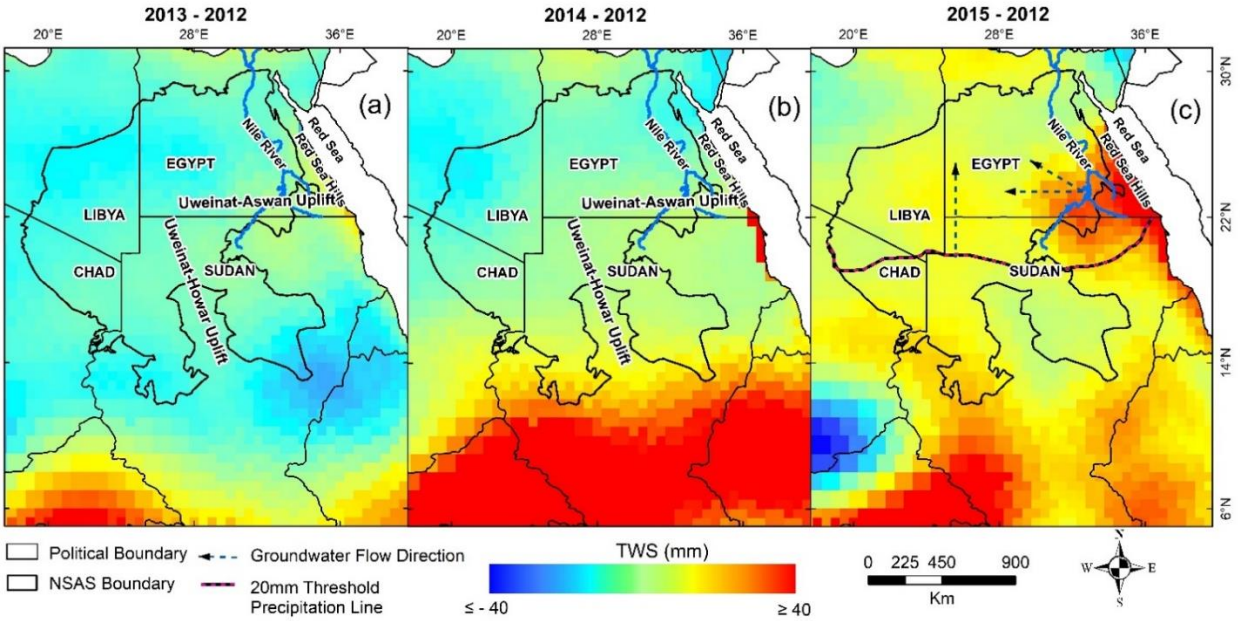

Figure 7. Difference images showing a progressive increase in TWS and mass movement during the wet period from the south to the north and from Lake Nasser to its surroundings. (a) Difference image between the AA $GRACE_{TWS}$ for 2013 and that for 2012. (b) Difference image between the AA $GRACE_{TWS}$ for 2014 and that for 2012. (c) Difference image between AA $GRACE_{TWS}$ 2015 and that for 2012. Also shown is the 20 mm AAP threshold line and groundwater flow distances measured from the source areas (Lake Nasser and areas receiving AAP > 20 mm in Northern Sudan Platform), represented by the length of arrows.

Additional evidence for the advocated model comes from the rapid response in groundwater levels in wells distant from Lake Nasser that are located along, or proximal to, the preferred pathways for groundwater flow and by a similar rapid response in the soil moisture content within areas characterized by near-surface groundwater levels (< 2m). One of these areas is Wadi El-Battikh (refer to Figs. 1 and 8(b) for location). It is located some 450 km to the west of Lake Nasser and 600 km from the potential source areas in northern Sudan (Fig. 1); because of its shallow groundwater table, farmers grow watermelons in these areas. Fig. 5(a) shows a general correspondence between the soil moisture content in Wadi El-Battikh and Lake Nasser surface

water levels. For example, Lake Nasser surface water levels started to rise from 170 m in August 2012 and peaked at 179 m in April 2015; for the following three years (2012 to 2015), soil moisture fluctuations in Wadi El Battikh corresponded to those in Lake Nasser, but lagged by 6–8 months. The Wadi El-Batikh area is characterized by major faults (northwest-southeast trending faults; El-Hinnawi et al., 2005; Fig. 8(b)) where these faults intersect the escarpment, promontories, and embayments at theater head valleys, indicating groundwater discharge along the extension of these faults (Abotalib et al., 2016). Several locations within the Western Desert display temporal variations in soil moisture content similar to those observed over Wadi El-Batikh. Specifically, they show stable or decreasing soil moisture content during the dry period followed by an increase during the wet period. Seven of these locations are displayed in Fig. 2b. The identified locations are all in lowlands, in areas where groundwater levels are shallow, and where sub-vertical, deep-seated faults were mapped; the faults act as conduits for ascending deep groundwater within the confined sections of the NSAS (Abotalib et al., 2016).

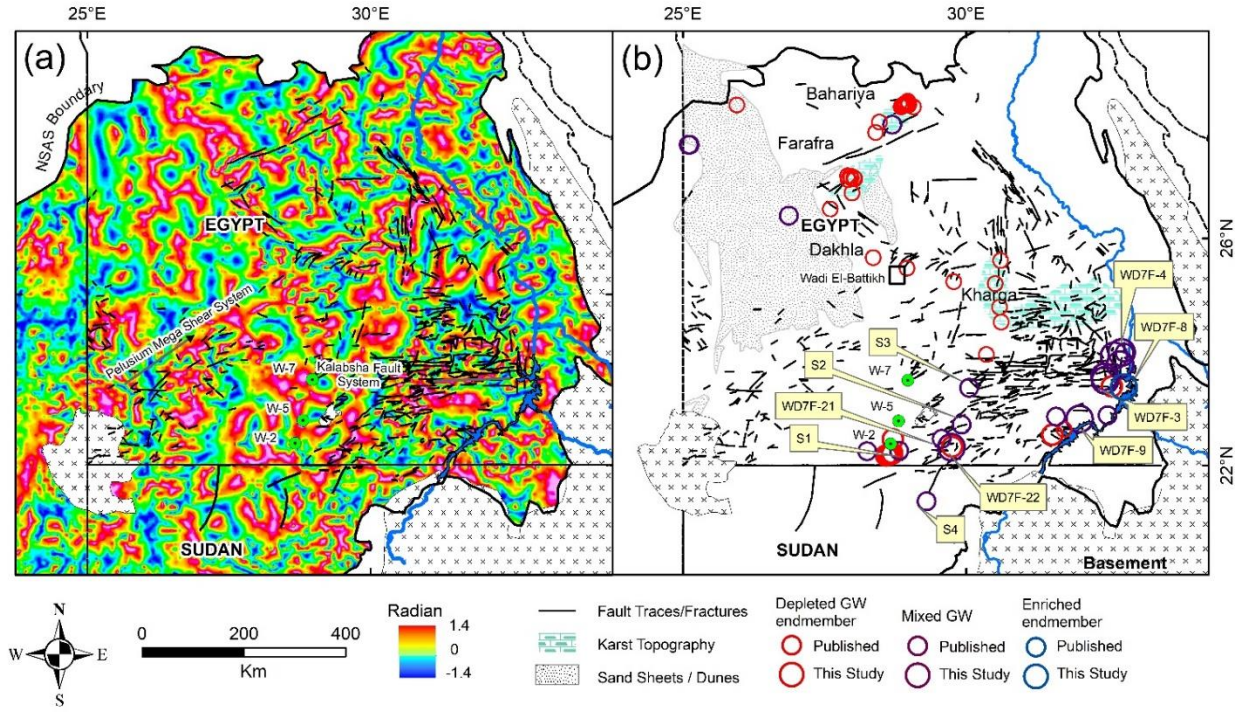

Figure 8. (a) TDR image showing the distribution of inferred deep-seated northwest, northeast, north-south, and east-west trending lithologic contacts and/or faults mapped along zero-tilt lineaments (yellow colors). (b) Interpretation map showing the distribution of fault traces and fractures (El-Hinnawi et al., 2006, 2005; GRAS, 1988). Note the correspondence of the zero-tilt lineaments with the fault traces. The complex of intersecting structures can represent preferred pathways for groundwater flow. Also shown are the spatial distribution of color-coded isotopic compositions for our groundwater samples (large open circles) from productive wells tapping the NSAS and reported isotopic compositions for the NSAS paleowaters from the Western Desert (small open circles).

A similar correspondence and rapid response to fluctuations in Lake Nasser was observed in a monitoring well (well W-2) located some 280 km to the west of Lake Nasser (Figs. 1 and 8(b)). A rise in the lake's surface water level started in August 2005 and peaked at 179 m in January 2008; for the following three years (April 2005 to April 2008), fluctuations in groundwater levels in well W-2 corresponded to those in Lake Nasser, but lagged by 4–6 months (Fig. 5(b)). In contrast, two other proximal wells (W-5 and W-7, <150 km from well W-2) showed no response to fluctuations in Lake Nasser surface water levels (Fig. 5(b)). One interpretation for the reported differences in monitoring well response is that well W-2, but not wells W-5 and W-7, is probably located along the postulated extension of the east-west trending Kalabsha fault system, or along the extension of a northeast-trending strand of the Pelusiam fault system (Fig. 8(b)), both considered here to be potential preferred pathways for groundwater flow. One should expect a general (but not a one-to-one) correspondence between the lag time extracted from the phase analysis of $GRACE_{TWS}$ and that extracted from the groundwater levels and soil moisture data. The former provides the average lag time over large areas, whereas the latter reflects the local nature of the flow pathways that feed the examined locations. Unfortunately, very limited monitoring well data is available for the Western desert of Egypt temporally and spatially to further test our suggestions.

If the advocated seasonal and interannual mass movements in the wet and dry years are valid, one would have to invoke a rapid mass movement of hundreds of kilometers in the investigated periods. That is difficult to reconcile if the groundwater flow was through porous media under laminar Darcian flow, even if the media had exceptionally high effective porosity and permeability. One way to achieve this rapid mass movement is for groundwater flow to occur as rapid turbulent non-Darcian flow within high transmissivity zones within fractured systems (faults/shear zones) and karstic textures. Very high hydraulic conductivities (0.01 to 1 m/s; Bear, 1972) were reported for densely fractured bedrocks using integrated theoretical and experimental approaches. Tracer experiments in fractured aquifers indicated that groundwater flow could attain velocities several orders of magnitude higher than natural groundwater flow through porous media (Lapcevic et al., 1999), and the flow velocity in the individual fractures can be extremely high (>1 m/s; Kohl et al., 1997). Such high flow velocities in fractures are maximized within areas characterized by high hydraulic gradients such as those surrounding dam-generated artificial lakes (Qian et al., 2005), Lake Nasser being one of these areas (hydraulic gradient: 0.0014; Alfaran, 2013). Groundwater flow velocities exceeding 2 km/day were measured in fissured and karstic chalk aquifers in the Hampshire Basin, south Hampshire (Atkinson & Smith, 1974). Using a tracer test, Banks et al. (1995) measured similar high groundwater flow velocities (5.8–6.8 km/day) in a karstic system within a chalk aquifer in Stanford Dingley, Berkshire, in southern England. They attributed these high velocities to secondary fissure flow systems developed by preferential dissolution along discontinuities (e.g., bedding planes and fractures) producing high transmissivity zones (Banks et al., 1995). The advocated rapid flow for the NSAS contrasts with the much slower flow (0.05–0.5 cm/day) within the Nubian Sandstone matrix (Patterson et al., 2005; Sturchio et al., 2004; Sultan et al., 2013). It is the former type of groundwater flow, not the latter, that is causing the observed temporal and spatial variations in $GRACE_{TWS}$ during the wet period in the Dakhla subbasin and in the Northern Kufra section. For this to be true, one would expect to observe extensive networks of interconnected structures and/or karstic topography.

The Dakhla subbasin is dissected by sub-vertical, deep-seated basement faults, many of which were reactivated by later tectonic activities (Neev et al., 1982; Sultan et al., 2007a). These

include: (1) north-south—trending accretionary structures, (2) northwest-southeast—trending Najd faults in the eastern sections of the Western Desert, (3) east-west—trending Kalabsha and Seiyal fault systems in the southern parts of the Western Desert, and (4) northeast-southwest—trending Pelusium faults in the western sections of the Western Desert (Hermina, 1990; Khan et al., 2014; Neev, 1975; Neev et al., 1982; Thurmond et al., 2004). We correlated the distribution of fault traces and fractures (El-Hinnawi et al., 2006, 2005; GRAS, 1988) with potential fault locations extracted from TDR maps of gravity data (Oruc, 2010; Verduzco et al., 2004). The TDR filter was applied to enhance the geophysical signal of the basement structures (Oruc, 2010). The TDR filter was applied to the gravity data derived from Eigen-6C4 GGM; the latter was found to have the least deviation (9.122 mGal) from the terrestrial gravity data (21,262 sites) for the study area. The applied approach (selection of model showing minimum deviation from terrestrial gravity data) was adopted after Elsaka et al., (2016).

Fig. 8(a) is a TDR map for the Dakhla subbasin and surroundings showing radian values between – 1.4, 0, and + 1.4. On this map the red color reflects positive tilt values, the blue shades indicate negative tilt values, and the yellow colors delineate areas with zero tilt. The zero-tilt lineaments could indicate the location of lithologic contacts and/or faults (Verduzco et al., 2004; Oruc, 2010). Also plotted on Fig. 8 are fault traces exceeding 10 km in length (El-Hinnawi et al., 2005, 2006). Fig. 8(a) shows numerous north-south, northwest-southeast, northeast-southwest, and east-west trending linear features, and many of the zero-tilt lineaments coincide with the mapped fault traces. Inspection of geologic maps (e.g., Conco, 1987; El-Hinnawi et al., 2005, 2006), and our analysis of satellite imagery (Landsat TM) revealed that large sections of the Western Desert are covered by sand dunes and sheets, and thus fault traces were only mapped in the dune and sand sheet-free areas (Fig. 8(b)). Approximately two-thirds of the Dakhla subbasin is covered by marine limestone plateau which extends west of the Nile Valley (Fig. 1; Conco, 1987). The limestone outcrops are largely formed of Cretaceous chalk and Eocene limestone, many of which were described as having karstic features (e.g., dissolution caves, speleothems, chalk pillars, and flowstones). The karstic features were reported along fractures and joints west of Lake Nasser (e.g., El Gammal, 2010; Halliday, 2003; Ruggeri, 2001; Waltham, 2001), along, and proximal to, the road from the Farafra Oasis to the Bahariya Oasis, in the Kharga and Siwa depressions, and

from the Kurkur area (Figs. 1 and 3(b); Aref et al., 1987; Butzer, 1965; El Gammal, 2010; Mostafa, 2013; Ruggieri, 2001; Waltham, 2001). The high inferred groundwater flow velocities for the NSAS is common in fractured and karstic aquifers. These reported faults and karst systems in the Dakhla subbasin represent preferred pathways (Mohamed et al., 2017) as well as vertical passages for groundwater connection between the NAS and the overlying PNAS (Abotalib et al., 2019; Mohamed et al., 2017). Given the densely mapped fault and karst networks, and building on the observations extracted from GRACE, altimetry, SMOS, and monitoring well data, we advocate similar systems in our study area, where extensive networks of deep-seated fault systems and karstic topography provide preferred and rapid pathways (or hydraulic conduits) for groundwater flow across large sections of the Dakhla subbasin.

If our conceptual model is true one could expect the isotopic composition of groundwater within, or proximal to, the preferred pathways to reflect mixing between depleted NSAS groundwater and modern waters from Lake Nasser and from precipitation over recharge areas in the Northern Sudan Platform. The isotopic composition of the collected samples were compared to those of Lake Nasser surface water (Aly et al., 1993), modern precipitation (mean ± 1 Standard Deviation [1S]: δD: −10.0 ± 15.7‰; $\delta^{18}O$: −2.09 ± 2.3‰) over recharge areas in the Northern Sudan Platform (Joseph et al., 1992), and reported groundwater composition (Patterson et al., 2005; Thorweihe, 1986) across the Western Desert (Figs. 8(b), 9). The majority of our groundwater samples (e.g., WD7F-20, WD7F-19, WD7F-18, WD7F7-24, and WD7F-23; Table 1, Fig. 9) had depleted isotopic compositions (δD: −84.2 to −80.4‰; $\delta^{18}O$: −10.6 to −10.1‰) that are typical of NSAS paleowater composition (Abotalib et al., 2016; Mohamed et al., 2017; Sultan et al., 2007b), whereas the composition of a number of our groundwater samples (e.g., WD7F-3, WD7F-4) from wells proximal (<30 km) to Lake Nasser are consistent with depleted NSAS groundwater mixing with enriched Lake Nasser water (Figs. 8(b), 9; Table 1). One of our groundwater samples (WD7F-8) that was collected only a few kilometers west of Lake Nasser yielded an isotopic composition (δD: 7.1‰; $\delta^{18}O$: 0.77‰) that approaches that of Lake Nasser surface water (Figs. 8(b), 9).

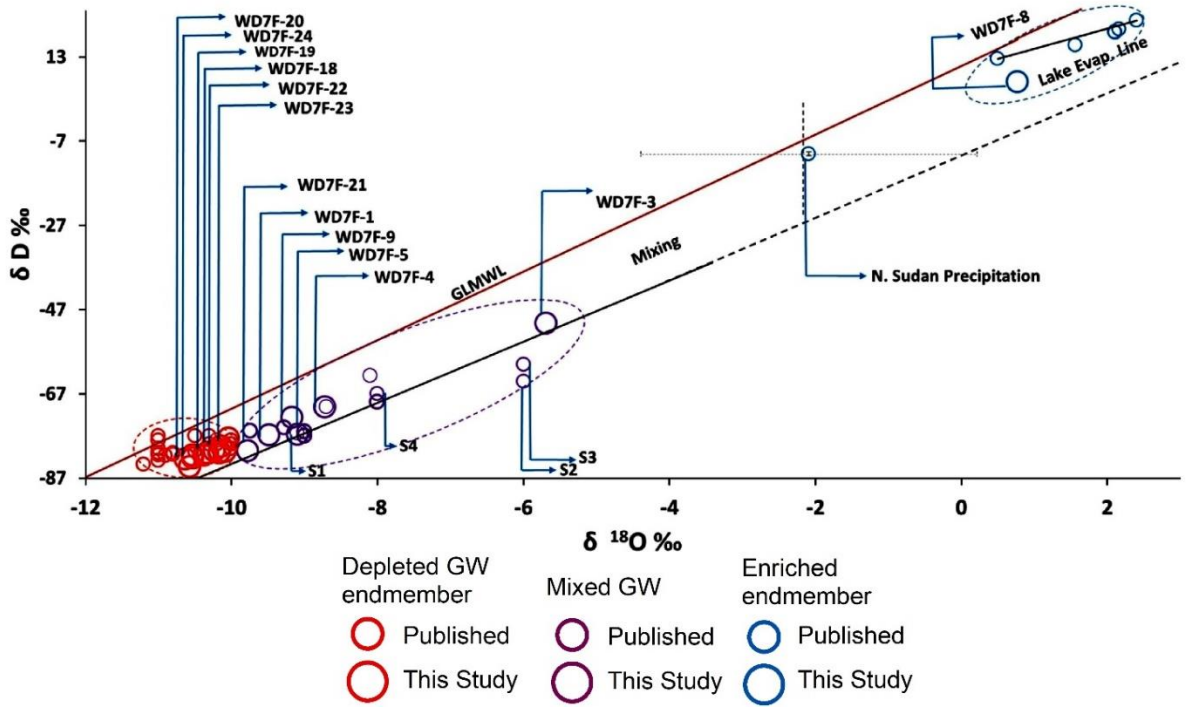

Figure 9. The isotopic composition of our samples (large open circles) plotted on a δD versus $\delta^{18}O$ plot and compared to groundwater (small open red and purple circles; Patterson et al., 2005; Thorweihe, 1986) and modern precipitation (open blue circle; mean ± 1 SD) from northern Sudan (Khartoum IAEA station; Joseph et al., 1992). Also shown are the paleo meteoric water line (MWL), $\delta D = 8\ \delta^{18}O + 6.3$ (Dietzel et al., 2014) and global meteoric water line (GMWL), $\delta D = 8\ \delta^{18}O + 10$ (Craig, 1961) and evaporation line for Lake Nasser (Aly et al., 1993).

A considerable number of groundwater samples, both ours and reported by others, from East Uweinat and Darb Al Arbaein (e.g., WD7F-21, S1, S2, and S3), approximately 200–300 km from Lake Nasser show evidence of mixing with a more enriched endmember (Figs. 8(b), 9). Although it is possible that the enriched samples in these two areas received contributions from Lake Nasser through infiltration and preferred groundwater flow along east-west trending faults and shear zones (Fig. 8), it is also possible that the source of their modern contributions is groundwater flow from the south that originated as modern precipitation over the Northern

Sudan Platform (Fig. 3). This hypothesis is supported by the observed similarity in isotopic compositions of enriched samples from East Uweinat and Darb Al Arbaein to samples (e.g., S4) from northern Sudan (Figs. 8(b), 9), and by the fact that the enriched compositions from East Uweinat could be explained by mixing between depleted NSAS groundwater and precipitation over northern Sudan (Fig. 9). Some of these enriched samples around Lake Nasser and in East Uweinat were collected only hundreds of meters away from others that yielded typical NSAS depleted isotopic signatures (e.g. WDF-21, 22; Figs. 8(b), 9). One likely explanation is that the former samples, not the latter samples, were collected from wells lying on, or proximal to, one of the preferred groundwater flow pathways.

During the wet periods, groundwater recharge intensifies through infiltrated precipitation in the south and through infiltration from Lake Nasser and mixes with the extensive depleted fossil groundwater of the NSAS. The total water reserves in the Dakhla subbasin are estimated at 154,716 km^3 (M Bakhbakhi, 2006), whereas the combined increase in $GRACE_{TWS}$ due to the groundwater flow from Lake Nasser and from the Northern Sudan Platform is here estimated at ~8.5 km^3/yr. Thus, one should not expect to observe evidence for mixing from samples collected across the entire Dakhla subbasin. Instead, evidence for mixing is likely to be detected in samples collected from wells that are located on, or proximal to, these preferential pathways. Examination of Fig. 3 supports this suggestion; a number of enriched samples (e.g., WD7F-9, WD7F-3, S3; Fig. 8(b)) lie on east-west trending faults originating at or near Lake Nasser, and others (e.g., S4, WD7F-21, S2, S3; Fig. 8(b)) lie on north-south trending faults originating in northern Sudan. TWS time series along the E-W fractures show uniform patterns along the pathways of the faults, and dissimilar patterns across the faults (Appendix A).

We offer a conceptual model (Fig. 10) that is consistent with the above-mentioned field and isotopic observations and our earlier GRACE-related temporal and spatial variations. We advocate that during the dry period, Lake Nasser is the main source of recharge for the Dakhla subbasin with modest to minimal recharge from the Northern Sudan Platform. The lake receives on an annual basis added river flow during the flood season (month of December/January) that increases Lake Nasser surface water level, infiltration, recharge, and groundwater flow from the

lake to the Dakhla subbasin. During the wet periods, Lake Nasser receives higher surface water flow compared to that received during dry periods, leading to excessive rise in Lake Nasser surface water level, infiltration, recharge, and groundwater flow from the lake to the Dakhla subbasin. In contrast to the dry periods, the Dakhla subbasin receives in the wet periods additional recharge from the south. Precipitation over the Northern Sudan Platform increases, as does infiltration, recharge, and groundwater flow from the south (Northern Sudan Platform) towards the Dakhla basin. During both the dry and wet periods, groundwater flow is rapid along preferred pathways (karst and fault-based conduit network) causing the increase in groundwater flow and storage of groundwater water in conduit network. This rapid groundwater flow, when it occurs, is detected as an increase in $GRACE_{TWS}$ over the Dakhla subbasin, whereas groundwater flow in the surrounding matrix is slow resulting in little change in matrix storage and is not responsible for the observed $GRACE_{TWS}$ variations in the Dakhla subbasin. We realize that none of the individual pieces of evidence presented in this study can, on its own, conclusively prove the validity of the advocated model, yet collectively they provide substantial evidence in support of the advocated model and merit additional investigations over aquifers of similar geologic and hydrogeologic settings worldwide.

Our findings, we believe, have significant implications for groundwater sustainability of the NSAS in general, and for the arid sectors of the aquifer in particular. The current perception of the aquifer as being formed entirely of non-renewable fossil water should be revisited, even in its arid sectors (Dakhla subbasin and Northern Kufra section).

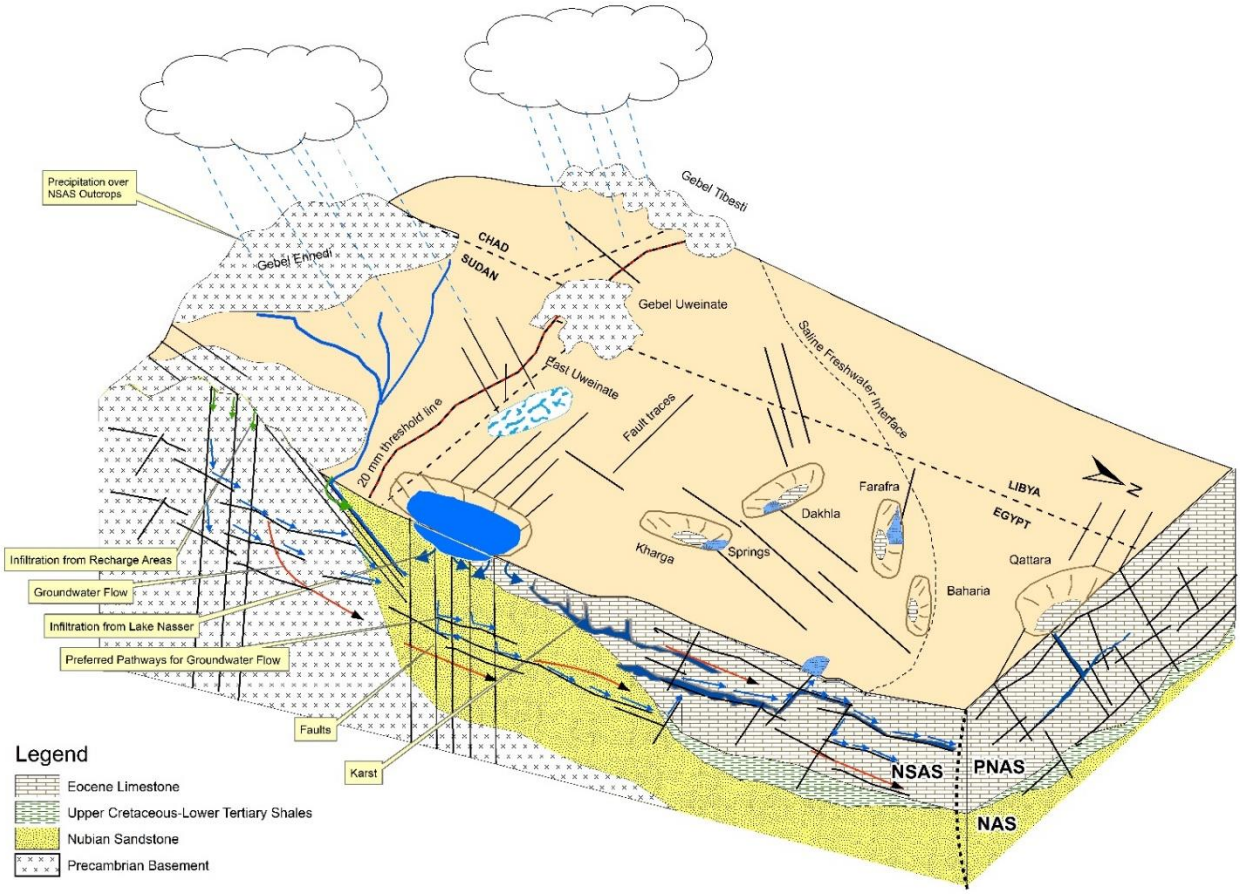

Figure 10. Block diagram showing our hydrological conceptual model for the NSAS where faults and karst serve as preferred groundwater flow conduits allowing groundwater flow to discharge areas. The figure shows on the surface and in cross section the locations of infiltration and recharge from precipitation in the Northern Sudan Platform south of the 20 mm AAP threshold line (green arrow) and from Lake Nasser (blue arrow), areas of natural discharge (oases in Western Desert), preferred pathways for groundwater flow (interconnected faults and karst topography), and groundwater flow direction flow (red arrows).

It should be also noted that the rapid groundwater flow in response to climatic variability observed over the NSAS and detected from GRACE data could be common to many of the fossil aquifers worldwide and might offer a viable explanation for the reported modern contributions in many of the deep aquifers elsewhere. While we believe that the response of deep aquifers to climatic variations remains a relatively slow process that takes thousands to tens of thousands of years, there is apparently a much faster response in aquifers that are characterized by dense networks of faults, fractures and karst as is the case with the NSAS. Examples of potential fossil aquifers which could be investigated for a similar rapid response to climate variability include the Saharan aquifer systems in North Africa and in the Arabian Peninsula. The largest of those aquifers is the Mega Aquifer System (area: 2×10^6 km^2; countries: Saudi Arabia, Oman, United Emirates, and Jordan) and the North Western Saharan Aquifer System (area: 1.2×10^6 km^2; countries: Algeria, Tunisia, and Libya). Additional smaller Saharan ($<900 \times 10^3$ km^2) aquifers include the Iullemeden Aquifer in Mali, Niger, Nigeria, Algeria and Benin and the Taoudeni Aquifer in Mauritania, Mali and Burkina Faso (Abotalib et al., 2016, Othman et al., 2018).

CHAPTER 4

WHAT CAN THE GRACE SEASONAL CYCLE TELL US ABOUT LAKE-AQUIFER INTERACTIONS?

4.1 Introduction

Sustainable utilization of freshwater systems is essential to ensure food security, as well as economic and political stability, particularly in semi-arid and arid regions. Central to these systems are freshwater lakes. Natural lakes contain 91×10^3 km^3 of freshwater (87% of global non-frozen surface freshwater; Gleick, 2000) and artificial lakes together with river systems add another 7 to 8×10^3 km^3 (Lehner et al., 2011. Recent attempts to integrate hydrological components of freshwater systems (e.g., surface water in lakes and rivers, groundwater, and aquatic ecosystems) into a single management scheme (Ala-aho et al., 2015) necessitates the development of new approaches to investigate the temporal and spatial variability in surface water–groundwater exchange on regional scales (Rosenberry et al., 2013).

Many characteristics can be used to distinguish between the groundwater–surface water exchange settings, the most common of which is lake level height. Depending on the differences between groundwater and lake water levels, the lakes can lose water to surrounding aquifers (recharge lakes), gain water from surrounding aquifers (discharge lakes), or lose water over parts of the lake body and gain water over others (flow-through lakes; Born et al., 1979). This classification is suitable for regional groundwater flow systems, yet the superposition of shallow local flow systems between lake water and adjacent water table mounds or depressions complicates the interaction between these lakes and the groundwater system, because of subsurface heterogeneity and variations in flow rates within and among lakes (Schneider et al., 2005; Tóth, 1963; Winter, 1999). The phenomena of discharge lakes has received significant scientific attention (Anderson

et al., 2014; Attanayake and Waller, 1988; Belanger and Kirkner, 1994; Cherkauer and Zager, 1989), yet less attention has been paid to the recharge lakes. This review focuses on the phenomena of recharge lakes and describes factors that control the rapid flow between surface waters and groundwater, where the qualitative and quantitative evaluation of lake-aquifer interactions has been demonstrated by the present study on a decadal scale and over a large spatial domain.

The lake-groundwater interactions have traditionally been investigated by measuring water flux across the groundwater–surface water interface using seepage meters (Lee and Hynes, 1978; Murdoch and Kelly, 2003; Rosenberry et al., 2020), applying heat and environmental (e.g., radon-222) tracer methods (Becker et al., 2004; Shaw et al., 2013; Stonestrom and Constantz, 2003), or conducting numerical simulations of the water flow based on Darcy's Law (Kalbus et al., 2006; Kim and Sultan, 2002).

Alternatively, lake-groundwater interactions could be investigated using mass balance–based approaches, where the change in lake volume is estimated from the sum of precipitation and inflow (groundwater and surface water) in the lake, less evaporation and outflow from the lake (Gonfiantini, 1986). In these methods, one or more of these variables could be extracted from satellite data (e.g., precipitation from Tropical Rainfall Measuring Mission [TRMM]), land surface model outputs (evaporation from Global Land Evaporation Amsterdam Model [GLEAM]), or field measurements (surface water inflow and outflow from flow meter measurements; Abdelmohsen et al., 2019; Chipman and Lillesand, 2007; Crétaux et al., 2016; Gilbert, 1978; Kang and Hong, 2016; Martens et al., 2017). Hydrogeochemical (e.g., total dissolved solids) data have been used to investigate lake-groundwater interactions in the Pantanal wetland in Brazil (Freitas et al., 2019) and in the Nunavik in Canada (Cochand et al., 2020). Knowing the isotopic compositions of the lake and groundwater, isotopic mass balance calculations were also utilized in examining these interactions (e.g., Sparkling Lake in northern Wisconsin [Krabbenhoft et al., 1990], Lake Nasser in Egypt [Aly et al., 1993], and lakes in northern Finland [Ala-aho et al., 2015]).

These methods, although effective in many settings worldwide, have their limitations. Seepage meter measurements are subject to device and spatial sampling errors (Belanger and Montgomery, 1992), whereas heat tracer and Darcy's Law–based applications and mass balance approaches require extensive piezometer networks and/or intensive labor, conditions that are not necessarily available for many of the world's lakes (Nanteza et al., 2016; UNECA, 2011). Moreover, the above-mentioned methods limit exchange flux estimations to the scale of stream or lake sections (Smerdon et al., 2007; Virdi et al., 2012). This is not consistent with the nature of the groundwater–lake water exchange, which is highly variable in space and is significantly impacted by small-scale features, such as subsurface karsts (Lee et al., 2014), lithological heterogeneities (Ala-aho et al., 2015), and fault systems (Abdelmohsen et al., 2019). Additionally, the isotopic mass balance calculations assume that the composition of the groundwater outflow and surface water outflow resembles that of the lake water; hence, it requires that the lake is isotopically well mixed (Krabbenhoft et al., 1990), a condition that is not common in many lakes worldwide (Gat, 1995). The large and fast level changes in artificial lakes in response to lake regulation activities significantly influence the groundwater dynamics around the lake and put the estimation of the lake water–groundwater exchange flux largely out of reach using the traditional methods (El-Zehairy et al., 2018).

Additional complexities are introduced in estimating the lake water–groundwater exchange flux in settings where lakes are surrounded or floored by fractured or karstic bedrock aquifers. In such settings two different flow regimes exist: a fast flow regime (hundreds of km/yr) in fractures and/or caves (Abdelmohsen et al., 2019), and a slow flow regime (few m/yr) in rock pore spaces (Abotalib et al., 2019; Karay and Hajnal, 2015). The latter flow is laminar, can be characterized by Darcy's law, and its response to lake variations is can be estimated using standard experimental and/or numerical models (Karay and Hajnal, 2015). In contrast, the former flow is turbulent and cannot be described using Darcy's Law and standard modeling approaches. Instead, it has been characterized using a dual continuum approach or the so-called double porosity model (Karay and Hajnal, 2015; Petronici et al., 2019). However, this model's application has been limited given the lack of dense monitoring networks needed for adequate sampling of the fractures and karst

distribution, the difficulties associated with delineating these features in the subsurface, and the uncertainties in estimating the vertical and horizontal conductivities of these features (Petronici et al., 2019)

The Gravity Recovery and Climate Experiment (GRACE) was designed to map the temporal variations in the Earth's global gravity field and to estimate the variations in terrestrial water storage (TWS) on a monthly basis (Tapley et al. 2004). This data was successfully used to investigate the temporal variations in $GRACE_{TWS}$ over watersheds (Scanlon et al., 2012), aquifers, and lakes (Awange et al., 2009). However, less attention was paid towards the use of $GRACE_{TWS}$ data for understanding the interactions of various compartments largely due to the vertical resolution of GRACE data that does not allow differentiation between the contributions of various Components. One way around that was to use $GRACE_{TWS}$ together with outputs of land surface models to extract the temporal variations of compartments of interest such as groundwater (Mohamed et al., 2017; Sultan et al., 2019; Voss et al., 2013), soil moisture (Swenson et al., 2008), and surface water (Ramillien et al., 2011). This approach has proven to be effective in many areas of the world (Li et al., 2019; Thomas and Famiglietti, 2019), yet its overall accuracy depends on the accuracy of the model outputs (Ahmed and Abdelmohsen, 2018; Sultan et al., 2019; Tiwari et al., 2009). Very few studies were dedicated towards the use of $GRACE_{TWS}$ solutions to better understand the response of groundwater systems to seasonal cycles and to use $GRACE_{TWS}$ seasonal variation to better understand the hydrologic settings of the systems under consideration.

GRACE satellites monitor changes in terrestrial or land TWS as an anomaly relative to the long-term mean from changes in the Earth's gravity field but cannot be used to monitor absolute water storage (B. D. Tapley et al., 2004). The $GRACE_{TWS}$ signal includes both interannual and seasonal signals of water mass variations. The seasonal signals are the larger contributor to the overall $GRACE_{TWS}$ signal (40–80 %), whereas the interannual signals are much smaller (4–6%; Döll et al., 2014; Humphrey et al., 2016; Scanlon et al., 2019). Seasonal signals capture mass variations related to seasonal cycles (e.g., precipitation, snow, temperature, and evapotranspiration) and

anthropogenic activities (e.g., irrigation and groundwater extraction) that could be seasonal in nature as well (Scanlon et al., 2019). One would expect that the larger the observed variations in $GRACE_{TWS}$ signals, the easier it is to utilize such variations to better understand the hydrologic systems under investigation.

Using the seasonal change in $GRACE_{TWS}$ over Lake Nasser (4530 km^2) and the NSAS as our study areas, we investigate the nature of the seasonal interactions between surface water and groundwater, groundwater recharge from the lake into the aquifer, and directions and velocities of the groundwater flow that originated as infiltration from Lake Nasser. We also test and/or refine findings from earlier GRACE-related studies (Ahmed and Abdelmohsen, 2018; Abdelmohsen et al., 2019) over the NSAS in which the response of the NSAS to climatic variability (wet versus dry periods) was investigated. In our analysis of the seasonal change in $GRACE_{TWS}$ we use CSR-RL06M that reduces the leakage signal between the land and ocean signals (Save et al., 2016; Save, 2019) and we capture the dominant $GRACE_{TWS}$ signal, the seasonal signal. None of the previous studies examined the aquifer response to seasonal climatic variabilities.

4.2 Geology and Hydrology of the Dakhla Subbasin and Lake Nasser

The NSAS extends over 2×10^6 km^2 in Egypt, Libya, Chad, and Sudan. It is bound by the basement rocks from the east and the south (Sultan et al., 2013), the Devonian bedrock from the west, and the saltwater-freshwater interface from the north (Sultan et al., 2013). It is subdivided into three subbasins that are separated by basement uplifts: (1) the Uweinat-Aswan uplift separates the Dakhla subbasin in the north from the Northern Sudan Platform subbasin in the south, and (2) the Uweinat-Howar uplift separates the Northern Sudan Platform subbasin (east) from the Kufra subbasin (west) (Hesse et al., 1987; Fig. 11 inset).

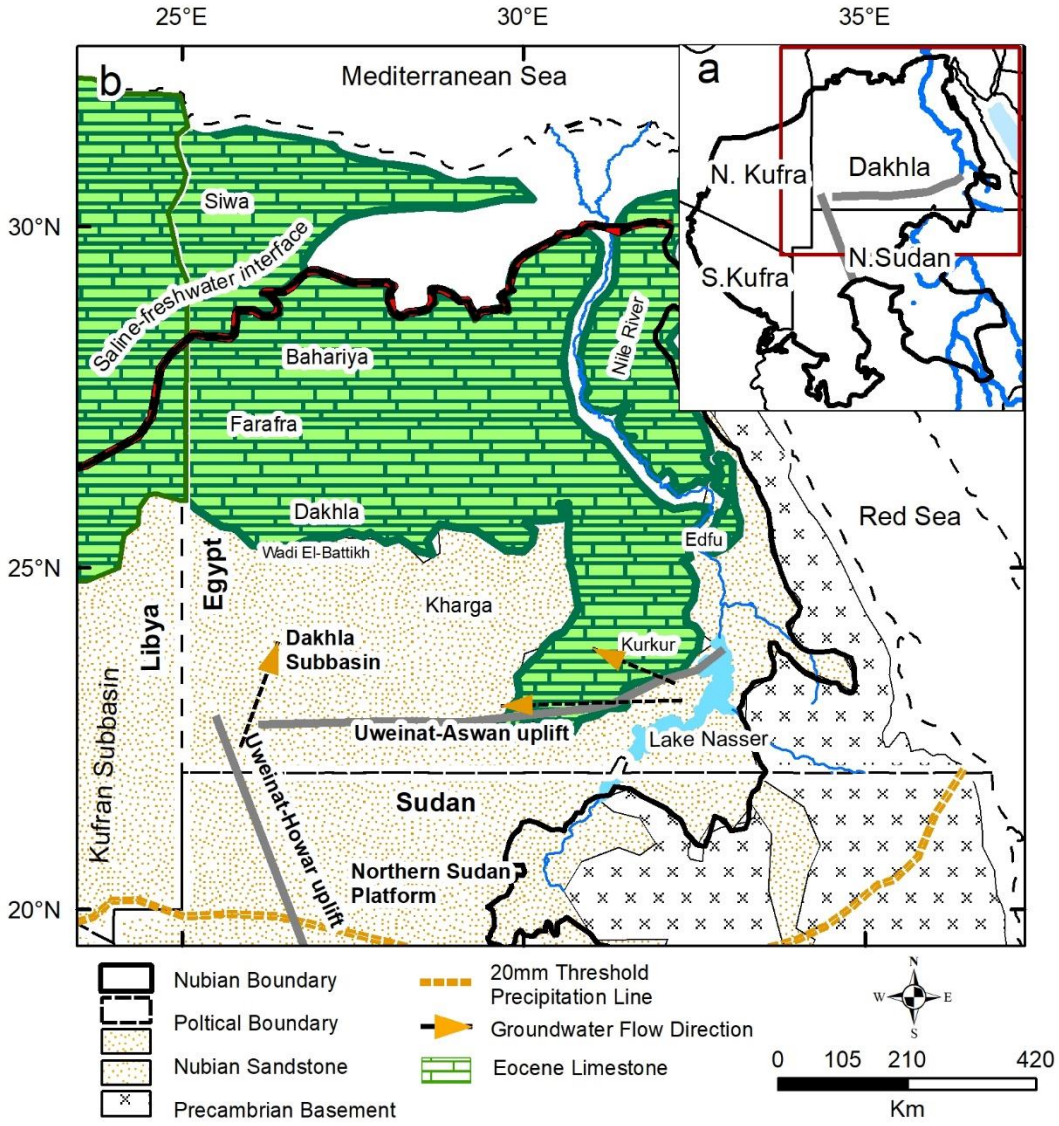

Figure 11. (a) Distribution of the NSAS in Libya, Sudan, and Chad, and basement uplifts (Uweinat-Aswan; Uweinat-Howar) separating its subbasins (Kufra, Northern Sudan platform, and Dakhla) within the aquifer. (b) Distribution of the Dakhla subbasin of the NSAS in Egypt, outcrops of the Upper Lower Cretaceous Nubian Sandstone and the overlying karstic Eocene limestone outcrops, and Lake Nasser, and the uplifts (Uweinat-Aswan; Uweinat-Howar) separating the NSAS subbasins (Kufra, Northern Sudan platform, and Dakhla) within the aquifer.

The NSAS is composed of: (1) continental sandstone formations of the Nubian Sandstone Aquifer, (2) marine carbonates of the post Nubian Aquifer System (Bakhbakhi, 2006; Thorweihe, 1990), and (3) confined shale and clay layers that separate the continental and marine sediments (Thorweihe and Heinl, 2002). The limestone outcrops in Dakhla subbasin are largely composed of Cretaceous chalk and Eocene limestone that are characterized by extensive karstic features (e.g., subsurface caves, speleothems, chalk pillars, and flowstones; Abdelmohsen et al., 2019; Abotalib et al., 2016; El Gammal, 2010; Halliday, 2003; Ruggieri, 2001; Waltham, 2001), many of which are found along fractures and joints (Aref et al., 1987; Butzer, 1965; Mostafa, 2013). The Dakhla subbasin is dissected by deep-seated and vertical basement faults which were reactivated by an earlier tectonic process (Neev et al., 1982; Sultan et al., 2007a). These include: (1) northwest-southeast faults (the extension of Najd fault system), (2) north-south faults, and (3) east-west Kalabsha and Seiyal faults (Abdelmohsen et al., 2019; Abotalib et al., 2016; Hermina, 1990; Khan et al., 2014; Neev, 1975; Neev et al., 1982; Thurmond et al., 2004). In the northern part of the Dakhla subbasin, the Nubian aquifer is confined beneath a thick layer of marine shales of Upper Cretaceous age, whereas unconfined conditions are present south of the Dakhla subbasin (Sturchio et al., 2004).

The NSAS is believed to have been largely recharged in previous wet climatic periods by intensification of monsoons (Prell and Kutzbach, 1987; Sarnthein et al., 1981; Yan and Petit-Maire, 1994) or paleowesterlies (Abotalib et al., 2019; Abouelmagd et al., 2014; Sturchio et al., 2004; Sultan et al., 1997), yet it is still receiving modern recharge locally over the Nubian Sandstone outcrops at the foothills of mountains that are receiving high (> 96 mm/yr) precipitation (Abdelmohsen et al., 2019). Examples of such areas include the Nuba and Darfur mountains (southern Sudan, North Sudan Platform), the Tibesti and Sherif mountains (eastern Chad, southern Kufra subbasin). Unlike the other two subbasins, precipitation over recharge areas in the Dakhla subbasin is negligible. Instead, the Dakhla subbasin receives its modern contributions from Lake Nasser, an extensive (length: 500 km; average width: 12 km; Kim and Sultan, 2002) artificial reservoir that developed upstream from the Aswan High Dam. It has a maximum capacity of 168 $\times 10^9$ m^3 at a maximum water level of 183 meters above mean sea level (m.a.m.s.l; Said, 1993). A

two-dimensional groundwater flow model covering the entirety of Lake Nasser in Egypt and Sudan and its surroundings was constructed and calibrated against observed head data in wells surrounding the lake (Sultan et al., 2013). Transient simulations suggest that the Dakhla subbasin is receiving significant recharge from Lake Nasser, where the total recharge for the period 1970–2002 was estimated at 100 km^3—about 60% of total lake capacity (Sultan et al., 2013). However, the net movement of the recharge front was found to be fairly slow (6–14 km) over the period 1970–2000 (Kim and Sultan, 2002). These estimates were extracted from a two-dimensional groundwater model constructed and calibrated against temporal head data over Lake Nasser and areas west of the lake.

4.3 Data and Methodology

The adopted methodology comprises four main steps. First, we investigated the spatial and temporal seasonal cycle–related variations in $GRACE_{TWS}$ over the Dakhla subbasin using seasonal difference in $GRACE_{TWS}$ (SD_{TWS}) images (refer to section 3.1.1; Fig. 12). Second, we conducted spatial and temporal correlation with annual precipitation to examine whether the observed seasonal cycle–related patterns could be related to the variations in precipitation patterns (distribution and intensity) from TRMM data (Fig. 13). Third, we examined whether the seasonal variations in the Lake Nasser surface water level (LNSWL; Fig. 14) and the associated leakage out signal from the lake could explain the observed seasonal cycle–related variations in $GRACE_{TWS}$. Knowing the temporal variations in LNSWL (from radar altimetry) and volume, we applied forward modeling to estimate the $GRACE_{TWS}$ and compared modeling results to the observed seasonal $GRACE_{TWS}$ variations (Figs. 15 and 16). Fourth, we examined whether the observed seasonal $GRACE_{TWS}$ variations could be related to rapid groundwater flow along preferred pathways in relation to variation in lake levels. This was accomplished by examining the amplitude and phase images (Figs. 17 and 18) and by correlating the observed seasonal $GRACE_{TWS}$ variations with the distribution of preferred pathways (faults, fractures, and karst topography; Fig. 19).

4.3.1 Processing of GRACE solutions

The processing of GRACE data in this study, included three recently released (RL06) GRACE solutions: CSR-RL06M, the mascon solutions from the Jet Propulsion Laboratory (JPL-RL06M), and the spherical harmonics solution (CSR- RL06SH (Save, 2019; Watkins et al., 2015; Wiese et al., 2016).The GRACE data acquired (January 2006 to January 2016) over the study area was used in this study. The CSR Rl06 was selected for generating various products: (1) SD_{TWS} images, (2) simulated leakage signal products, and (3) amplitude and phase images and the uncertainties reported in this study build on the variations (standard deviation) between values extracted from GRACE Spherical Harmonic (CSR RL06-SH) and mascons (CSR RL06-M and JPL RL06-M) solutions. The CSR RL06 was selected for generating various products: (1) SD_{TWS} images, (2) simulated leakage signal products, and (3) amplitude and phase images and the uncertainties reported in this study build on the variations (standard deviation) between values extracted from GRACE Spherical Harmonic (CSR RL06-SH) and mascons (CSR RL06-M and JPL RL06-M) solutions .

4.3.2 Seasonal difference $GRACE_{TWS}$ images

The SD_{TWS} images were generated from the seasonal fluctuation in $GRACE_{TWS}$ time series using equation 4, where $GRACE_{TWS}$ (sp) is the seasonal peak of $GRACE_{TWS}$ values for a particular year (annual maximum) and $GRACE_{TWS}$ (st) is the seasonal trough of $GRACE_{TWS}$ for the same year (annual minimum).

$$SD_{TWS} = GRACE_{TWS}\ (sp) - GRACE_{TWS}\ (st) \quad (4)$$

The smallest values over Lake Nasser and its surroundings were found to be in the months of July or August and highest in the month of November or December. Figure 12 shows the difference

images for the seasonal cycles in $GRACE_{TWS}$ over the Dakhla subbasin for the years 2006 through 2015.

4.3.3 Simulated leakage signal products.

We applied forward modeling to estimate the upper bound of leakage signal caused by concentrated mass in Lake Nasser and its extension into the Dakhla subbasin (Longuevergne et al., 2013). We selected to conduct this exercise in the spherical harmonics domain given the technical challenges posed by the extensive and irreversible processing steps if we were to work in the mascon domain given the presence of regularization constraints.(developed by CSR; Save et al., 2016, 2012). In the SH domain leakage error reduction and signal restoration can be applied as post processing steps. This is not the case for mascon solutions, where leakage error reduction can be applied only during the gravity inversion process through regularization or stabilization of the solution without any post processing including de-striping or any scaling (Save et al., 2012, 2016; Scanlon et al., 2016).

Two exercises were conducted. In the first the following steps were implemented. We identified the year in which the maximum SD_{TWS} was observed (year 2015; Figs. 12 and 5a; Step I) and tested whether the observed SD_{TWS} for this year could be accounted for by leakage signal alone from Lake Nasser. The temporal variations in Lake Nasser levels (from satellite altimetry data) for this year were extracted. We then generated a water level grid by filling the pixels (pixel size: 0.25° × 0.25°) over the lake by the maximum seasonal increase in lake level in 2015 and those outside the lake by zeros. A uniform mass variation was assumed across the entire lake to represent the concentration of true mass within the basin, and equation 5 was applied (Velicogna and Wahr, 2006; Longuevergne et al., 2013),

$$B(\theta, \lambda) = SD_{WL} \quad (5),$$

where, $B(\theta,\lambda)$ is the basin function, θ,λ are the latitude and longitude of the grid points, and the SD_{WL} is the seasonal difference in water level (Step II). We investigated the leakage-out signal effect of the lake due to finite spherical harmonic expansion by converting the generated water level grid into fully normalized spherical harmonics (or Stokes coefficients) up to degree/order (d/o) of 120; a 250 km Gaussian smoothing filter (Wahr et al., 1998; Step II) and the results are shown in Fig. 5b. The spherical harmonic analysis in Step II was applied to SD_{TWS} for year 2015; the results are shown in Fig. 15c (Step III). Finally, at each grid point, the differences between the observed SD_{TWS} in spherical harmonics (Fig. 15c) and the modeled leakage signal (Fig. 15b) were calculated (Fig. 15d; Step IV).

In the second exercise, we identified the year in which the maximum rise in LNSWL was observed (2008; Figs. 14 and 16a) and tested whether the observed SD_{TWS} for this year could be accounted for by leakage signal alone from Lake Nasser following the procedures described above for the first exercise (Steps I–IV). Hence, Fig. 15b gives us an upper bound estimate of the leakage out signal from the Lake Nasser.

An additional forward modelling approach was applied to investigate whether the observed SD_{TWS} across the Dakhla subbasin could have been caused by leakage in signal from sources outside of the Dakhla subbasin due to finite spherical harmonic expansion. In this approach we used simulated TWS derived from the Global Land Data Simulation System (GLDAS)(Landerer and Swenson, 2012; Rodell et al., 2020) (refer to Appendix B).

4.3.4 Amplitude, phase, and time series

Amplitude and phase of annual cycle images were generated from $GRACE_{TWS}$ for the entire investigated period (2003–2015), a period that witnessed a rise in lake levels (2012–2014), and

another that witnessed a decline in lake levels (2008–2010; Figs. 17 and 18). The amplitude image was generated to examine the spatial variations of the amplitude of $GRACE_{TWS}$ with respect to Lake Nasser in search of causal effects. On the phase images, the values of the pixels range from 1 to 12, where 1 represents the month of January and 12 the month of December, and the values assigned to each pixel represent the month in which $GRACE_{TWS}$ reaches its maximum value during the seasonal cycle. The $GRACE_{TWS}$ time series was extracted, then detrended for periods of lake decline and rise by removing the trend components after simultaneously fitting a trend and a seasonal term to each TWS time series over the selected locations (e.g., TWS1, TWS2, and TWS3; Fig. 17). These time series were compared to one another and to the time series for Lake Nasser levels to examine the spatial variations in lag time within an annual cycle for a better understanding of the factors (e.g., sources or structures) causing the observed spatial variations in $GRACE_{TWS}$ (Fig. 12).

4.3.5 Altimetry

The Lake Nasser surface levels time series (2003–2016) was derived from the US Department of Agriculture Foreign Agricultural Service (USDAFAS) global reservoir and lake monitoring database (GRLM; available at https://www.pecad.fas.usda.gov/cropexplorer/globalreservoir/), where lake height variations were extracted from satellite altimetry data sets (TOPEX/Poseidon/Jason satellite series: 10-day resolution). The Lake Nasser monthly variations were converted to lake level height with respect to the mean sea level (m.a.m.s.l). Variations in interannual lake level trends (rising versus declining) were identified from the lake level time series using the regime shift detection (RSD) method (Andersen et al., 2009; Reeves et al., 2007; Rodionov, 2004; Villarini et al., 2009).

4.3.6 Precipitation (TRMM)

The average monthly precipitation (2006–2015) over the NSAS extracted from TRMM Multi-satellite Precipitation Analysis (TMPA; Huffman et al., 2007; Kummerow et al., 1998). The TMPA was designed to combine all available precipitation datasets from different satellite sensors and monthly surface rain gauge data to provide a "best" estimate of precipitation at a spatial resolution of 0.25° × 0.25° for the areas between 50°N and 50°S. TRMM 3B43, which provides monthly data, is used in this study. The data are available at https://pmm.nasa.gov/data-access/downloads/trmm.

4.4 Results and Discussion

Inspection of Fig. 12 shows the spatial distribution of the seasonal increase in $GRACE_{TWS}$, here expressed as SD_{TWS}, over the Dakhla subbasin throughout the period 2006 to 2015. The seasonal variations in $GRACE_{TWS}$ for each of the investigated years do not correlate with precipitation patterns over the Dakhla subbasin for that year (Figs. 12 and 13). This observation, together with the fact that precipitation is negligible over the Dakhla subbasin (0–5 mm/month; 2016 to 2015: average annual precipitation, 8.5 mm/yr; Fig. 13) over the Dakhla subbasin rules out precipitation as the source of the observed seasonal variation in $GRACE_{TWS}$ over the Dakhla subbasin. That is not the case in areas to the north of the Dakhla subbasin (Mediterranean coastline) and to its east and northeast (Red Sea Hills and Sinai). A spatial correlation has been observed between SD_{TWS} Signal (Fig. 12) and northerly precipitation patterns (Fig. 13).

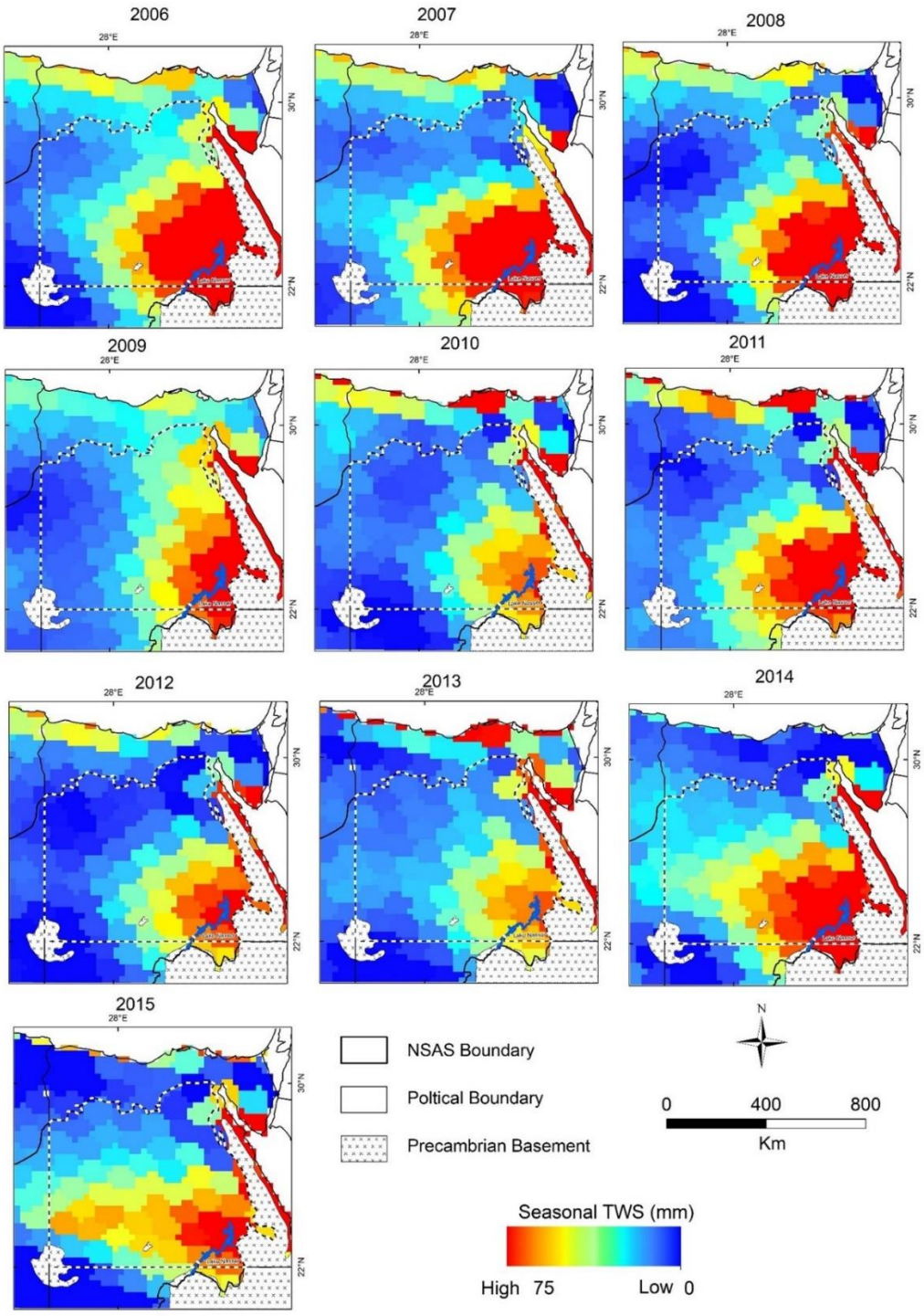

Figure 12. SD_{TWS} image over the Dakhla subbasin for 2006 through 2015 showing consistent patterns of increasing $GRACE_{TWS}$ centered over Lake Nasser and extending hundreds of kms away from the lake. The white line shows the distribution of the Dakhla subbasin.

For each of the investigated years we observe that the SD_{TWS} is centered over Lake Nasser and decreases in magnitude away from the lake (Fig. 12). The observed SD_{TWS} covers large areas ranging from 172,500 km^2 (2010) to 385,700 km^2 (2015) with SD_{TWS} > 25 ±9mm, reaching distances as far as 700 km from Lake Nasser (2014/2015), and amounting to a total seasonal increase in $GRACE_{TWS}$ over the Dakhla subbasin that ranges from 7.7 km^3 (2010) to 18 km^3 (2015). Leakage in signal simulations for years 2015 and 2008 show that the "leakage in" is minimal to negligible over the Dakhla subbasin. It is restricted to an east-west trending zone, 200 km deep zone along its northern peripheries (up to 10 mm in 2015 and 13 mm in 2008) and is negligible (< 4 mm) over the rest of the subbasin (see Appendix B). The leakage signal is related to precipitation over the Mediterranean coastline. These collective observations rule out that the observed seasonal SD_{TWS} variations are caused by sources outside of the subbasin and are consistent with the Lake being the main source of the observed SD_{TWS} seasonal patterns and recharge of the Dakhla subbasin.

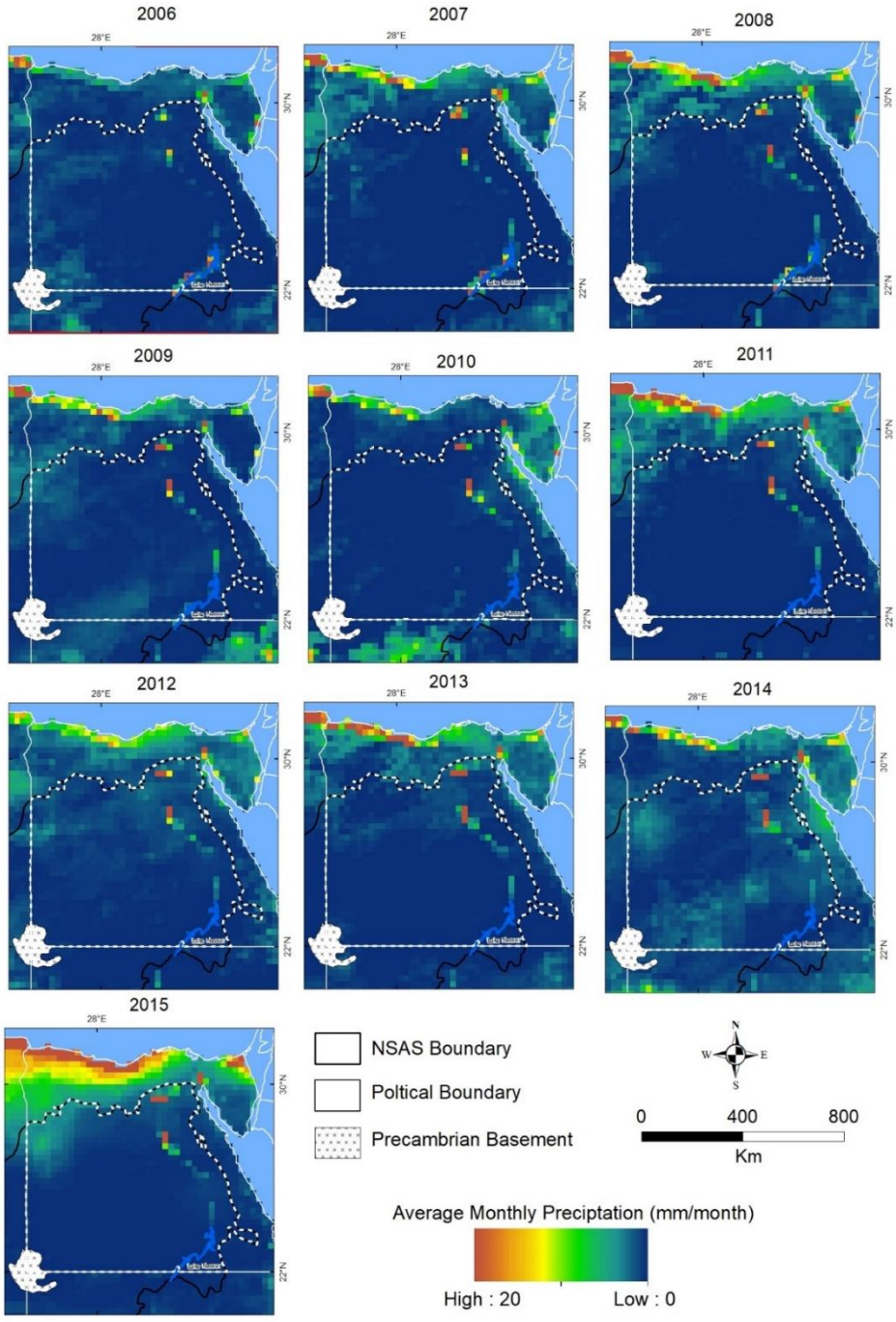

Figure 13. Average monthly precipitation over the Dakhla subbasin for 2006 through 2015. Comparison of Figs. 2 and 3 shows that precipitation is not responsible for the observed seasonal variations in GRACETWS. The white dashed line shows the distribution of the Dakhla subbasin.

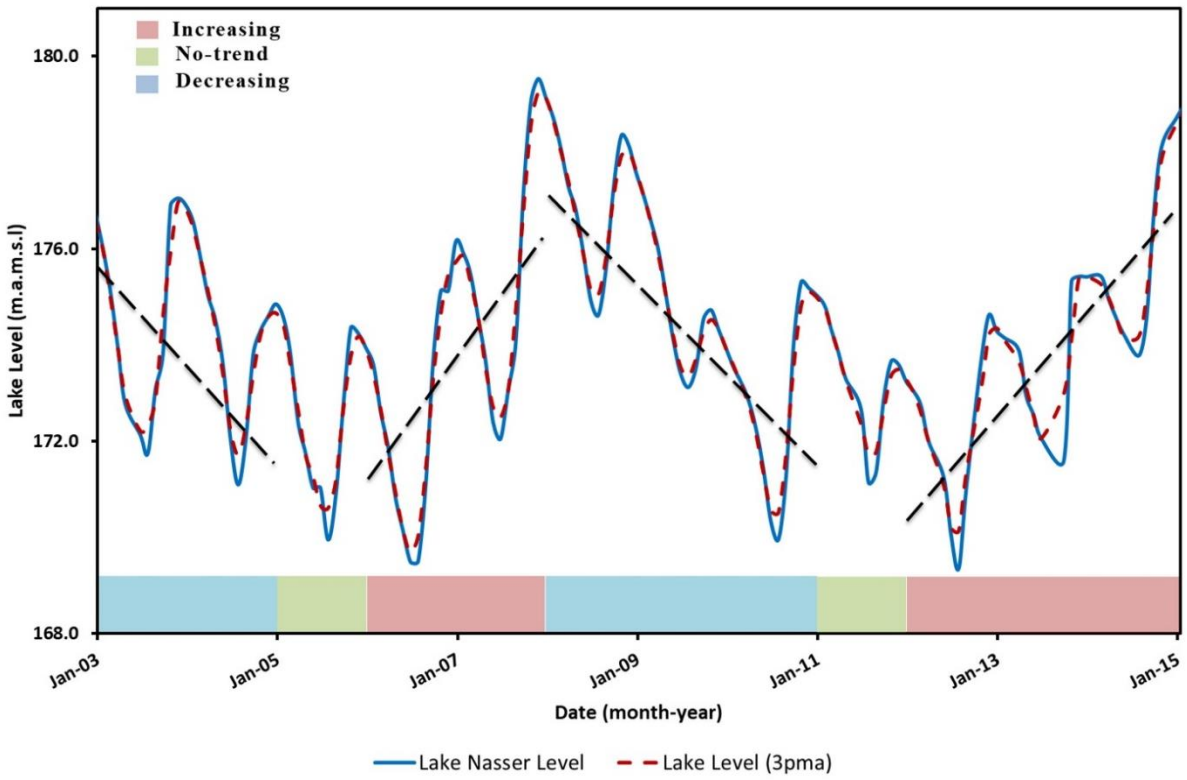

Figure 14. Time series for Lake Nasser surface water level (2003–2015) extracted from the GRLM database.

The signal of surface water storage (e.g., Lake Nasser) may leak to the surrounding areas (leakage out signal), and the signal from the surrounding areas may also leak into the surface water (leakage in signal; Swenson and Wahr, 2007, 2002; Wahr et al., 1998). We investigated whether the leakage out from Lake Nasser could be the cause of the observed variations in SD_{TWs} over the Dakhla subbasin. The maximum observed SD_{TWS} was in 2015 (Figs. 12 and 15a), in which the SD_{TWS} signal centered over the Lake Nasser extended for hundreds of kilometers away from the lake (Fig.

15a: area outlined by orange contour; SD_{TWS} > 25 ±9 mm), reaching distances of up to 700 km from the lake. The simulated spherical harmonic leakage-out signal effect from LNSWL for 2015 (Fig. 15b) is modest. In areas in the immediate surroundings (Fig. 5b; 0–250 km; the area outlined by red contour line) of the lake, the SD_{TWS} is moderate (≥10 mm and < 49 mm), negligible (< 10 mm) in areas 250 to 330 km from the lake (Fig. 15b; area subtended by the red and white contours), and nonexistent beyond 330 km from the lake. In contrast, the simulated SD_{TWS} (spherical harmonic representation of the mascon solutions) extends over much larger areas in the Dakhla subbasin. For example, the SD_{TWS} threshold line (Fig. 5c; >30±10 mm orange contour) extends as far as 700 km to the west (Fig. 15c). Not only is the extension of the simulated (spherical harmonic) SD_{TWS} much larger than the simulated spherical harmonic leakage out signal , but its magnitude is larger as well. A difference image (Fig. 15d) between the observed SD_{TWS} (Fig. 15c) and the modeled leakage out signal both in spherical harmonics (Fig. 15b) shows that the former exceeds the latter by 13.7 km^3 in the Dakhla subbasin.

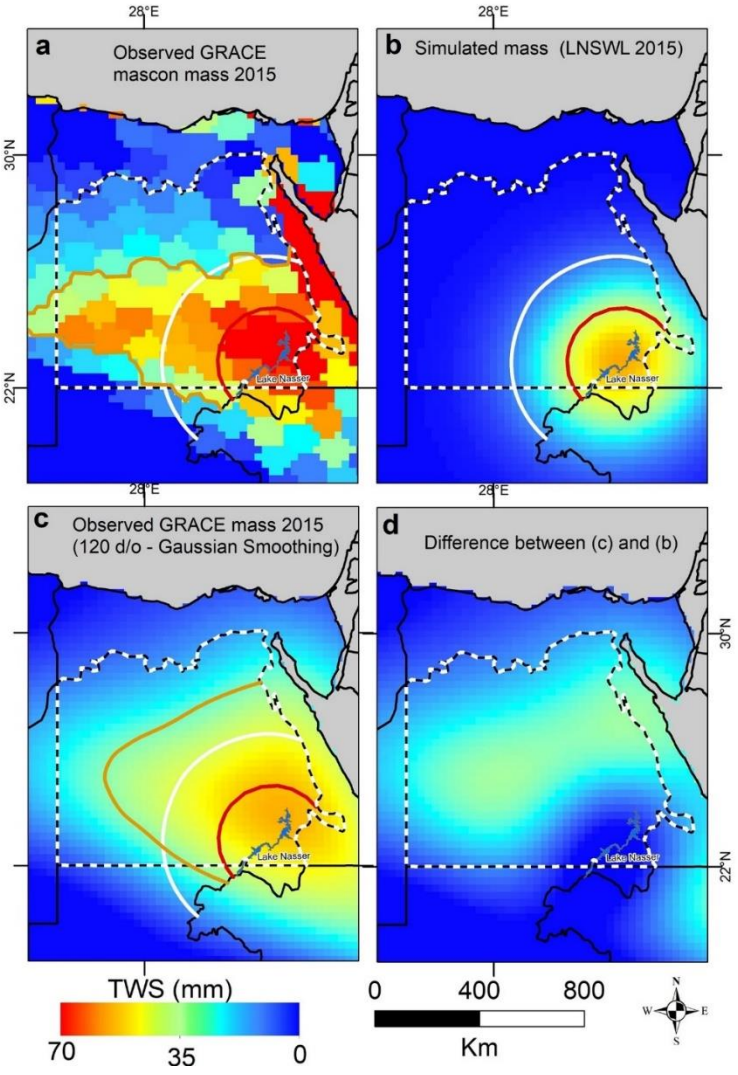

Figure 15. Forward modeling of the seasonal mass variations in the year in which the maximum SD_{TWS} was observed (2015) to test whether the observed SD_{TWS} for this year could be accounted for by leakage signal alone from Lake Nasser. (a) SD_{TWS} image over the Dakhla subbasin for 2015 (Step I). (b) Leakage-out signal effect image of the lake due to finite spherical harmonics expansion obtained by converting the generated water level grid into fully normalized spherical harmonics (or Stokes coefficients) up to degree/order (d/o) of 120; a 250 km Gaussian smoothing filter (Wahr et al., 1998; Step II). (c) The spherical harmonics analysis in Step II applied to SD_{TWS} for 2015 (Step III). (d) Difference image between the simulated SD_{TWS} (Fig. 15c) and the modeled leakage signal (Fig. 5b; Step IV). The areas outlined by the orange contours (Figs 5a,

5c) have, SDTWS values of > 25 mm. For comparison purposes the simulated leakage out signal from LNSWL outlined by red and white contour lines (red: < 49 mm; white < 10 mm; Fig. 5b) are plotted on Figs. 5a and 5c.

An additional, yet similar, investigation was conducted to test whether the leakage out signal from Lake Nasser could be the cause of the observed variations in SD_{TWs} over the Dakhla subbasin. In this case, the year in which the maximum rise in LNSWL was selected instead of maximum SD_{TWS} year. The maximum rise (7.5 m) was in year 2008 (Fig. 14). Using procedures described above, we note observations similar to those reported above: (1) a SD_{TWS} signal centered over the Lake Nasser extends for hundreds of km (Fig. 16a: area outlined by the SD_{TWS} threshold orange contour line of >15 mm) away from the lake, (2) a modest leakage out signal simulated effect from LNSWL (Fig. 16b; 0–270 km: ≥ 10 mm and <72 mm; 270–350 km: <10 mm; >350 km: none), (3) extension of the simulated SD_{TWS} over large areas (Fig. 16c; area outlined by the threshold >20 mm orange contour line) as far as 600 km to the west (Fig. 16c), and (4) the simulated SD_{TWS} exceeds the simulated leakage out signal by 10.5 km^3 in the Dakhla subbasin (Fig. 16d).

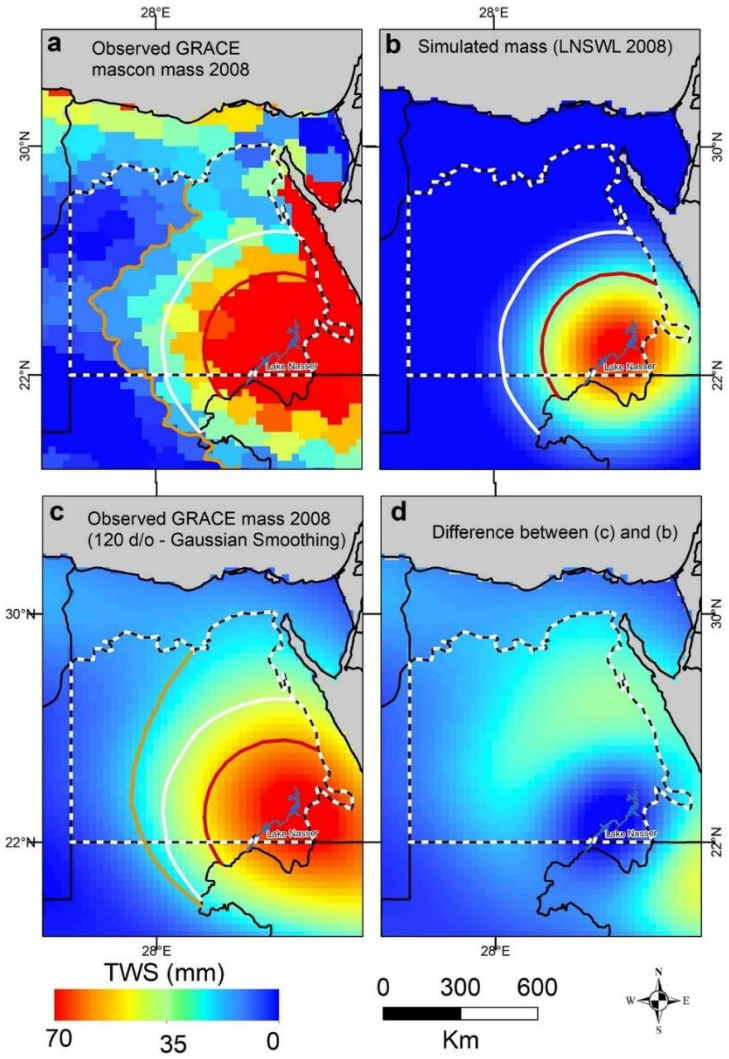

Figure 16. Forward modeling of the seasonal mass variations in the year in which the maximum rise in LNSWL was observed (2008) to test whether the observed SD_{TWS} for this year could be accounted for by leakage alone from Lake Nasser. (a) SD_{TWS} image over the Dakhla subbasin for 2018 (Step I). (b) Leakage-out signal effect image of the Lake due to finite spherical harmonics expansion obtained by converting the generated water level grid into fully normalized spherical harmonics (or Stokes coefficients) up to degree/order (d/o) of 120; a 250 km Gaussian smoothing filter (Step II). (c) The SH analysis in Step II applied to SD_{TWS} for year 2008 (Step III). (d) Difference image between the observed SD_{TWS} (Fig. 5c) and the modeled leakage signal (Fig. 5b) both in spherical harmonics (Step IV). The areas outlined by the orange Figs 6a, 6c) have SDTWS values of > 15 mm. For comparison purposes the simulated leakage out signal from

LNSWL outlined by red and white contour lines (red: < 72 mm; white < 10 mm; Fig. 6b) are plotted on Figs. 6a and 6c.

We have shown that the observed SD_{TWs} exceeds the estimated leakage signal. Even with adopting spherical harmonics solutions that tend to emphasize leakage signal from the lake spatially and attenuate the GRACE signal (Bridget R. Scanlon et al., 2016), we could not account for the observed variations in the SD_{TWS} signal. Hence, another mechanism has to be involved. We hypothesize that in addition to the artificial numeric leakage signal effect, infiltration and rapid groundwater flow from Lake Nasser has to be invoked to explain the observed spatial and temporal variations in SD_{TWS}.

Additional support for this hypothesis comes from seasonal spatial and temporal relationships between lake levels and $GRACE_{TWS}$ solutions within the Dakhla subbasin. If Lake Nasser is the main source of recharge for the Dakhla subbasin, the peak seasonal $GRACE_{TWS}$ (SD_{TWS}) in the Dakhla subbasin should occur over the lake and its surrounding at the time the lake levels peak. The runoff from the Blue Nile, which represents more than 80% of the surface waters reaching Lake Nasser, is impounded behind the High Dam and reaches peak levels in the months of December or January (Kim and Sultan, 2002; Said, 1993; Sultan et al., 2013). For all of the investigated years, the highest SD_{TWS} in the Dakhla subbasin occurs over Lake Nasser and its surroundings during the months of December and January (Fig. 14). One would also expect to observe higher seasonal increase in SD_{TWS} during lake cycles where lake levels are on the rise, and vice versa during cycles where lake levels are on the decline. Using radar altimetry data, four periods were identified: (1) 2003 to 2005: decline in LNSWL, (2) 2006 to 2007: increase in LNSWL, (3) 2008 to 2010: decline in LNSWL, and (4) 2012 to 2014 increase in LNSWL (Fig. 14). Inspection of Fig. 12 indicates that in years 2014 and 2015 (end of LNSWL rise cycles) the SD_{TWS} reached maximum distances from Lake Nasser and in years 2010 and 2011 SD_{TWS} (end of LNSWL decline cycles) were at minimum distances from Lake Nasser (Fig. 12).

Moreover, if Lake Nasser is the main source of recharge for the Dakhla subbasin, one would also expect to observe a progressive shift in phase and decrease in amplitude with distance from the lake. Inspection of Figs. 17 and 18 show that this is indeed the case. In Figs. 17 and 18 three periods were examined: the entire investigated period (2003–2015), a period that witnessed a decline in lake levels (2008–2010; Fig. 17b), and another period that witnessed a rise in lake levels (2012–2014; Fig. 17c). Inspection of Fig. 17 shows that for all investigated periods the spatial distribution of amplitude is high over the Lake Nasser and progressively declines with increasing distance from it. For example, for the period 2003–2015, the average amplitude close to Lake Nasser (<50 km) is 70 ±18 mm, 13 ±4 mm at a distance of 450 km from the lake, and declines to 10 ±4 mm some 600 km from the lake.

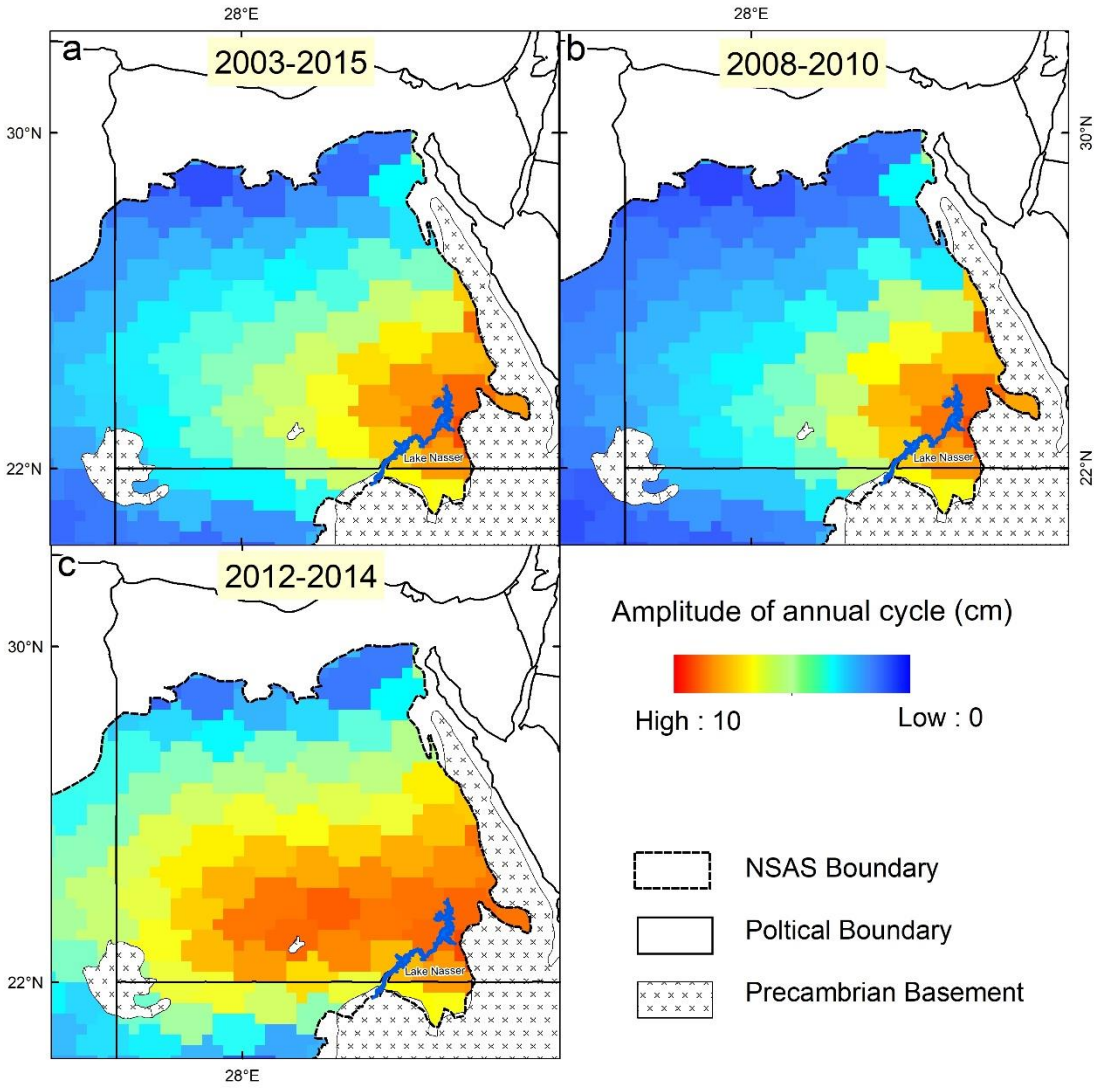

Figure 17: Amplitude of annual cycle derived from monthly $GRACE_{TWS}$ solutions for (a) the entire investigated period (2003–2015), (b) a period that witnessed a decline in lake levels (2008–2010), and (c) a period that witnessed a rise in lake levels (2012–2014). In all three periods a progressive decrease in amplitude with distance from the lake was observed.

Starting with the months of December and January, which mark peak lake levels, we observe phase shifts with increasing distance from the lake. The phase shift is observed throughout the entire investigated period (2003–2014; Fig. 18a), a period witnessing a decrease in lake levels (2008–2010; Fig., 18b), and a period witnessing an increase in lake levels (2012 to 2015; Fig. 18c). The above-mentioned observations suggest that Lake Nasser is not only the main source of recharge, but is also a continuous source of recharge during high and low flood periods.

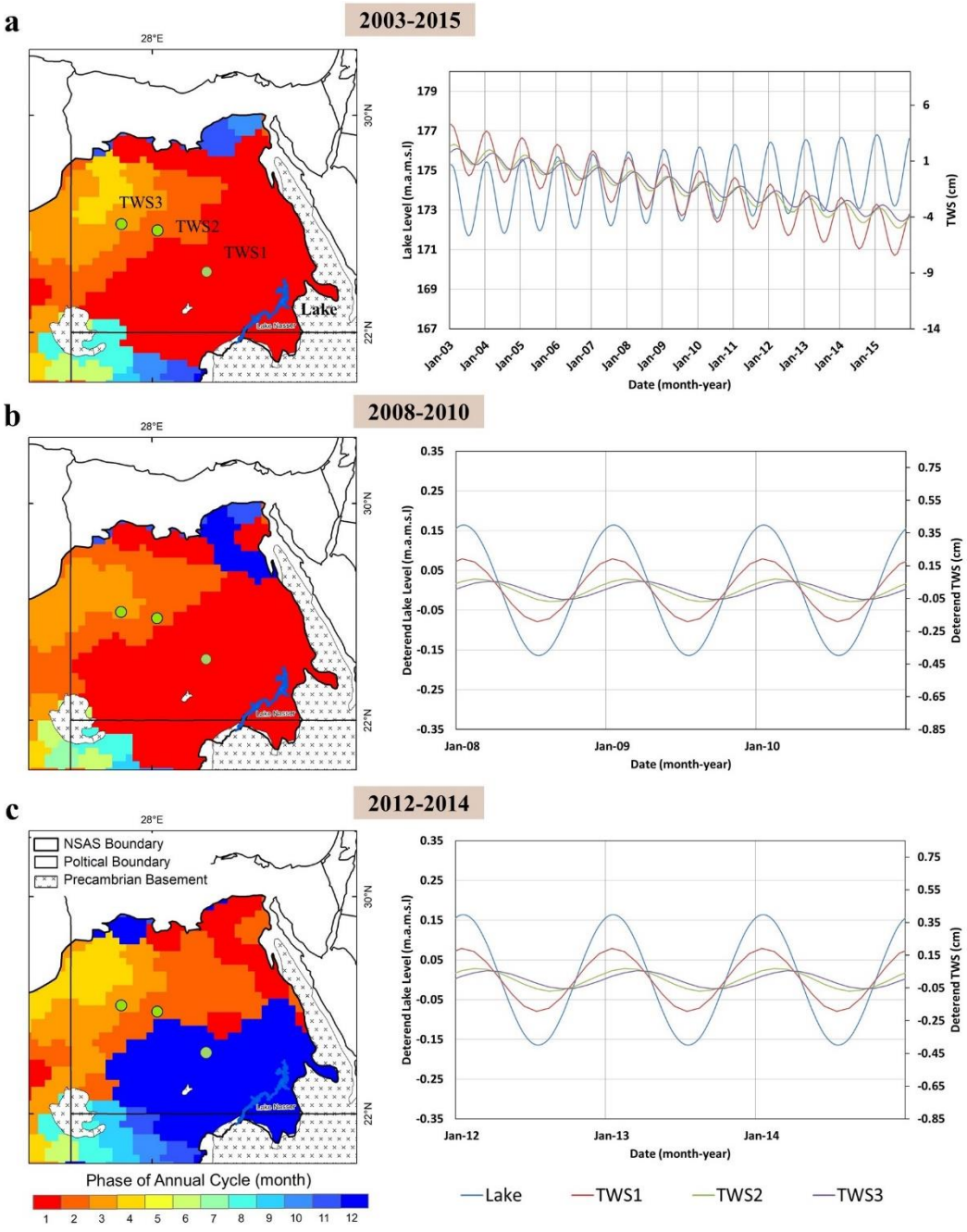

Figure 18. The phase of the annual cycle derived from $GRACE_{TWS}$ for (a) the entire investigated period (2003–2015), (b) a period that witnessed a decline in lake levels (2008–2010), and (c) another that witnessed a rise in lake levels (2012–2014). In all three periods a progressive shift in phase with distance from the lake is observed. Also shown for each of the three periods are

comparisons between the $GRACE_{TWS}$ time series at variable distances from Lake Nasser. A lag time of up to three months is observed between $GRACE_{TWS}$ and lake water level.

In our earlier study (Abdelmohsen et al., 2019) we proposed the presence of preferred pathways for rapid groundwater flow along a network of karst and faults in the Dakhla subbasin and provided field and isotopic evidences in support of this model. In this article, we show that the propagation of the seasonal cycles, especially those within rising lake level cycles (e.g., 2014 and 2015) follow the distribution of east-west trending faults and shear systems and the distribution of karstic carbonate sequences (Fig. 19).

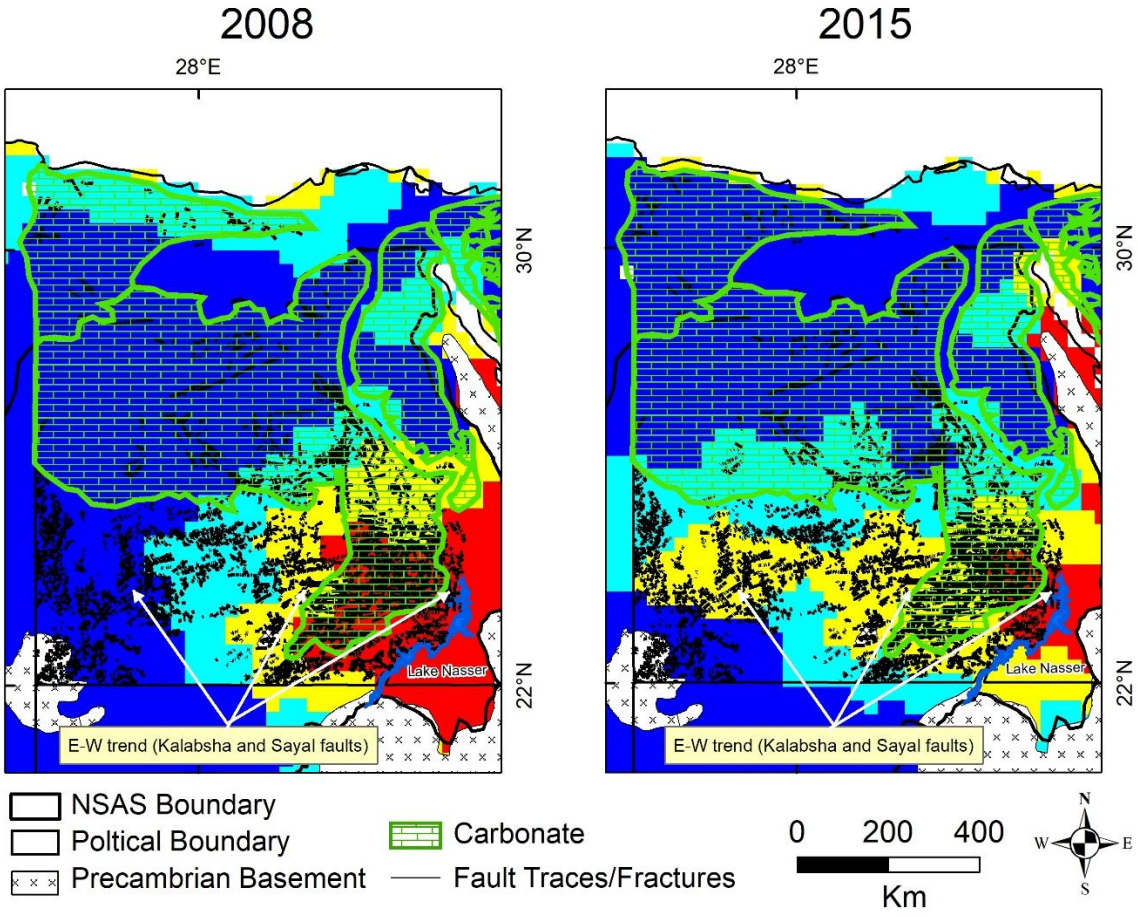

Figure 19: Comparison of the distribution of areas witnessing seasonal increase in $GRACE_{TWS}$ with the distribution of faults/karst (Abdelmohsen et al., 2019; Abotalib et al., 2016; Hermina, 1990; Khan et al., 2014; Neev, 1975; Neev et al., 1982; Thurmond et al., 2004). The figure shows a preferential increase in $GRACE_{TWS}$ along the E-W trending Kalabsha and Sayal fault system and their postulated extension to the west.

Our findings are consistent with earlier models (Kim and Sultan, 2002) that acknowledged the role of the Aswan High Dam in altering the pre–High Dam surface and groundwater interactions. Prior to the dam construction, the Dakhla subbasin discharged in the Nile, but following the construction of the Aswan High Dam, surface water level were elevated by as much as 65 m and the surface water recharged the Dakhla subbasin (Kim and Sultan, 2002). However, these models estimated the movement of the recharge front by as much as few meters a year, whereas our GRACE findings call on groundwater flow by as much as hundreds of km per year. These two models are not mutually exclusive. We acknowledge that groundwater flow is very slow through the porous media under laminar Darcian flow. One way to achieve the observed rapid mass movement is for groundwater flow to occur under non-Darcian flow system within high transmissivity media of fractured and karstic texture.

Several studies have reported extremely high groundwater flow velocities using tracer experiments in fissured and karstic aquifers. Groundwater flow velocities greater than 2 km/day were observed in fractured and chalk aquifers in the Hampshire Basin, south Hampshire (Atkinson & Smith, 1974). Similar high groundwater flow velocities (5.8–6.8 km/day) were measured in karstic chalk aquifers in Dingley, Berkshire, in southern England (Banks et al., 1995). These observed rapid groundwater flow velocities were observed in aquifers characterized by (1) high hydraulic gradient, and (2) highly fractured systems (faults/shear zones) and karstic textures. Such characters can be seen here, where the hydraulic gradient of Lake Nasser is as high as 0.0014 (Alfaran, 2013) and extensive networks of interconnected structures and karstic topography (Abdelmohsen et al.,

2019). One of these structures is the strike slip, E-W trending Kalabsha and Sayal fault system (Hussein et al., 2013; Saleh et al., 2018).

The seepage of Lake Nasser water into these fault systems and their associated fracture zones increases the confined hydro-dynamic pressures and flows along these faults, which in turn increases the lubrication and reactivation of these faults (Kebeasy et al., 1987; Kumar et al, 2012; Hussein et al., 2013). Another driving force for the reactivation of this system could be the differential rifting rates in the northern Red Sea (Woodword-Clyde Consultants, 1985; Hussein et al., 2013).The ongoing reactivation of this fault system has apparently increased the permeability of the fault zones by as much as several orders of magnitude (Gudmundsson, 2000). Such hydrogeological and geological settings provide preferred and rapid pathways for groundwater flow from Lake Nasser (the recharge area) to the Dakhla subbasin along the E-W trending Kalabsha and Sayal fault system. Figure 19 shows a preferential increase in $GRACE_{TWS}$ (propagation of mass) along the E-W trending Kalabsha and Sayal fault system and their postulated extension to the west (Fig. 19).

A new conceptual model for the groundwater recharge and flow in the Dakhla subbasin of the NSAS is proposed based on findings presented in this study. Two flow mechanisms are proposed: a slow groundwater flow throughout the porous matrix in the subbasin and across the entire NSAS, and a fast flow developed and hosted within the highly fractured zones (faults/shear zones/karst topography), which forms a fractured channel network across the porous matrix. The slow groundwater flow through porous matrix is expected in a range of 0.001–0.01 m/day (Darcy velocity) based on a flow model calibrated against water levels from a monitoring well network near Lake Nasser (Sultan et al., 2013). The fast flow through the fractured channel network range from 5.0–6.7 km/day based on the range of distance 600–700 km from the lake where SD_{TWS} exceeds threshold (20 ±9 mm) (Figs 15d and 16d) and phase changes over three to four months (December to March). Future studies should be designed to explore the fracture system in more detail within the NSAS.

Although the suggested conceptual model with two flow mechanisms in the NSAS presents challenges in simulations of both flows in groundwater for this area, it could offer an opportunity to improve our flow predictions and could support future management of groundwater resources. The findings from this study provide a possibility to develop groundwater flow models that incorporate both flow mechanisms. The GRACE data processed in the study is a useful dataset to help constrain and calibrate such models.

The extensive turbulent flow through fractures and caverns and the high hydraulic pressures especially during high lake stands introduce significant challenges to modeling lake-aquifer interactions, even when double continuum or triple porosity (matrix, fracture and conduit) models (Ford, 2014) are applied. The suggested approach can potentially assist in understanding lake-aquifer interactions, especially in artificial reservoirs surrounded by karstified or fractured bedrocks. Examples include the Bratsk lake in Russia (169 Km^3; Eraso et al., 1995), Volta lake in Ghana (150 Km^3; Yidana et al., 2019) and Mosul dam lake in Iraq (11.1 Km^3; Sissakian et al., 2018). All of these reservoirs show evidence of massive turbulent flow and significant interaction with the surrounding aquifers that should be adequately quantified. The aquifer surrounding Lake Volta is largely composed of impervious sedimentary successions. It is characterized by low primary porosity and very high fracture-related secondary porosity (Achcampong and Hess, 1998; Yidana et al., 2007) and by highly variable transmissivity (0.3 to 267 m^2/day; Dapaah-Siakwan and Gyau-Boakye, 2000). The dense fracturing of the bedrock surroundings Lake Volta can probably explain its anomalous seasonal variations in the $GRACE_{TWS}$ values which are three times those of Lake Victoria, a natural lake with a surface area eight times that of Lake Volta (Moore and Williams, 2014). We suggest that applications similar to those described in this manuscript could complement the conventional methods in understanding the complex lake-aquifer interactions in karst/fractured settings that could have contributed to the significant damage or failure of dams(Milanović, 2014). Examples include the failure of the St. Francis Dam in California (Begnudelli and Sanders, 2007) and San Juan earth Dam in Spain (Gutiérrez et al., 2003).

4.5 Conclusion

We investigated the interactions between Lake Nasser and the underlying Nubian Sandstone Aquifer System (NSAS) in the Western Desert of Egypt (area: 0.66×10^6 km^2) by examining and correlating, temporally and spatially, the variations in $GRACE_{TWS}$ solutions (CSR-Rl06M), with precipitation (from TRMM), and lake levels (from radar altimetry), area (from temporal Landsat imagery), and water volume. The spatial and temporal observations from the above-mentioned datasets, together with modeling results of the leakage patterns of Lake Nasser's geophysical signal, suggest that the lake is the main source of modern recharge for the Dakhla subbasin. The observations and modeling support a new conceptual model for the NSAS, which has a slow groundwater flow through predominated porous matrix and a rapid groundwater flow along a network of faults, fractures, and karst topography across the matrix.

The findings from this study could potentially complement existing methods (such as groundwater flow models or geochemical and isotopic tracers) in understanding the nature, and the full scale, of the interactions between lakes and aquifers. Our methods provide an opportunity to detect rapid groundwater flow along preferred pathways in large scale aquifers, but not the slow flow in the surrounding porous media, whereas the traditional methods are more suited for the latter. The advocated method has its limitations as well: the large footprint of the GRACE data limits its application to large aquifers. We have shown that using the seasonal $GRACE_{TWS}$ difference images we could map the approximate distribution of the areas affected by the rapid groundwater flow, however delineating these areas and mapping the distribution of the preferred pathways with precision is hampered by the large footprint of the GRACE data and the leakage signal from one pixel to its neighbors. The temporal acquisition of GRACE data (monthly) is another technical impediment of capturing the short term signals. Moreover, the technique is more suited for arid and hyper-arid areas, but less so for temperate areas. In the former, precipitation is negligible and thus seasonal variations in $GRACE_{TWS}$ could be attributed with confidence to variations in groundwater storage. In contrast, in temperate areas $GRACE_{TWS}$ variations could be overshadowed

with precipitation-related variations in soil moisture and/or surface water storage and therefore be more difficult to estimate.

The advocated method provides cost-effective, robust, and innovative approaches to examine the lake-aquifer interaction from readily available datasets and could be especially useful in data-scarce locations in the arid world. We suggest that the proposed conceptual model for the interaction between Lake Nasser and the Dakhla subbasin could be applicable to aquifers of similar geologic, climatic, and hydrologic settings worldwide and that the approaches similar to those advocated here could be used to investigate the validity of this suggestion, improve flow predictions, and ultimately optimize management of groundwater resources.

CHAPTER 5

SUMMARY

A detailed description of all of the major conclusions of this work, the reader is referred to Chapter 3 Section 3.3 and Chapter 4 Section 4.5, where all of the conclusions of this thesis were discussed at length.

REFERENCES

Abdelmohsen, K., Sultan, M., Ahmed, M., Save, H., Elkaliouby, B., Emil, M., Yan, E., Abotalib, A.Z., Krishnamurthy, R.V., Abdelmalik, K., 2019. Response of deep aquifers to climate variability. Sci. Total Environ. 677, 530–544. https://doi.org/10.1016/j.scitotenv.2019.04.316

A, G., Wahr, J., Zhong, S., 2013. Computations of the viscoelastic response of a 3-D compressible Earth to surface loading: an application to Glacial Isostatic Adjustment in Antarctica and Canada. Geophys. J. Int. 192, 557–572. https://doi.org/10.1093/gji/ggs030

Abotalib, A.Z., Sultan, M., Elkadiri, R., 2016. Groundwater processes in Saharan Africa: Implications for landscape evolution in arid environments. Earth-Science Rev. https://doi.org/10.1016/j.earscirev.2016.03.004

Abotalib, A.Z., Sultan, M., Jimenez, G., Crossey, L., Karlstrom, K., Forman, S., Krishnamurthy, R.V., Elkadiri, R., Polyak, V., 2019. Complexity of Saharan paleoclimate reconstruction and implications for modern human migration. Earth Planet. Sci. Lett. 508, 74–84. https://doi.org/10.1016/J.EPSL.2018.12.015

Abouelmagd, A., Sultan, M., Sturchio, N.C., Soliman, F., Rashed, M., Ahmed, M., Kehew, A.E., Milewski, A., Chouinard, K., 2014. Paleoclimate record in the Nubian Sandstone Aquifer, Sinai Peninsula, Egypt. https://doi.org/10.1016/j.yqres.2013.10.017

Achcampong, S.Y., Hess, J.W., 1998. Hydrogeologic and hydrochemical framework of the shallow groundwater system in the southern Voltaian Sedimentary Basin, Ghana. Hydrogeol. J. 6, 527–537. https://doi.org/10.1007/s100400050173

Ahmed, M., Abdelmohsen, K., 2018. Quantifying modern recharge and depletion rates of the Nubian Aquifer in Egypt. Surv. Geophys. 39, 729–751. https://doi.org/10.1007/s10712-018-9465-3

Ahmed, M., Sultan, M., Wahr, J., Yan, E., 2014. The use of GRACE data to monitor natural and

anthropogenic induced variations in water availability across Africa. Earth-Science Rev. https://doi.org/10.1016/j.earscirev.2014.05.009

Ahmed, M., Sultan, M., Yan, E., Wahr, J., 2016. Assessing and improving land surface model outputs over africa using GRACE, field, and remote sensing data. Surv. Geophys. 37, 529–556. https://doi.org/10.1007/s10712-016-9360-8

Ala-aho, P., Rossi, P.M., Isokangas, E., Kløve, B., 2015. Fully integrated surface-subsurface flow modelling of groundwater-lake interaction in an esker aquifer: Model verification with stable isotopes and airborne thermal imaging. J. Hydrol. 522, 391–406. https://doi.org/10.1016/j.jhydrol.2014.12.054

Alfaran, S.M.M.A., 2013. Geologic and geomorphologic impacts on the water resources , Tushka area and its vicinities , South Western Desert , Egypt . Doctoral thesis, Ain Shams University.

Aly, A.M., Froehlich, K., Nada, A., Awad, M., Hamza, M., Salem, W.M., 1993. Study of environmental isotope distribution in the Aswan High Dam Lake (Egypt) for estimation of evaporation of lake water and its recharge to adjacent groundwater. Environ. Geochem. Health 15, 37–49.

Andersen, T., Carstensen, J., Hernández-García, E., Duarte, C.M., 2009. Ecological thresholds and regime shifts: approaches to identification. Trends Ecol. Evol. 24, 49–57. https://doi.org/10.1016/J.TREE.2008.07.014

Anderson, R.B., Naftz, D.L., Day-Lewis, F.D., Henderson, R.D., Rosenberry, D.O., Stolp, B.J., Jewell, P., 2014. Quantity and quality of groundwater discharge in a hypersaline lake environment. J. Hydrol. 512, 177–194. https://doi.org/10.1016/j.jhydrol.2014.02.040

Aref, E.M.M., Kadrah, A.M.., Lotfy, Z.H., 1987. Karst topography and karstification processes in the Eocene limestone plateau of El Bahariya. Z. Geomorphol. N.F 31, 45–64.

Atkinson, T.C., Smith, D.I., 1974. Rapid groundwater flow in fissures in the chalk: an example from south Hampshire.. Q. J. Eng. Geol. Hydrogeol 7, 197–205.

doi:https://doi.org/10.1144/GSL.QJEG.1974.007.02.05.

Attanayake, M.P., Waller, D.H., 1988. Use of seepage meters in a groundwater – lake interaction study in a fractured rock basin — a case study. Can. J. Civ. Eng. 15, 984–989. https://doi.org/10.1139/l88-130

Awange, J.L., Sharifi, M.A., Keller, W., Kuhn, M., 2009. GRACE Application to the Receding Lake Victoria Water Level and Australian Drought, in: International Association of Geodesy Symposia. pp. 387–396. https://doi.org/10.1007/978-3-540-85426-5_46

Bakhbakhi, M, 2006. Nubian Sandstone Aquifer System, in: Foster, S., Loucks, D.P. (Eds.), Non-Renewable Groundwater Resources: A Guidebook on Socially Sustainable Management for Water-Policy Makers. United Nations Educational, Scientific and Cultural Organization, Paris, pp. 75–81.

Bakhbakhi, Mohamed, 2006. Nubian Sandstone Aquifer System, in Non-Renewable Groundwater Resources: A Guidebook on Socially Sustainable Management for Water-Policy Makers, United Nations Educational, Scientific and Cultural Org. Paris.

Ball, J., 1927. Problems of the Libyan Desert. Geogr. J. 70, 21-38,105-128,209-224.

Banks, D., Davies, C., Davies, W., 1995. The chalk as a karstic aquifer: evidence from a tracer test at Stanford Dingley, Berkshire, UK. Q. J. Eng. Geol. Hydrogeol. 28, S31–S38. https://doi.org/10.1144/GSL.QJEGH.1995.028.S1.03

Bear, J., 1972. Dynamics of fluids in porous media. Elsevier, New York. https://doi.org/10.1016/S0006-3223(98)00224-8

Becker, N.S.C., Bennett, D.M., Bolto, B.A., Dixon, D.R., Eldridge, R.J., Le, N.P., Rye, C.S., 2004. Detection of polyelectrolytes at trace levels in water by fluorescent tagging. React. Funct. Polym. 60, 183–193. https://doi.org/10.1016/j.reactfunctpolym.2004.02.022

Begnudelli, L., Sanders, B.F., 2007. Simulation of the St. Francis Dam-Break Flood. J. Eng. Mech. 133, 1200–1212. https://doi.org/10.1061/(ASCE)0733-9399(2007)133:11(1200)

Belanger, T. V., Kirkner, R.A., 1994. Groundwater/surface water interaction in a florida augmentation lake. Lake Reserv. Manag. 8, 165–174. https://doi.org/10.1080/07438149409354468

Belanger, T. V., Montgomery, M.T., 1992. Seepage meter errors. Limnol. Oceanogr. 37, 1787–1795. https://doi.org/10.4319/lo.1992.37.8.1787

Born, S.M., Smith, S.A., Stephenson, D.A., 1979. Hydrogeology of glacial-terrain lakes, with management and planning applications. J. Hydrol. 43, 7–43. https://doi.org/10.1016/0022-1694(79)90163-X

Butzer, K.W., 1965. Desert landforms at the Kurkur Oasis. Egypt.Association Am. Geogr. 55, 578–591.

Chao, W., Qian, J., Guo, Z., Zhao, L., Li, X., 2008. Vertical Distributions of Phosphorus Fractions in Sediments of Three Typical Shallow Urban Lakes in P.R. China. Polish J. Environ. Stud. 17, 155–162.

Chen, Z., Grasby, S.E., Osadetz, K.G., 2004. Relation between climate variability and groundwater levels in the upper carbonate aquifer, southern Manitoba, Canada. J. Hydrol. 290, 43–62. https://doi.org/10.1016/J.JHYDROL.2003.11.029

Cheng, M., Ries, J.C., Tapley, B.D., 2011. Variations of the Earth's figure axis from satellite laser ranging and GRACE. J. Geophys. Res. 116, B01409. https://doi.org/10.1029/2010JB000850

Cherkauer, D.S., Zager, J.P., 1989. Groundwater interaction with a kettle-hole lake: Relation of observations to digital simulations. J. Hydrol. 109, 167–184. https://doi.org/10.1016/0022-1694(89)90013-9

Chipman, J.W., Lillesand, T.M., 2007. Satellite-based assessment of the dynamics of new lakes in southern Egypt. Int. J. Remote Sens. 28, 4365–4379. https://doi.org/10.1080/01431160701241787

Cochand, M., Molson, J., Barth, J.A.C., van Geldern, R., Lemieux, J.M., Fortier, R., Therrien,

R., 2020. Rapid groundwater recharge dynamics determined from hydrogeochemical and isotope data in a small permafrost watershed near Umiujaq (Nunavik, Canada). Hydrogeol. J. 28, 853–868. https://doi.org/10.1007/s10040-020-02109-x

Conco, C., 1987. Geological map of Egypt, Scale 1:500,000. Geological Survey and Egyptian General Petroleum Corporation, Cairo, Egypt.

Coplen, T.B., 1996. New guidelines for reporting stable hydrogen, carbon, and oxygen isotope-ratio data. Geochim. Cosmochim. Acta 60, 3359–3360. https://doi.org/10.1016/0016-7037(96)00263-3

Craig, H., 1961. Isotopic variations in meteoric waters. Science 133, 1702–1703. https://doi.org/10.1126/science.133.3465.1702

Crétaux, J.F., Abarca-del-Río, R., Bergé-Nguyen, M., Arsen, A., Drolon, V., Clos, G., Maisongrande, P., 2016. Lake Volume Monitoring from Space. Surv. Geophys. https://doi.org/10.1007/s10712-016-9362-6

Dapaah-Siakwan, S., Gyau-Boakye, P., 2000. Hydrogeologic framework and borehole yields in Ghana. Hydrogeol. J. 8, 405–416.

Dickinson, J., Ferré, T., Bakker, M., Crompton, B., 2014. A screening tool for delineating subregions of steady recharge within groundwater models. Vadose Zo. J. 13. https://doi.org/https://doi.org/10.2136/vzj2013.10.0184

Dietzel, M., Leis, A., Abdalla, R., Savarino, J., Morin, S., Böttcher, M.E., Köhler, S., 2014. 17O excess traces atmospheric nitrate in paleo-groundwater of the Saharan desert. Biogeosciences 11, 3149–3161. https://doi.org/10.5194/bg-11-3149-2014

Döll, P., Fritsche, M., Eicker, A., Müller Schmied, H., 2014. Seasonal Water Storage Variations as Impacted by Water Abstractions: Comparing the Output of a Global Hydrological Model with GRACE and GPS Observations. Surv. Geophys. 35, 1311–1331. https://doi.org/10.1007/s10712-014-9282-2

El-Hinnawi, M., Philibbos, E., Riad, S., El-Khawaga, M.M., 2006. Geological Map of the north

Western Desert, Egypt. 25 Sheets, scale 1:250,000.

El-Hinnawi, M., Philibbos, E., Riad, S., El-Khawaga, M.M., 2005. Geological Map of the south Western Desert, Egypt. 30 Sheets, scale 1:250,000.

El-Zehairy, A.A., Lubczynski, M.W., Gurwin, J., 2018. Interactions of artificial lakes with groundwater applying an integrated MODFLOW solution. Hydrogeol. J. 26, 109–132. https://doi.org/10.1007/s10040-017-1641-x

El Gammal, E., 2010. New Findings On The Karst In Nubia Sandstone Southern Egypt. Nat. Sci. 8, 125–129.

Elsaka, B., Alothman, A., Godah, W., 2016. On the contribution of GOCE satellite-based GGMs to improve GNSS/leveling geoid heights determination in Saudi Arabia. IEEE J. Sel. Top. Appl. Earth Obs. Remote Sens. 9, 5842–5850. https://doi.org/10.1109/JSTARS.2015.2495193

Eraso, A., Trzhtsinskij, Y., Castrillo, A.., 1995. Dolinas de colapso y karst en yeso en la plataforma cámbrica del esta de Siberia. Boletın Geológico y Min. 106, 373–378.

Fairhead, J.D., Salem, A., Cascone, L., Hammill, M., Masterton, S., Samson, E., 2011. New developments of the magnetic tilt-depth method to improve structural mapping of sedimentary basins. Geophys. Prospect. 59, 1072–1086. https://doi.org/10.1111/j.1365-2478.2011.01001.x

Fendorf, S., Michael, H.A., van Geen, A., 2010. Spatial and temporal variations of groundwater arsenic in South and Southeast Asia. Science 328, 1123–7. https://doi.org/10.1126/science.1172974

Fendorf, S., Michael, H.A., van Geen, A., 2010. Spatial and temporal variations of groundwater arsenic in South and Southeast Asia. Science 328, 1123–7. https://doi.org/10.1126/science.1172974

Feng, W., 2019. GRAMAT: a comprehensive Matlab toolbox for estimating global mass variations from GRACE satellite data. Earth Sci. Informatics 12, 389–404.

https://doi.org/10.1007/s12145-018-0368-0

Ford, D., 2014. Expect the Unexpected! Groundwater Flow in Karstified Carbonate Aquifers, in: H2Karst Research in Limestone Hydrogeology. Springer International Publishing, pp. 1–17. https://doi.org/10.1007/978-3-319-06139-9_1

Freitas, J.G., Furquim, S.A.C., Aravena, R., Cardoso, E.L., 2019. Interaction between lakes' surface water and groundwater in the Pantanal wetland, Brazil. Environ. Earth Sci. 78, 1–15. https://doi.org/10.1007/s12665-019-8140-4

Gat, J.R., 1995. Stable Isotopes of Fresh and Saline Lakes, in: Physics and Chemistry of Lakes. Springer Berlin Heidelberg, pp. 139–165. https://doi.org/10.1007/978-3-642-85132-2_5

Geyer, T., Birk, S., Liedl, R., Sauter, M., 2008. Quantification of temporal distribution of recharge in karst systems from spring hydrographs. J. Hydrol. 348, 452–463. https://doi.org/10.1016/J.JHYDROL.2007.10.015

Gilbert, R., 1978. Observations on Oceanography and Sedimentation at Pangnirtung Fiord, Baffin Island.

Gleick, P.H., 2000. A look at twenty-first century water resources development. Water Int. 25, 127–138. https://doi.org/10.1080/02508060008686804

Gonfiantini, R., 1986. Environmental isotopes in lake studies . Handb. Environ. Isot. geochemistry 2, 113–168.

Goode, D.J., 1996. Direct simulation of groundwater age. Water Resour. Res. 32, 289–296.

GRAS, 1988. Geological Research Authority of the Sudan, Khartoum. Geological Map of the Sudan, scale 1: 1,000,000, Sheets 1 and 2. Robertson Research.

Gudmundsson, A., 2000. Active fault zones and groundwater flow. Geophys. Res. Lett 27, 2993–2996. doi:https://doi.org/10.1029/1999GL011266.

Gutiérrez, F., Desir, G., Gutiérrez, M., 2003. Causes of the catastrophic failure of an earth dam built on gypsiferous alluvium and dispersive clays (Altorricón, Huesca Province, NE

Spain). Environ. Geol. 43, 842–851. https://doi.org/10.1007/s00254-002-0700-2

Halliday, W.R., 2003. Caves and karsts of northeast Africa. Int. J. Speleol. 32, 19–32. https://doi.org/http://dx.doi.org/10.5038/1827-806X.32.1.2

Hanson, R.T., Dettinger, M.D., Newhouse, M.W., 2006. Relations between climatic variability and hydrologic time series from four alluvial basins across the southwestern United States. Hydrogeol. J. 14, 1122–1146. https://doi.org/10.1007/s10040-006-0067-7

Healy, R.W., Cook, P.G., 2002. Using groundwater levels to estimate recharge. Hydrogeol. J. 10, 91–109. https://doi.org/10.1007/s10040-001-0178-0

Hermina, M., 1990. The surroundings of Kharga, Dakhla and Farafra oases. The Geology of Egypt. Balkema, Rotterdam.

Hesse, K.H., Hissese, A., Kheir, O., Schnacker, E., Schneider, M., Thorweihe, U., 1987. Hydrogeological investigations in the Nubian Aquifer system, Eastern Sahara, in: Kilitzsch, E., Schranck, E. (Eds.), Research in Egypt and Sudan. Dietrich Reimer, Berlin, pp. 397–464.

Huffman, G.J., Bolvin, D.T., Nelkin, E.J., Wolff, D.B., Adler, R.F., Gu, G., Hong, Y., Bowman, K.P., Stocker, E.F., 2007. The TRMM multisatellite precipitation analysis (TMPA): Quasi-global, multiyear, combined-sensor precipitation estimates at fine scales. J. Hydrometeorol. 8, 38–55. https://doi.org/10.1175/JHM560.1

Humphrey, V., Gudmundsson, L., Seneviratne, S.I., 2016. Assessing Global Water Storage Variability from GRACE: Trends, Seasonal Cycle, Subseasonal Anomalies and Extremes. Surv. Geophys. https://doi.org/10.1007/s10712-016-9367-1

Hussein, H.M., Abou Elenean, K.M., Marzouk, I.A., Korrat, I.M., Abu El-Nader, I.F., Ghazala, H., ElGabry, M.N., 2013. Present-day tectonic stress regime in Egypt and surrounding area based on inversion of earthquake focal mechanisms. J. African Earth Sci 81, 1–15. doi:https://doi.org/10.1016/j.jafrearsci.2012.12.002.

Jasechko, S., Perrone, D., Befus, K.M., Bayani Cardenas, M., Ferguson, G., Gleeson, T.,

Luijendijk, E., McDonnell, J.J., Taylor, R.G., Wada, Y., Kirchner, J.W., 2017. Global aquifers dominated by fossil groundwaters but wells vulnerable to modern contamination. Nat. Geosci. 10, 425–429. https://doi.org/10.1038/ngeo2943

Joseph, A., Frangi, J.P., Aranyossy, J.F., 1992. Isotope characteristics of meteoric water and groundwater in the Sahelo-Sudanese zone. J. Geophys. Res. 97, 7543. https://doi.org/10.1029/92JD00288

Kalbus, E., Reinstorf, F., Schirmer, M., 2006. Measuring methods for groundwater ? surface water interactions: a review Measuring methods for groundwater ? surface water interactions: a review. Hydrology and Earth System Hydrology and Earth System Sciences Measuring methods for groundwater-surface water interactions: a review, European Geosciences Union.

Kang, S., Hong, S.Y., 2016. Assessing Seasonal and Inter-Annual Variations of Lake Surface Areas in Mongolia during 2000-2011 Using Minimum Composite MODIS NDVI. PLoS One 11, e0151395. https://doi.org/10.1371/journal.pone.0151395

Karay, G., Hajnal, G., 2015. Modelling of Groundwater Flow in Fractured Rocks. Procedia Environ. Sci. 25, 142–149. https://doi.org/10.1016/j.proenv.2015.04.020

Kebeasy, R.M., Maamoun, M., Ibrahim, E., Megahed, A., Simpson, D.W., Leith, W.S., 1987. Earthquake studies at aswan reservoir. J. Geodyn 7, 173–193. doi:https://doi.org/10.1016/0264-3707(87)90003-2.

Kerr, Y.H., Waldteufel, P., Wigneron, J.-P., Martinuzzi, J., Font, J., Berger, M., 2001. Soil moisture retrieval from space: the Soil Moisture and Ocean Salinity (SMOS) mission. IEEE Trans. Geosci. Remote Sens. 39, 1729–1735. https://doi.org/10.1109/36.942551

Khan, S.D., Fathy, M.S., Abdelazeem, M., 2014. Remote sensing and geophysical investigations of Moghra Lake in the Qattara Depression, Western Desert, Egypt. Geomorphology 207, 10–22. https://doi.org/10.1016/J.GEOMORPH.2013.10.023

Kim, J., Sultan, M., 2002. Assessment of the long-term hydrologic impacts of Lake Nasser and

related irrigation projects in Southwestern Egypt. J. Hydrol. 262, 68–83.

Kohl, T., Evans, K.F., Hopkirk, R.J., Jung, R., Rybach, L., 1997. Observation and simulation of non-Darcian flow transients in fractured rock. Water Resour. Res. 33, 407–418. https://doi.org/10.1029/96WR03495

Krabbenhoft, D.P., Anderson, M.P., Bowser, C.J., 1990. Estimating groundwater exchange with lakes: 2. Calibration of a three-dimensional, solute transport model to a stable isotope plume. Water Resour. Res. 26, 2455–2462. https://doi.org/10.1029/WR026i010p02455

Kumar, Jonnakuti, P., Pavan Kumar, J., Ramana, D. V, Chadha, R.K., Singh, C., Shekar, M., 2012. The relation between seismicity and water level changes in the Koyna-Warna region, India Porepressure studies of Koyna Warna Region,India. View project Detecting and Correcting the Degradations of Sensors on Argo Floats Using Artificial Neural Networks View project The relation between seismicity and water level changes in the Koyna- Warna region, India. Hazards Earth Syst Sci 12, 813–817. doi:https://doi.org/10.5194/nhess-12-813-2012. Kummerow, C., Barnes, W., Kozu, T., Shiue, J., Simpson, J., 1998. The tropical rainfall Measuring mission

Kummerow, C., Barnes, W., Kozu, T., Shiue, J., Simpson, J., 1998. The Tropical Rainfall Measuring Mission (TRMM) sensor package. J. Atmos. Ocean. Technol. 15, 809–817. https://doi.org/10.1016/0273-1177(94)90210-0

Landerer, F.W., Swenson, S.C., 2012. Accuracy of scaled GRACE terrestrial water storage estimates. Water Resour. Res. 48. https://doi.org/10.1029/2011WR011453

Lapcevic, P.A., Novakowski, K.S., Sudicky, E.A., 1999. The interpretation of a tracer experiment conducted in a single fracture under conditions of natural groundwater flow. Water Resour. Res. 35, 2301–2312. https://doi.org/10.1029/1999WR900143

Lee, J., Robinson, C., Couture, R.M., 2014. Effect of groundwater-lake interactions on arsenic enrichment in freshwater beach aquifers. Environ. Sci. Technol 48, 10174–10181. doi:https://doi.org/10.1021/es5020136.

Lee, D.R., Hynes, H.B.N., 1978. Identification of Groundwater Discharge Zones in a Reach of Hillman Creek in Southern Ontario. Water Qual. Res. J. 13, 121–134. https://doi.org/10.2166/wqrj.1978.010

Lehner, B., Reidy Liermann, C., Revenga, C., Vorosmarty, C., Fekete, B., Crouzet, P., Doll, P., Endejan, M., Frenken, K., Magome, J., Nilsson, C., Robertson, J.C., Rodel, R., Sindorf, N., Wisser, D., 2011. Global Reservoir and Dam Database, Version 1 (GRanDv1): Dams, Revision 01.

Li, B., Rodell, M., Kumar, S., Beaudoing, H.K., Getirana, A., Zaitchik, B.F., de Goncalves, L.G., Cossetin, C., Bhanja, S., Mukherjee, A., Tian, S., Tangdamrongsub, N., Long, D., Nanteza, J., Lee, J., Policelli, F., Goni, I.B., Daira, D., Bila, M., de Lannoy, G., Mocko, D., Steele-Dunne, S.C., Save, H., Bettadpur, S., 2019. Global GRACE Data Assimilation for Groundwater and Drought Monitoring: Advances and Challenges. Water Resour. Res. 55, 7564–7586. https://doi.org/10.1029/2018WR024618

Longuevergne, L., Wilson, C.R., Scanlon, B.R., Crétaux, J.F., 2013. GRACE water storage estimates for the Middle East and other regions with significant reservoir and lake storage. Hydrol. Earth Syst. Sci. 17, 4817–4830. https://doi.org/10.5194/hess-17-4817-2013

Long, D., Longuevergne, L., Scanlon, B.R., 2015. Global analysis of approaches for deriving total water storage changes from GRACE satellites. Water Resour. Res. 51, 2574–2594. https://doi.org/10.1002/2014WR016853

Luthcke, S.B., Sabaka, T.J., Loomis, B.D., Arendt, A.A., McCarthy, J.J., Camp, J., 2013. Antarctica, Greenland and Gulf of Alaska land-ice evolution from an iterated GRACE global mascon solution. J. Glaciol. 59, 613–631. https://doi.org/10.3189/2013JoG12J147

Martens, B., Miralles, D.G., Lievens, H., van der Schalie, R., de Jeu, R.A.M., Fernández-Prieto, D., Beck, H.E., Dorigo, W.A., Verhoest, N.E.C., 2017. GLEAM v3: satellite-based land evaporation and root-zone soil moisture. Geosci. Model Dev. 10, 1903–1925. https://doi.org/10.5194/gmd-10-1903-2017

Milanović, P., 2014. Hydraulic Properties of Karst Groundwater and Its Impacts on Large

Structures, in: H2Karst Research in Limestone Hydrogeology. Springer International Publishing, pp. 19–48. https://doi.org/10.1007/978-3-319-06139-9_2

Milewski, A., Sultan, M., Yan, E., Becker, R., Abdeldayem, A., Soliman, F., Gelil, K.A., 2009. A remote sensing solution for estimating runoff and recharge in arid environments. J. Hydrol. 373, 1–14. https://doi.org/10.1016/j.jhydrol.2009.04.002

Miller, H.G., Singh, V., 1994. Potential field tilt—a new concept for location of potential field sources. J. Appl. Geophys. 32, 213–217. https://doi.org/10.1016/0926-9851(94)90022-1

Mohamed, A., Sultan, M., Ahmed, M., Yan, E., Ahmed, E., 2017. Aquifer recharge, depletion, and connectivity: Inferences from GRACE, land surface models, and geochemical and geophysical data. Bull. Geol. Soc. Am. https://doi.org/10.1130/B31460.1

Mohamed, A., Sultan, M., Ahmed, M., Yan, E., Ahmed, E., 2016. Aquifer recharge, depletion, and connectivity: Inferences from GRACE, land surface models, and geochemical and geophysical data. Geol. Soc. Am. Bull. B31460.1. https://doi.org/10.1130/B31460.1

Moore, P., Williams, S.D.P., 2014. Integration of altimetric lake levels and GRACE gravimetry over Africa: Inferences for terrestrial water storage change 2003-2011. Water Resour. Res. 50, 9696–9720. https://doi.org/10.1002/2014WR015506

Mostafa, A., 2013. Paleokarst shafts in the western desert of Egypt: A unique landscape. Acta Carsologica 42. https://doi.org/10.3986/ac.v42i1.631

Murdoch, L.C., Kelly, S.E., 2003. Factors affecting the performance of conventional seepage meters. Water Resour. Res. 39.

Nanteza, J., de Linage, C.R., Thomas, B.F., Famiglietti, J.S., 2016. Monitoring groundwater storage changes in complex basement aquifers: An evaluation of the GRACE satellites over East Africa. Water Resour. Res. 52, 9542–9564. https://doi.org/10.1002/2016WR018846

Neev, D., 1975. Tectonic evolution of the Middle East and the Levantine basin (easternmost Mediterranean). Geology 3, 683. https://doi.org/10.1130/0091-7613(1975)3<683:TEOTME>2.0.CO;2

Neev, D., Hall, J.K., Saul, J.M., 1982. The Pelusium Megashear System across Africa and associated lineament swarms. J. Geophys. Res. Solid Earth 87, 1015–1030. https://doi.org/10.1029/JB087iB02p01015

Othman, A., Sultan, M., Becker, R., Alsefry, S., Alharbi, T., Gebremichael, E., Alharbi, H., Abdelmohsen, K., 2018. Use of Geophysical and Remote Sensing Data for Assessment of Aquifer Depletion and Related Land Deformation. Surv. Geophys 39, 543–566. doi:https://doi.org/10.1007/s10712-017-9458-7.

Oruc, B., 2010. Edge detection and depth estimation using a tilt angle map from gravity gradient data of the Kozaklı-Central Anatolia region, Turkey. Pure Appl. Geophys. 168, 1769–1780. https://doi.org/10.1007/s00024-010-0211-0

Patterson, L.J., Sturchio, N.C., Kennedy, B.M., Van Soest, M.C., Sultan, M., Lu, Z.T., Lehmann, B., Purtschert, R., Alfy, Z. El, Kaliouby, B. El, Dawood, Y., Abdallah, A., 2005. Cosmogenic, radiogenic, and stable isotopic constraints on groundwater residence time in the Nubian Aquifer, Western Desert of Egypt. Geochemistry, Geophys. Geosystems 6. https://doi.org/10.1029/2004GC000779

Petronici, Pujades, Jurado, Marcaccio, Borgatti, 2019. Numerical Modelling of the Mulino Delle Vene Aquifer (Northern Italy) as a Tool for Predicting the Hydrogeological System Behavior under Different Recharge Conditions. Water 11, 2505. https://doi.org/10.3390/w11122505

Prell, W.L., Kutzbach, J.E., 1987. Monsoon variability over the past 150,000 years. J. Geophys. Res. 92, 8411–8425. https://doi.org/10.1029/JD092iD07p08411

Qian, J., Zhan, H., Zhao, W., Sun, F., 2005. Experimental study of turbulent unconfined groundwater flow in a single fracture. J. Hydrol. 311, 134–142. https://doi.org/10.1016/J.JHYDROL.2005.01.013

Ramillien, G., Biancale, R., Gratton, S., Vasseur, X., Bourgogne, S., 2011. GRACE-derived surface water mass anomalies by energy integral approach: Application to continental hydrology. J. Geod. 85, 313–328. https://doi.org/10.1007/s00190-010-0438-7

Reeves, J., Chen, J., Wang, X.L., Lund, R., Lu, Q.Q., Reeves, J., Chen, J., Wang, X.L., Lund, R., Lu, Q.Q., 2007. A Review and Comparison of Changepoint Detection Techniques for Climate Data. J. Appl. Meteorol. Climatol. 46, 900–915. https://doi.org/10.1175/JAM2493.1

Rodell et al., 2020. Monthly gridded Global Land Data Assimilation System (GLDAS) from Noah-v3.3 land hydrology model for GRACE and GRACE-FO over nominal months. PO.DAAC, CA, USA. https://doi.org/https://doi.org/10.5067/GGDAS-3NH33

Rodionov, S.N., 2004. A sequential algorithm for testing climate regime shifts. Geophys. Res. Lett. 31, n/a-n/a. https://doi.org/10.1029/2004GL019448

Rosenberry, D.O., Duque, C., Lee, D.R., 2020. History and evolution of seepage meters for quantifying flow between groundwater and surface water: Part 1 – Freshwater settings. Earth-Science Rev. https://doi.org/10.1016/j.earscirev.2020.103167

Rosenberry, D.O., Sheibley, R.W., Cox, S.E., Simonds, F.W., Naftz, D.L., 2013. Temporal variability of exchange between groundwater and surface water based on high-frequency direct measurements of seepage at the sediment-water interface. Water Resour. Res. 49, 2975–2986. https://doi.org/10.1002/WRCR.20198@10.1002/(ISSN)1944-7973.AQUIDER1

Ruggieri, R., 2001. Speleologia d'Egitto. Speleologia, Soc. Spel. Ital. Bol. 45 42- 51.

Russo, T.A., Lall, U., 2017. Depletion and response of deep groundwater to climate-induced pumping variability. Nat. Geosci. 10, 105–108. https://doi.org/10.1038/ngeo2883

Said, R., 1993. The River Nile:Geology, Hydrology and Utilization. Pergamon Press.

Sanford, K.S., 1935. Sources of water in the North-Western Sudan. Geogr. J. 85, 412–431.

Sarnthein, M., Tetzlaff, G., Koopman, B., Wolter, K., Pflaumann, U., 1981. Glacial and interglacial wind regimes over the eastern subtropical Atlantic and North-West Africa. Nature 293, 193–196.

Save, H., 2019. “CSR GRACE RL06 Mascon Solutions”, https://doi.org/10.18738/T8/UN91VR, Texas Data Repository Dataverse, V1 [WWW Document]. URL https://dataverse.tdl.org/dataset.xhtml?persistentId=doi:10.18738/T8/UN91VR (accessed 12.24.19).

Save, H., Bettadpur, S., Tapley, B.D., 2016. High-resolution CSR GRACE RL05 mascons. J. Geophys. Res. Solid Earth 121, 7547–7569. https://doi.org/10.1002/2016JB013007

Save, H., Bettadpur, S., Tapley, B.D., 2012. Reducing errors in the GRACE gravity solutions using regularization. J. Geod. 86, 695–711. https://doi.org/10.1007/s00190-012-0548-5

Scanlon, B.R., Faunt, C.C., Longuevergne, L., Reedy, R.C., Alley, W.M., McGuire, V.L., McMahon, P.B., 2012. Groundwater depletion and sustainability of irrigation in the US High Plains and Central Valley. Proc. Natl. Acad. Sci. U. S. A. 109, 9320–9325. https://doi.org/10.1073/pnas.1200311109

Scanlon, B.R., Zhang, Z., Rateb, A., Sun, A., Wiese, D., Save, H., Beaudoing, H., Lo, M.H., Müller-Schmied, H., Döll, P., Beek, R., Swenson, S., Lawrence, D., Croteau, M., Reedy, R.C., 2019. Tracking Seasonal Fluctuations in Land Water Storage Using Global Models and GRACE Satellites. Geophys. Res. Lett. 46, 5254–5264. https://doi.org/10.1029/2018GL081836

Scanlon, Bridget R, Zhang, Z., Save, H., Wiese, D.N., Landerer, F.W., Long, D., Longuevergne, L., Chen, J., 2016. Global evaluation of new GRACE mascon products for hydrologic applications. Water Resour. Res. 52, 9412–9429. https://doi.org/10.1002/2016WR019494

Scanlon, Bridget R., Zhang, Z., Save, H., Wiese, D.N., Landerer, F.W., Long, D., Longuevergne, L., Chen, J., 2016. Global evaluation of new GRACE mascon products for hydrologic applications. Water Resour. Res. 52, 9412–9429. https://doi.org/10.1002/2016WR019494

Schneider, R.L., Negley, T.L., Wafer, C., 2005. Factors influencing groundwater seepage in a large, mesotrophic lake in New York. J. Hydrol. 310, 1–16. https://doi.org/10.1016/j.jhydrol.2004.09.020

Seaton, W.J., Burbey, T.J., 2005. Influence of ancient thrust faults on the hydrogeology of the blue ridge province. Ground Water 43, 301–313. https://doi.org/10.1111/j.1745-6584.2005.0026.x

Shaw, G.D., White, E.S., Gammons, C.H., 2013. Characterizing groundwater-lake interactions and its impact on lake water quality. J. Hydrol. 492, 69–78. https://doi.org/10.1016/j.jhydrol.2013.04.018

Sissakian, V.K., Adamo, N., Al-Ansari, N., Knutsson, S., Laue, J., Elagely, M., 2018. A Comparative Study of Mosul and Haditha Dams, Iraq: Geological Conditions. J. Earth Sci. Geotech. Eng. 8, 35–52.

Smerdon, B.D., Mendoza, C.A., Devito, K.J., 2007. Simulations of fully coupled lake-groundwater exchange in a subhumid climate with an integrated hydrologic model. Water Resour. Res. 43. https://doi.org/10.1029/2006WR005137

Stonestrom, D.A., Constantz, ed., 2003. Heat as a tool for studying the movement of ground water near streams. USGS Circular 1260. USGS.

Sturchio, N.C., Du, X., Purtschert, R., Lehmann, B.E., Sultan, M., Patterson, L.J., Lu, Z.-T., Müller, P., Bigler, T., Bailey, K., O'Connor, T.P., Young, L., Lorenzo, R., Becker, R., El Alfy, Z., El Kaliouby, B., Dawood, Y., Abdallah, A.M.A., 2004. One million year old groundwater in the Sahara revealed by krypton-81 and chlorine-36. Geophys. Res. Lett. 31, 2–5. https://doi.org/10.1029/2003GL019234

Sultan, M., Ahmed, M., Sturchio, N., Yan, Y.E., Milewski, A., Becker, R., Wahr, J., Becker, D., Chouinard, K., 2013. Assessment of the vulnerabilities of the Nubian Sandstone Fossil Aquifer, North Africa, in: Pielke, R.A. (Ed.), in: Climate Vulnerability. Elsevier, Cambridge, Massachusetts, pp. 311–333. https://doi.org/10.1016/B978-0-12-384703-4.00531-1

Sultan, M., Ahmed, M., Wahr, J., Yan, E., Emil, M.K., 2014. Monitoring aquifer depletion from space, in: Lakshmi, V., Alsdorf, D., Anderson, M., Biancamaria, S., Cosh, M., Entin, J., Huffman, G., Kustas, W., Oevelen, P. V, Painter, T., Parajka, J., Rodell, M., Rüdiger, C.

(Eds.), Remote Sensing of the Terrestrial Water Cycle. John Wiley {&} Sons, Inc, Hoboken, NJ, pp. 347–366. https://doi.org/10.1002/9781118872086.ch21

Sultan, M., Sturchio, N., Hassan, F.A., Hamdan, M.A.R., Mahmood, A.M., ElAlfy, Z., Stein, T., 1997. Precipitation source inferred from stable isotopic composition of Pleistocene groundwater and carbonate deposits in the Western Desert of Egypt. Quat. Res. 48, 29–37. https://doi.org/https://doi.org/10.1006/qres.1997.1907

Sultan, M., Sturchio, N.C., Alsefry, S., Emil, M.K., Ahmed, M., Abdelmohsen, K., AbuAbdullah, M.M., Yan, E., Save, H., Alharbi, T., Othman, A., Chouinard, K., 2019. Assessment of age, origin, and sustainability of fossil aquifers: A geochemical and remote sensing–based approach. J. Hydrol. https://doi.org/10.1016/J.JHYDROL.2019.06.017

Sultan, M., Wagdy, A., Manocho, N., Sauck, W., Abdel Gelil, K., Youssef, A.F., Becker, R., Milewski, A., El Alfy, Z., Jones, C., 2007a. An integrated approach for identifying aquifers in transcurrent fault systems: The Najd shear system of the Arabian Nubian shield. J. Hydrol. 349, 475–488. https://doi.org/10.1016/j.jhydrol.2007.11.029

Sultan, M., Yan, E., Sturchio, N., Wagdy, A., Milewski, A., Abdel Gelil, K., Manocha, N., Becker, R., 2007b. Natural discharge: A key to sustainable utilization of fossil groundwater. J. Hydrol. 335, 25–36. https://doi.org/10.1016/j.jhydrol.2006.10.034

Swenson, S., Famiglietti, J., Basara, J., Wahr, J., 2008. Estimating profile soil moisture and groundwater variations using GRACE and Oklahoma Mesonet soil moisture data. Water Resour. Res. 44. https://doi.org/10.1029/2007WR006057

Swenson, S., Wahr, J., 2007. Multi-sensor analysis of water storage variations of the Caspian Sea. Geophys. Res. Lett. 34. https://doi.org/10.1029/2007GL030733

Swenson, S., Wahr, J., 2002. Methods for Inferring Regional Surface-Mass Anomalies from Gravity Recovery and Climate Experiment (GRACE) Measurements of Time-Variable Gravity. J. Geophys. Res. 107.

Tapley, B D, Bettadpur, S., Ries, J.C., Thompson, P.F., Watkins, M.M., 2004a. GRACE

measurements of mass variability in the Earth system. Science (80-.). 305, 503–505. https://doi.org/DOI: 10.1126/science.1099192

Tapley, B D, Bettadpur, S., Watkins, M., Reigber, C., 2004b. The Gravity Recovery and Climate Experiment: Mission overview and early results. Geophys. Res. Lett. 31, L09607. https://doi.org/10.1029/2004GL019920

Thomas, B.F., Famiglietti, J.S., 2019. Identifying Climate-Induced Groundwater Depletion in GRACE Observations. Sci. Rep. 9. https://doi.org/10.1038/s41598-019-40155-y

Thorweihe, U., Heinl, M., 2002. Groundwater Resources of the Nubian Aquifer System NE Africa. Tech. Univ. of Berlin, Berlin 1–23.

Thorweihe, U., 1990. Nubian Aquifer System. Geology of Egypt. R. Said, Ed., Balkema, Rotterdam.

Thorweihe, U., 1986. Isotopic identification and mass balance of the Nubian Aquifer System in Egypt, in Thorweihe, U., ed., Impact of climatic variations on East Saharian groundwaters—modelling of large scale flow regimes, Proceedings of a Workshop on Hydrology: Berlin, Berliner Geowissenschaftliche Abhandlungen, ser. A 72, 87–97.

Thurmond, A.K., Stern, R.J., Abdelsalam, M.G., Nielsen, K.C., Abdeen, M.M., Hinz, E., 2004. The Nubian Swell. https://doi.org/10.1016/j.jafrearsci.2004.07.027

Tiwari, V.M., Wahr, J., Swenson, S., 2009. Dwindling groundwater resources in northern India, from satellite gravity observations. Geophys. Res. Lett 36. https://doi.org/10.1029/2009GL039401

Tóth, J., 1963. A theoretical analysis of groundwater flow in small drainage basins. J. Geophys. Res. 68, 4795–4812. https://doi.org/10.1029/jz068i016p04795

UNECA, 2011. Economic Report on Africa 2011 | United Nations Economic Commission for Africa.

Velicogna, I., Wahr, J., 2006. Measurements of time-variable gravity show mass loss in

Antarctica. Science (80-.). 311, 1754–1756.

Verduzco, B., Fairhead, J.D., Green, C.M., Mackenzie, C., 2004. New ınsights into magnetic derivatives for structural mapping, Lead. Lead. Edge 23, 116–119.

Villarini, G., Serinaldi, F., Smith, J.A., Krajewski, W.F., 2009. On the stationarity of annual flood peaks in the continental United States during the 20th century. Water Resour. Res. 45. https://doi.org/10.1029/2008WR007645

Virdi, M.L., Lee, T.M., Swancar, A., Niswonger, R.G., 2012. Simulating the Effect of Climate Extremes on Groundwater Flow Through a Lakebed. Ground Water 51, no-no. https://doi.org/10.1111/j.1745-6584.2012.00969.x

Voss, K.A., Famiglietti, J.S., Lo, M., de Linage, C., Rodell, M., Swenson, S.C., 2013. Groundwater depletion in the Middle East from GRACE with implications for transboundary water management in the Tigris-Euphrates-Western Iran region. Water Resour. Res. 49, 904–914. https://doi.org/10.1002/wrcr.20078

Wahr, J., Molenaar, M., Bryan, F., 1998. Time variability of the Earth's gravity field: Hydrological and oceanic effects and their possible detection using GRACE. J. Geophys. Res. 103, 30205–30229.

Wahr, J., Swenson, S., Zlotnicki, V., Velicogna, I., 2004. Time-variable gravity from GRACE: First results. Geophys. Res. Lett. 31.

Waltham, T., 2001. Pinnacles and barchans in the Egyptian desert. Geol. Today 17, 101–104. https://doi.org/10.1046/j.0266-6979.2001.00288.x

Walton, W.C., 2011. Aquifer system response time and groundwater supply management. Ground Water 49, 126–127. https://doi.org/10.1111/j.1745-6584.2010.00770.x

Watkins, M.M., Wiese, D.N., Yuan, D.N., Boening, C., Landerer, F.W., 2015. Improved methods for observing Earth's time variable mass distribution with GRACE using spherical cap mascons. J. Geophys. Res. B Solid Earth 120, 2648–2671. https://doi.org/10.1002/2014JB011547

Wiese, D., Landerer, F.W., Watkins, M.M., 2016. Quantifying and reducing leakage errors in the JPL RL05M GRACE mascon solution. Water Resour. Res. 52, 7490–7502. https://doi.org/10.1002/2016WR019344

Wiese, D.N., Killett, B., Watkins, M.M., Yuan, D.-N., 2016. Antarctic tides from GRACE satellite accelerations. J. Geophys. Res. Ocean. 121, 2874–2886. https://doi.org/10.1002/2015JC011488

Winter, T.C., 1999. Relation of streams, lakes, and wetlands to groundwater flow systems. Hydrogeol. J. 7, 28–45. https://doi.org/10.1007/s100400050178

Wouters, B., Bonin, J.A., Chambers, D.P., Riva, R.E.M., Sasgen, I., Wahr, J., 2014. GRACE, time-varying gravity, Earth system dynamics and climate change. Reports Prog. Phys. 77. https://doi.org/10 .1088 /0034 -4885 /77 /11 /116801

Yan, Z.W., Petit-Maire, N., 1994. The last 140-Ka in the Afro-Asian arid/semi-arid transitional zone. Palaeogeogr. Palaeoclimatol. Palaeoecol. 110, 217–233. https://doi.org/https://doi.org/10.1016/0031-0182(94)90085-X

Yidana, S., Ophori, D., Banoeng-Yakubo, B., 2007. Hydrogeological and hydrochemical characterization of the Voltaian Basin: the Afram Plains area, Ghana. Environ. Geol. 53, 1213–1223. https://doi.org/10.1007/s00254-007-0710-1

Yidana, S.M., Evans, ·, Vakpo, K., Patrick, ·, Sakyi, A., Larry, ·, Chegbeleh, P., Akabzaa, T.M., 2019. Groundwater-lakewater interactions: an evaluation of the impacts of climate change and increased abstractions on groundwater contribution to the Volta Lake, Ghana. Environ. Earth Sci. 78, 74. https://doi.org/10.1007/s12665-019-8076-8

APPENDICES

A. Climate Variability

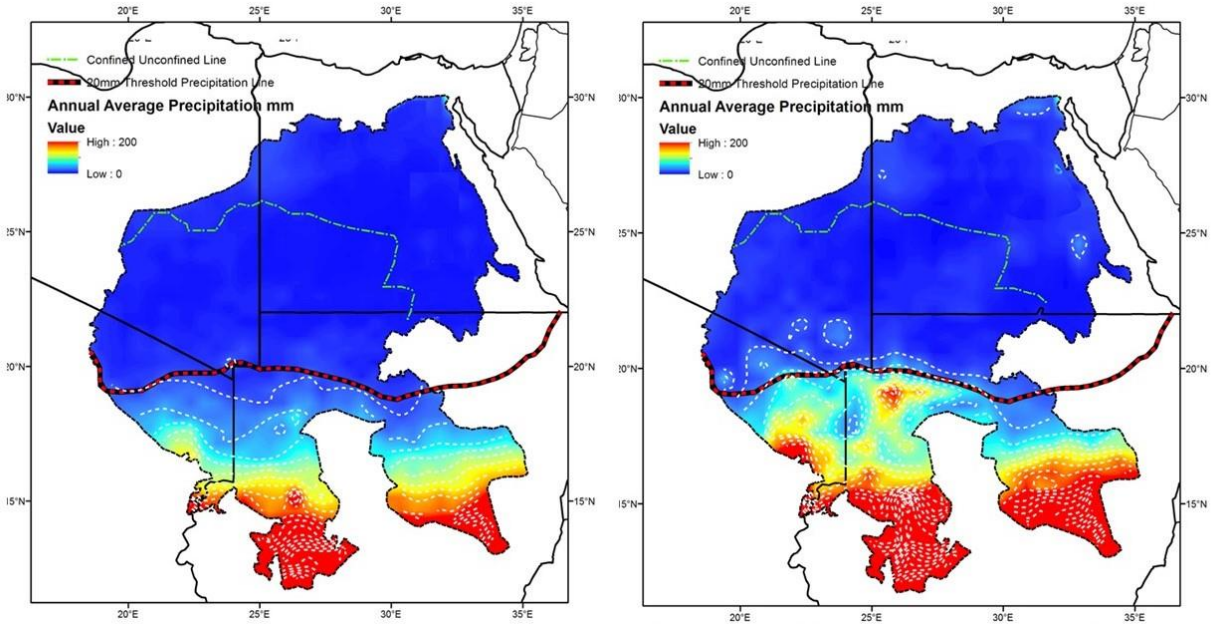

Figure. A1. Shows a significant increase in precipitation over the southern sections of the Nubian Sandstone Aquifer System (NSAS) during the wet period, but not over the northern sections (Dakhla subbasin). The increased precipitation during the wet period is affecting the NSAS in two ways: 1) increasing recharge in the southern sections of the NSAS, and 2) increasing the runoff in the Nile river and the surface water level of lake Nasser.

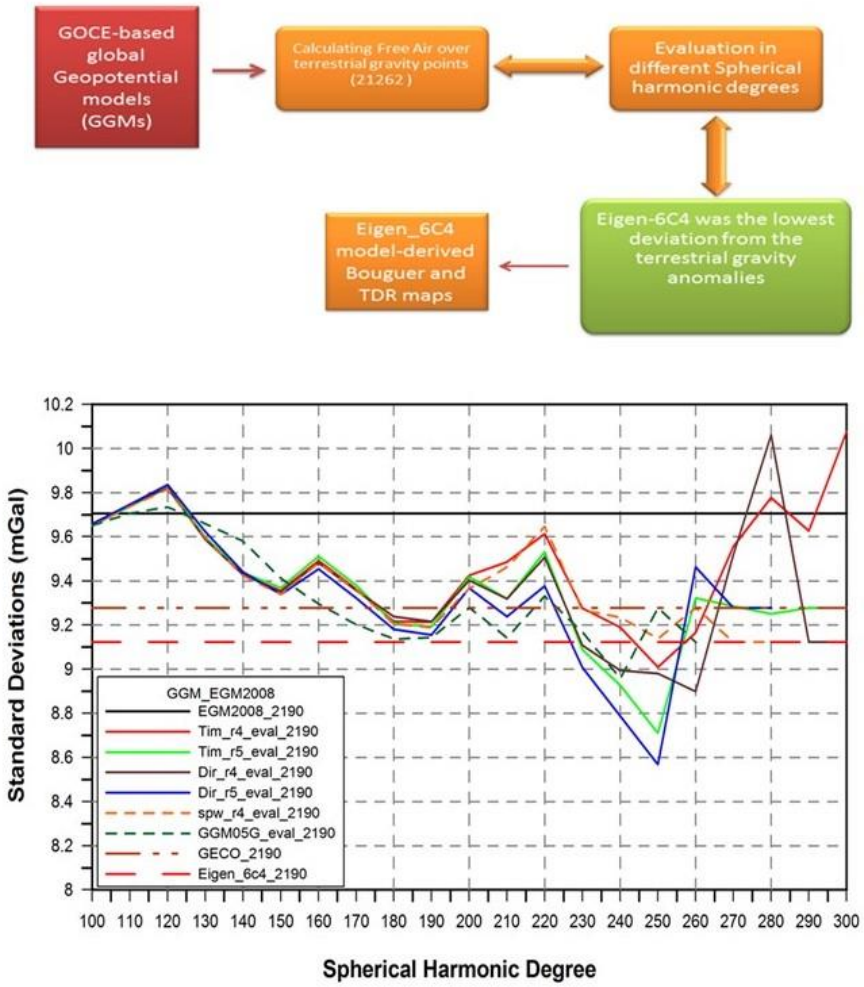

Figure. A2. Geopotential models over Egypt were compared to geophysical gravity field surveys to evaluate the performance of these models and to select the optimum geopotential model. The Egine_6c4 model showed the lowest deviation from the terrestrial data and was selected as the optimum geopotential model.

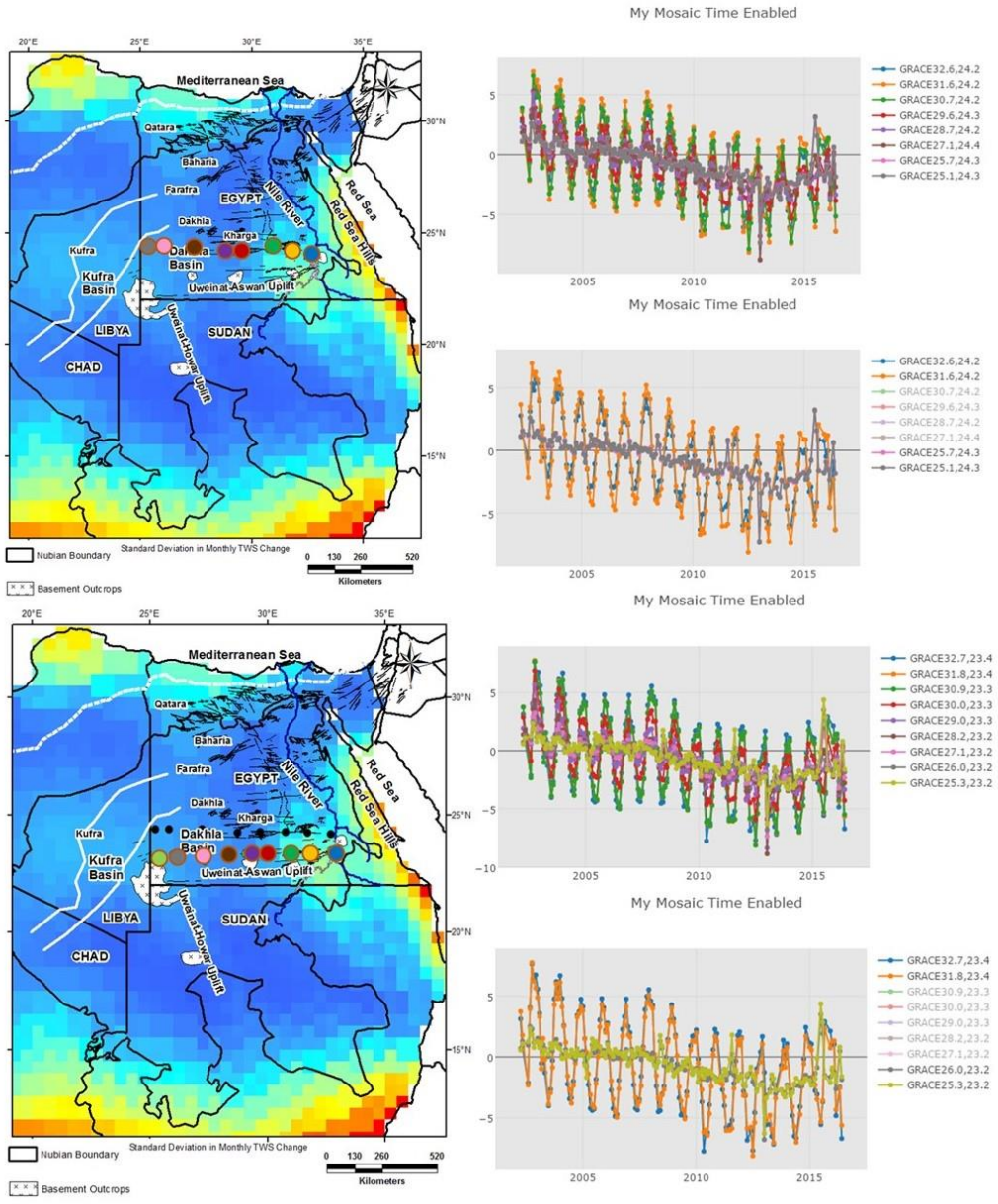

Figure. A3. Propagation of water mass from Lake Nasser to the Dakhla subbasin aong E-W trending fracture zones. The TWS time series along the E-W fractures show uniform patterns along the pathways of the faults with decreasing amplitude away from Lake Nasser; dissimilar patterns are observed across the faults.

B. Seasonal Cycle

Estimation of the leakage in signal for the Dakhla subbasin

The spatial distribution of the leakage in signal for the Dakhla subbasin was estimated using the simulated SD_{TWS} for years 2015 and 2008. The latter was extracted from GLDAS (Global Land Data Simulation System) Noah data following procedures described in (Feng, 2019). The monthly mean values were calculated at GRACE and GRACE-FO monthly time steps after subtracting climatology mean 2005 to 2009. Days unused in GRACE/ GRACE-FO months were not included in the GLDAS monthly mean computation (Landerer and Swenson, 2012; Rodell et al., 2020). The computed TWS values outside the Dakhla subbasin were retained and those within the subbasin were set to zero (Fig. A1). Spherical Harmonic (SH) analysis was conducted up to degree/order (d/o) of 120 and a 250 km Gaussian smoothing was applied. In general the leakage in was found to be minimal to negligible across the entire Dakhla subbasin. The highest values (up to 10 mm in 2015 and 13 mm in 2008) are restricted to an east-west, 200 km deep, trending zone at the northern peripheries of the Dakhla subbasin, most likely related to northerly precipitation along the Mediterranean coast, whereas the leakage in across the remaining sections of the Dakhla subbasin is negligible (< 4 mm).

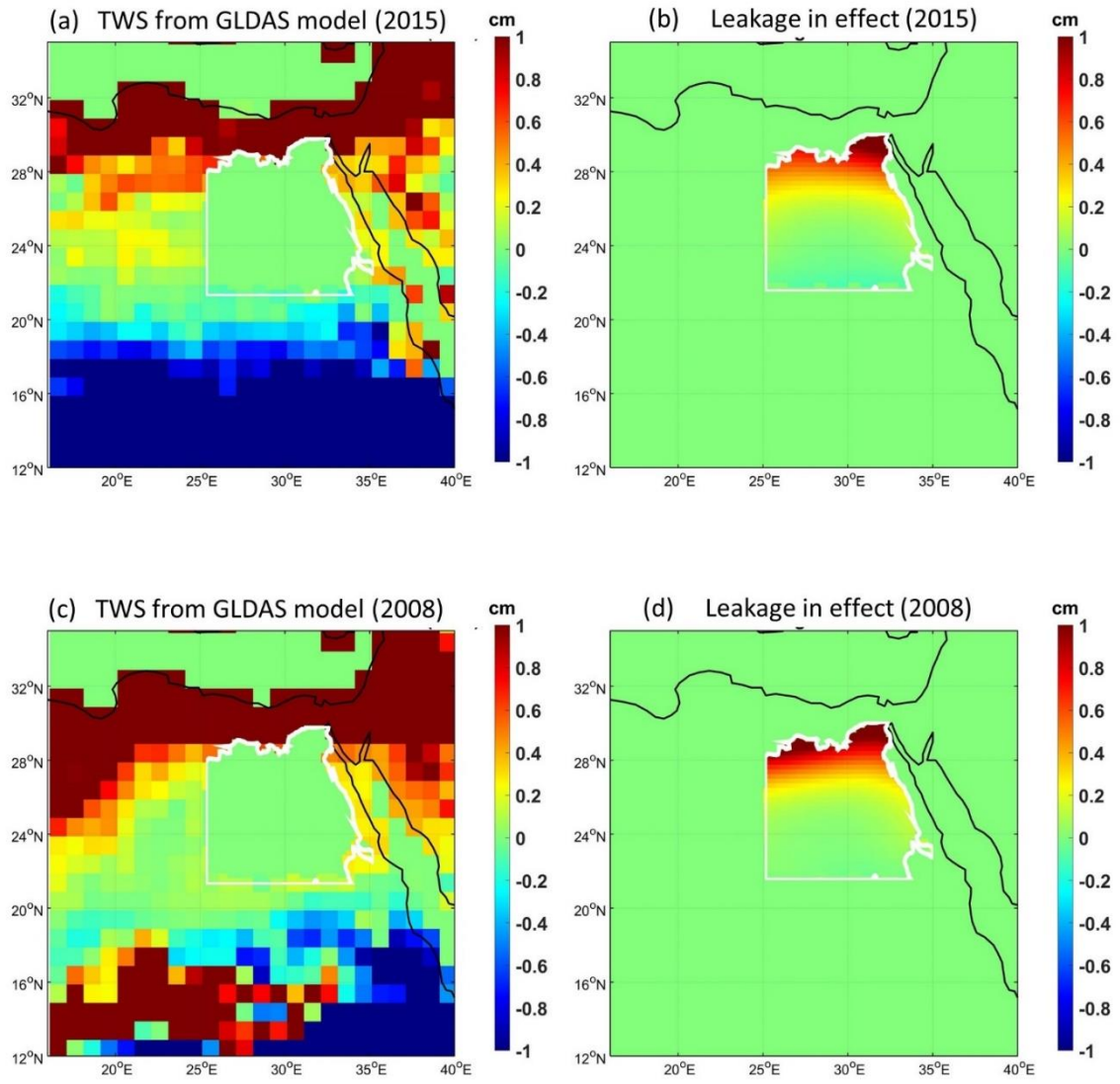

Figure. B1. Leakage in for the Dakhla subbasin. (a) a grid displaying SD_{TWS} variations extracted from the GLDAS Noah model for year 2015 over the Dakhla subbasin and its surroundings, where the extracted values were retained for grid points outside of the Dakhla subbasin and set to zero for points within it. (b) Leakage signal map for year 2015 generated by transforming the grid in the spherical harmonic domain and up to d/o 120. (c) a grid displaying SD_{TWS} variations extracted from the GLDAS Noah for year 2008 over the Dakhla subbasin. (d) Leakage signal map for year 2008 generated by transforming the grid in the spherical harmonic domain and up to d/o 120. The Dakhla subbasin extension is outlined by the white line.